Design and analysis of integrated lens antennas

van der Vorst, M.J.M.

Award date:
1997

EINDHOVEN UNIVERSITY OF TECHNOLOGY

FACULTY OF ELECTRICAL ENGINEERING

TELECOMMUNICATIONS DIVISION EC

Design and analysis of integrated lens antennas

by M.J.M. van der Vorst

Report of graduation work,
performed from April 1994 to February 1995

Supervisors : prof.dr.ir. G. Brussaard,
dr.ir. M.H.A.J. Herben and
dr.ir. P.J.I. de Maagt (ESA/ESTEC)

Those Rules of old discovered, not devised,
Are Nature still, but Nature methodized;
Nature, like liberty, is but restrained
By the same laws, which first herself ordained.

Abstract

This report gives an analysis of the radiation properties of some planar integrated circuit antennas mounted on a dielectric slab with lens. Two different planar antennas are treated: the double-slot antenna and the double-dipole antenna with a backing reflector. For the dielectric lens, which is used to focus the radiation and to reduce the substrate-mode power, two possible candidates have been analyzed and compared. Firstly, an elliptical lens that focuses an incident plane wave to one point is considered. A second elegant solution is the use of an extended hemispherical lens, which can for example be applied to synthesize the elliptical lens by a proper choice of both the radius of the hemisphere and the extension length.

For the calculation of antenna properties such as: radiation pattern, beamwidth, (Gaussian) beam efficiency and directivity, the electric and magnetic fields at the dielectric lens surface have to be known. These fields are found using ray-tracing inside the lens, assuming that the primary radiator can be treated as a point source characterized by its own far-field radiation pattern. Once the fields just outside the lens are known, an electric- and magnetic-field integration over the lens surface is applied to determine the far-field radiation pattern of the integrated lens antenna. A comparison between the results of our calculations and those obtained by Filipovic [1], for an extended hemispherical silicon lens, shows that there exists a very good correspondence. The directivities of the integrated elliptical lens antennas with a diameter of 15.0 mm are close to 30 dBi at 246 GHz, with a 10-dB beamwidth of about 8° for various antenna designs. The corresponding beam efficiencies vary from 70 to 90% depending on the planar antenna and the dielectric material used. Another very important antenna feature is the Gaussian beam efficiency or so-called Gaussicity, describing how well the radiation pattern resembles the pattern of the fundamental Gaussian beam. For the rotationally symmetric elliptical lens the Gaussicity varies between 70 and 90%. The Gaussian beam efficiency can be increased up to 97% by applying an extended hemispherical lens instead of an elliptical one.

Finally, this report describes the comparison between results of measurements and the results from our computations. The configuration used was a double-dipole antenna with a backing reflector illuminating a high density polyethylene (HDP) elliptical lens. It is shown that for the main lobe the theoretical results agree very well with the measured data. For larger angles from boresight however, there exist some differences between the two results, which can for the major part be explained by the power reflected at the lens surface.

Contents

List of symbols

a	half the length of the short axis of the ellipse
A	arbitrary constant
AF	array factor
b	half the length of the long axis of the ellipse
B	arbitrary constant
$\underline{B}$	magnetic flux density
c	focal distance
c_0	speed of light in vacuum (2.997910^8 m/s)
d	thickness of the dielectric slab
dz	length of a short slot or short dipole antenna
D	diameter of the lens
$\underline{D}$	electric flux density
$\hat{e}_{co}$	unit vector in the co-polarized direction
$\hat{e}_{cr}$	unit vector in the cross-polarized direction
$\hat{e}_\delta$	unit vector in the δ-direction
$\hat{e}_\zeta$	unit vector in the ζ-direction
$\underline{E}$	electric field
E_{co}	co-polarized electric field
E_{cr}	cross-polarized electric field
$\underline{E}_{tr}$	electric field just outside the lens
f	frequency
f_{co}	cut-off frequency
G	directive gain function or power pattern
$\underline{H}$	magnetic field
$\underline{H}_{tr}$	magnetic field just outside the lens
I	electric or magnetic current
I_e	electric current amplitude
I_m	magnetic current amplitude
j	$\sqrt{-1}$
$\underline{J}$	current density

$\underline{J}_s$	electric current density
k	wavenumber
k_m	mean wavenumber
l	half the length of the feed antenna
L_{ex}	extension length
m	integer
$\underline{M}_s$	magnetic current density
n	index of refraction
$\hat{n}$	unit normal vector
n_x	number of elements in array along the x-axis
P	radiation intensity
P_{tot}	total radiated power or input power of the feed antenna
r	distance from the center of the dielectric lens to the far-field observation point
r'	distance from the center of the dielectric lens to the equivalent electric and magnetic current densities
$\underline{r}$	vector pointing from the center of the dielectric lens to the far-field observation point
$\underline{r}'$	vector pointing from the center of the dielectric lens to the equivalent electric and magnetic current densities
R	distance from the feed antenna to the observation point
$\Re$	radius of curvature
$Re(\ )$	real part
R'	distance from a point on the feed antenna to the far-field observation point
s	distance from the double-dipole feed to its backing reflector
sgn( )	signum function
S	surface just outside the lens
t	time
w	beam radius or waist
w_0	minimum waist
x,y,z	Cartesian coordinates
Z	wave impedance
Z_0	free space impedance ($120\pi\Omega$)

α	attenuation constant
β	phase constant
γ	propagation constant
δ	angle in the xz-plane with respect to the z-axis
Δd	spacing between elements in feed-antenna array
ε_d	permittivity of the dielectric
ε_m	mean permittivity
ε_0	permittivity of vacuum ($1/36\pi\,10^{-9}$ F/m)
ε_{rd}	relative dielectric constant of the dielectric
η_a	(combined) aperture efficiency
η_p	polarization efficiency
η_s	spillover efficiency
η_{tr}	transmission efficiency
ζ	angle with the y-axis
ζ_e	width of the main beam
ζ_m	maximum angle with the y-axis of a ray illuminating the lens
θ	angle with the z-axis
θ_c	angle of incidence at the cut-off frequency (critical angle)
θ^i	angle of incidence
θ^r	angle of reflection
θ^t	angle of refraction
λ	wavelength
λ_m	mean wavelength
μ_0	permeability of vacuum ($4\pi 10^{-7}$ H/m)
ν	normalized frequency
π	3.14159265..
ρ	$\sqrt{x^2+z^2}$
$\rho_\parallel$	reflection coefficient for parallel polarization
$\rho_\perp$	reflection coefficient for perpendicular polarization
σ	conductivity
$\tau_\parallel$	transmission coefficient for parallel polarization
$\tau_\perp$	transmission coefficient for perpendicular polarization
ϕ	angle in the xy-plane with respect to the x-axis
ω	angular frequency
ω_c	angular cut-off frequency
∇	gradient $(\frac{\partial}{\partial x}, \frac{\partial}{\partial y}, \frac{\partial}{\partial z})$

1. Introduction

Due to the increasing demand for low-noise receivers operating in the millimeter-wave and submillimeter-wave region, people have looked for other system technologies than the expensive waveguide-based systems using traditional waveguide horns, i.e. Potter or corrugated horns. The applications for the low-noise receivers can be found in various areas such as remote sensing, radio astronomy, plasma diagnostics, radar and communication systems. It appears that the precision-machined waveguide-based systems are very difficult to manufacture at frequencies above 300-500 GHz. The question that arises is: How can we make reasonably priced systems for the millimeter-wave and submillimeter-wave region? It is clear that the answer is not found in just scaling down microwave systems, because the performance worsens due to the more critical alignments and metal surface tolerances.

One very attractive solution for the millimeter-wave and submillimeter-wave systems is the so-called planar integrated receiver technology. This technology is expected to lead to receivers that are easy to manufacture, reliable, small, light and much less expensive than waveguide-based receivers. One problem area used to be the unavailability of planar receiver detectors that could easily be matched with integrated antennas. Several diode types now exist which overcome this limitation and the research effort should shift towards the design of such antennas.

Integrated antennas consist of a functional combination of solid-state devices and planar printed circuit antennas. Though, it should be pointed out that this type of structure is not a simple combination of an antenna followed by active devices. One of the main immediately recognizable benefits is the elimination of the transmission line between the traditional antenna and the active circuit, because the planar antenna and the solid-state devices can be integrated into a single entity. However, the integrated antennas have traditionally suffered from poor radiation patterns and low efficiencies.

To give an idea of the possible integrated antenna structures that are used nowadays, two of these antennas are shown in Figures 1.1 and 1.2.

***Figure 1.1** : Planar log-periodic antenna on top of a dielectric lens [2].*

The first antenna that is shown in Figure 1.1 is a planar log-periodic antenna on a dielectric lens (dielectric lens antenna). A log-periodic antenna, which belongs to the class of broadside antennas, placed on a substrate lens offers an attractive solution for wideband applications. Another often used class of integrated antennas are the end-fire antennas and one example is the Vivaldi antenna, which is shown in Figure 1.2. The Vivaldi antenna is an exponentially tapered slot antenna (TSA) with the metallic slot etched on a dielectric substrate. Sometimes both sides of the dielectric are metallized.

Further, other types of integrated antennas used in millimeter-wave and submillimeter-wave systems are the dielectric-filled parabola [3] and the integrated horn antenna [4]. In this report it is chosen to analyze the integrated lens antennas, which are illuminated by a double-slot or a double-dipole (with backing reflector) feed. The lens of these antennas usually has an elliptical or an extended hemispherical shape.

An application for dielectric integrated lens antennas can be found in limb sounding [5] instruments, with which it is possible to determine the composition of the ozone layer.

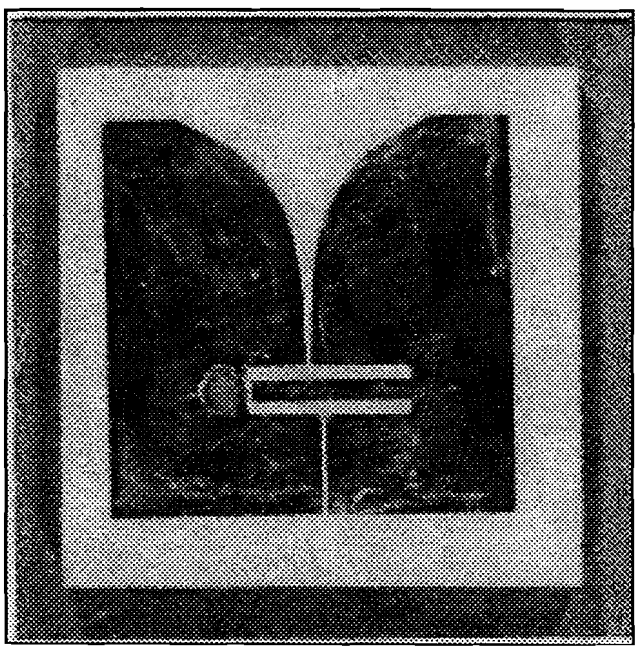

***Figure 1.2** : An exponentially tapered slot antenna (Vivaldi) [6].*

Before the complete lens antenna is considered, it is started in Chapter two with the theory of substrate modes. It is investigated to what extent this theory can be related to the Geometrical Optics (GO). Then, the radiation patterns of a slot, a double-slot and a double-dipole antenna with a backing reflector are calculated using Geometrical Optics. To eliminate the substrate modes, a dielectric lens with the same index of refraction is placed on top of the slab. In Chapter three, integrated lens antennas with an elliptical or an extended hemispherical lens are analyzed and the radiation patterns, the directivity, the beamwidth, the beam efficiency and the Gaussian beam efficiency are determined. A comparison between the results of our model and measurement results is described in Chapter four. Finally, the conclusions and recommendations are given in Chapter five.

2. Antennas on dielectric substrates

Printed antennas which are mounted on a dielectric substrate, as shown in Figure 2.1, tend to radiate most of their power into the dielectric. So, when the antenna is used in a receiving configuration, it is best to focus energy from the substrate side rather than the air side. The power radiated directly into the air can be seen as some sort of loss, but this is usual not the main loss. The main loss is formed by substrate modes, which always exist in a dielectric slab with a radiating antenna on top of it. If, from a Geometrical Optics point of view, the angle of incidence of a transmitted ray at the substrate-air interface is larger than the so-called critical angle (θ_c), this ray will be completely reflected at the interface and be trapped as substrate modes. In the next section the theory of substrate modes in a dielectric slab is treated.

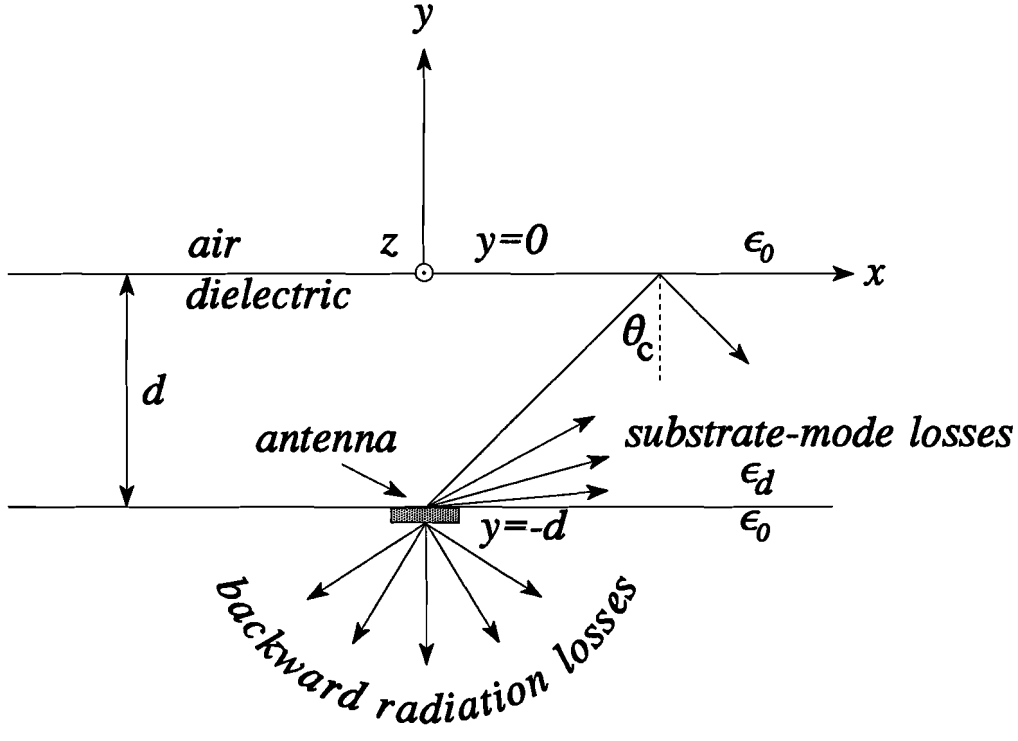

Figure 2.1 : Planar antenna printed on a dielectric slab.

2.1 Substrate modes

Integrated antennas on dielectric substrates usually suffer from relatively large substrate-mode losses. It is easy to describe the process of modes by applying Geometrical Optics, and considering a thick dielectric slab. The radiation pattern of any integrated antenna on a thick dielectric slab is usually not limited to angles smaller than the critical angle. As already stated, every ray with an angle of incidence greater than the critical angle will be totally reflected and, as a consequence, all the power radiated in the dielectric above this critical angle is converted into substrate-mode power. However, the dielectric slab is not always thick enough to validate the use of Geometrical Optics. In this case substrate-mode power can be described by using modes, and the first question that arises is: which substrate modes can exist in a dielectric slab? The dielectric slab shown in Figure 2.1 is assumed to be homogeneous, isotropic, linear and infinitely extended in the x- and z-direction. Because generally only non-magnetic materials are used, the permeability has the value μ_0. First it is started by writing down Maxwell's equations:

$$\nabla x \underline{E} = -\frac{\partial \underline{B}}{\partial t} = -\mu_0 \frac{\partial \underline{H}}{\partial t} \tag{2.1}$$

$$\nabla x \underline{H} = \frac{\partial \underline{D}}{\partial t} + \underline{J} = \varepsilon \frac{\partial \underline{E}}{\partial t} + \sigma \underline{E} \tag{2.2}$$

When it is known that the dielectric material contains no free charges, Maxwell's equations reduce to the following wave equation:

$$\nabla^2 \underline{E} = \mu_0 \varepsilon \frac{\partial^2 \underline{E}}{\partial t^2} + \mu_0 \sigma \frac{\partial \underline{E}}{\partial t} \tag{2.3}$$

In the following only attention will be paid to the transverse electric (TE) waves, because for the transverse magnetic (TM) waves the same procedure can be used. For dielectric media $\sigma \approx 0$ and therefore the last term of Equation (2.3) will further be neglected in the derivation of the substrate-mode fields.

2.1.1 Transverse electric waves

To derive solutions for Equation (2.3), harmonic waves that are independent of z are assumed. Then all the field components are proportional to $\exp(j\omega t - \gamma x)$, with $\gamma = \alpha + j\beta$, if the wave propagates in the positive x-direction.

For TE-waves polarized in the z-direction E_x and E_y are zero and therefore Equation (2.3) reduces to:

$$\frac{\partial^2 E_z}{\partial y^2} + k_c^2 E_z = 0 \tag{2.4}$$

with

$$k_c^2 = k^2 + \gamma^2 \tag{2.5}$$

and

$$k^2 = \omega^2 \mu_0 \varepsilon \tag{2.6}$$

In general, the dielectric is not free from losses (γ^2 is complex), but here only real values of γ^2 will be considered. If the dielectric losses are zero then $\gamma = j\beta$ and γ^2 is real. Solutions for the substrate modes can now be obtained if k_c^2 is made positive in the dielectric slab ($k_{cd} = h_1$) and negative in the air ($k_{ca} = jh_2$). Quantities in the dielectric slab are indicated by the subscript d and in the air by a. In Ref. [7] it is shown that the electric field components in- and outside the dielectric can be written as:

$$E_{zd} = A\cos\left[h_1\left(y + \frac{d}{2}\right)\right]\exp(j\omega t - j\beta x) \qquad -d \le y \le 0 \tag{2.7}$$

$$E_{za} = C\exp\left(-h_2\left|y + \frac{d}{2}\right|\right)\exp(j\omega t - j\beta x) \qquad y \le -d\ ,\ y \ge 0 \tag{2.8}$$

for symmetric TE-waves and

$$E_{zd} = B\sin\left[h_1\left(y + \frac{d}{2}\right)\right]\exp(j\omega t - j\beta x) \qquad -d \le y \le 0 \tag{2.9}$$

$$E_{za} = sgn\left(y + \frac{d}{2}\right)C\exp\left(-h_2\left|y + \frac{d}{2}\right|\right)\exp(j\omega t - j\beta x) \qquad y \le -d\ ,\ y \ge 0 \tag{2.10}$$

for antisymmetric TE-waves. It is seen that the field outside the dielectric is an exponential decaying function of the distance from the dielectric slab. For the magnetic field components see Ref. [7].

Further, continuity of the electric and magnetic field components across the dielectric-air interface leads to the following characteristic equations [7]:

$$\tfrac{1}{2}h_2 d = \tfrac{1}{2}h_1 d \tan\tfrac{1}{2}h_1 d \tag{2.11}$$

for symmetric TE-waves and

$$\tfrac{1}{2}h_2 d = -\tfrac{1}{2}h_1 d \cot\tfrac{1}{2}h_1 d \tag{2.12}$$

for antisymmetric TE-waves.

With $U=h_1 d/2$ and $W=h_2 d/2$ both the symmetric and antisymmetric TE-waves should satisfy the following relationship:

$$U^2 + W^2 = \tfrac{1}{4}(h_1 d)^2 + \tfrac{1}{4}(h_2 d)^2 = \tfrac{1}{4}\omega^2 \mu_0 \varepsilon_0 d^2(\varepsilon_{rd}-1) \triangleq \nu^2 \tag{2.13}$$

where ν is called the normalized frequency. The solutions to Equation (2.11) or (2.12) and (2.13) for $W \geq 0$ are called modes. When the value of W is smaller than zero the field will explode outside the dielectric slab and this is physically not acceptable. This can be seen in Equations (2.8) and (2.10). The symmetric modes are denoted by TE_m, with $m = 0,2,4...$, while for the antisymmetric modes odd values of m are used. A graphical method for solving the characteristic equations is illustrated in Figure 2.2. In this figure the possible substrate modes of a $0.31\lambda_0$ thick silicon slab are given. It is seen that only three transverse electric modes can propagate in this slab, because the other mathematical solutions require values of W smaller than zero.

At the cut-off frequency $W=h_2 d/2=0$, which means that $h_1 d/2=m\pi$, with $m = 0,1,2,3$ etc. If these two equations are substituted into Equation (2.13), the following cut-off thickness for the TE_m-mode is obtained:

$$\left(\frac{d}{\lambda_0}\right)_{co} = \frac{m}{2\sqrt{\varepsilon_{rd} - 1}} \qquad m = 0,1,2,3... \tag{2.14}$$

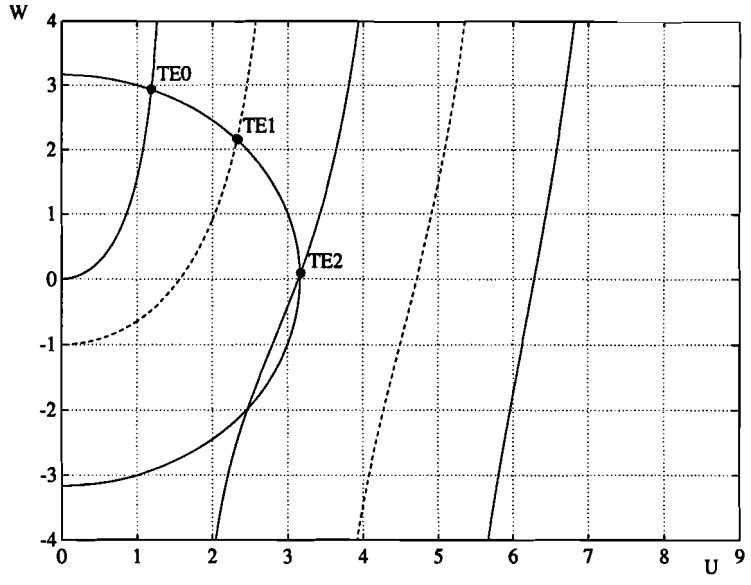

***Figure 2.2** : Graphical solutions for the characteristic equations with $d/\lambda_0 = 0.31$ and $\varepsilon_{rd} = 11.7$.*

Rewriting this equation results in the frequency at cut-off and for this cut-off frequency of the m-th substrate mode it is possible to write:

$$f_{co,m} = c_0 \frac{m}{2d\sqrt{\varepsilon_{rd} - 1}} \qquad m = 0,1,2,3... \tag{2.15}$$

with c_0 the speed of light in vacuum.

Figure 2.3 shows the propagating TE-modes for a quartz and a silicon substrate as a function of the slab thickness relative to the wavelength in the air. Now that the possible modes in a dielectric slab of thickness d are known, the total substrate-mode power can be calculated if the input source is given. As an example, the power lost to these propagating modes is calculated in Ref. [6] for an elementary dipole and an elementary slot antenna. It appears that when the substrate thickness increases the total substrate-mode power approaches a limit value; the only difference is the power distribution among each individual mode. For thick dielectric substrates however, it is not necessary to use the theory of modes to determine the total substrate-mode power. In this case the theory of Geometrical Optics can be applied to calculate the total power contained in these modes. The equivalence between the substrate-mode theory and the theory of Geometrical Optics is shortly treated in the next section.

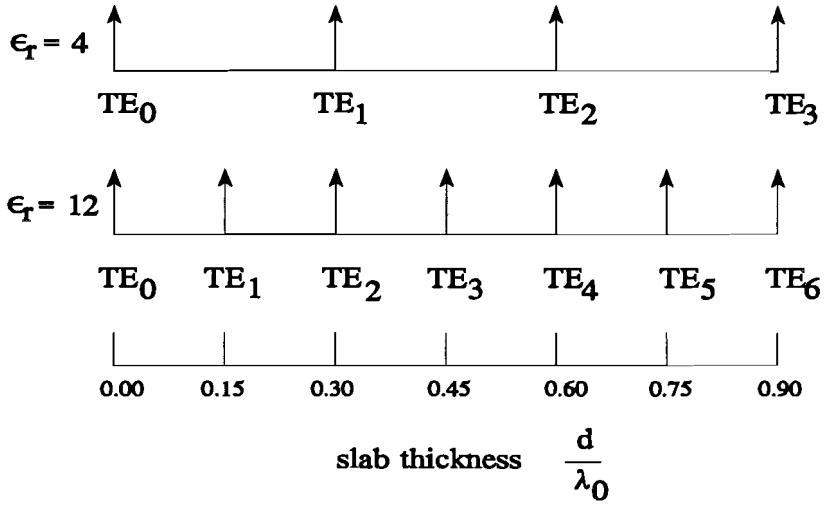

Figure 2.3 : Propagating modes in an ungrounded dielectric slab.

2.1.2 Geometrical Optics interpretation

Equations (2.7) and (2.9), which describe the electric field for symmetric and antisymmetric waves in a dielectric slab of thickness d, can be written in the following forms:

$$E_{zd} = \frac{A}{2}\exp(j(\omega t + h_1(y+\frac{d}{2}) - \beta x)) + \frac{A}{2}\exp(j(\omega t - h_1(y+\frac{d}{2}) - \beta x)) \qquad (2.16)$$

for symmetric TE-waves and

$$E_{zd} = \frac{B}{2j}\exp(j(\omega t + h_1(y+\frac{d}{2}) - \beta x)) - \frac{B}{2j}\exp(j(\omega t - h_1(y+\frac{d}{2}) - \beta x)) \qquad (2.17)$$

for antisymmetric TE-waves.

From these equations it can be seen that the electric field is a superposition of two uniform plane waves with an angle of propagation of θ and $-\theta$, where θ is the angle with the negative y-axis. For θ it is possible to write: $\tan\theta = \beta/h_1$.

The phase constant of a proper mode (which can exist) can be derived from Equations (2.5), (2.6) and (2.13) yielding

$$\beta(\omega) = \sqrt{\omega^2 \mu_0 \varepsilon_0 + h_2^2} = k_0 \sqrt{1 + \frac{h_2^2}{k_0^2}} \tag{2.18}$$

At the cut-off frequency $h_2 = 0$, therefore

$$\frac{\beta(\omega_c)}{k_d} = \frac{k_0}{k_d} = \frac{1}{n_d} = \sin\theta_c \tag{2.19}$$

So, it is clear that at cut-off the angle of incidence on the interface between the dielectric slab and the air equals the critical angle for total internal reflection. If the frequency is lower than the cut-off frequency, the rays are not totally reflected. For a proper mode, it is necessary for the angle θ to be greater than the critical angle.

As already stated, with the theory of Geometrical Optics the total substrate-mode power in a thick dielectric slab can be calculated by integrating the radiation pattern of the antenna (in the dielectric) over all angles greater than the critical angle. Of course not only the substrate-mode losses can be determined by using the radiation pattern, but also the field at the second dielectric-air interface.

2.2 Radiation patterns

To calculate the radiation pattern of the integrated antenna in the dielectric slab, it is assumed that the radiation pattern in a thick slab (second dielectric-air interface in the far-field of the feed) can be approximated by the radiation pattern of the same antenna in a dielectric half-space. It has already been explained that antennas on top of thick dielectric substrates lose power to substrate modes and that this loss can be calculated from the radiation pattern of the antenna. Therefore, it is important to find these patterns for different kind of antennas placed on top of some dielectric half-space (or thick slab).

The planar antennas to be used as a feed are a slot, a double-slot and a double-dipole antenna with a backing reflector. Both the E- and H-plane radiation patterns are calculated and silicon ($\varepsilon_r = 11.7$), fused quartz ($\varepsilon_r = 4$) and high density polyethylene ($\varepsilon_r = 2.31$) are used as dielectric materials. The double-slot and double-dipole antenna are chosen, because it would give us the opportunity to compare our results with results obtained by Filipovic [1] and Skalare [8]. In

this section the coordinate system of Figure 2.1 is shifted by d in the y-direction for mathematical convenience, so that in the following the antenna is located in the origin.

2.2.1 Slot antenna

The first antenna that is considered is a single-slot antenna, which is placed parallel to the z-axis. A picture of this type of antenna can be seen in Figure 2.7, where two of these slot elements are placed together. For a short slot ($dz \ll \lambda$) in some medium the far-field E- and H-components can be written as [9]:

$$E_\phi = \frac{jk_e I dz \sin\theta}{4\pi R} \exp(j\omega t - jk_e R) \tag{2.20}$$

$$H_\theta = -\frac{E_\phi}{Z_e} \tag{2.21}$$

with θ the angle with the z-axis, $k_e = k_d = 2\pi/\lambda_d$ for a dielectric medium and $k_e = k_0 = 2\pi/\lambda_0$ for air. The wave impedance of the medium is denoted by $Z_e = \sqrt{\mu_0/\varepsilon_d}$. Next, patterns of longer slot antennas will be calculated assuming a sinusoidal magnetic current distribution in the slot. The wavelength of this current distribution is the mean wavelength [10] given by $\lambda_m = \lambda_0/\sqrt{\varepsilon_m}$ with $\varepsilon_m = (1+\varepsilon_r)/2$. Then for the current in the slot it is possible to write:

$$I = I_m \sin[k_m(l - |z|)], \qquad -l \le z \le l \tag{2.22}$$

with $k_m = 2\pi/\lambda_m$ and $2l$ the length of the slot antenna. Because of the metal plane between the dielectric and the air, the slot antenna radiates as if it was entirely placed in the dielectric or air, depending on whether the radiation pattern in the dielectric or the air is needed. Of course the sum of the power radiated in the air and in the dielectric must equal the total radiated power by the slot. The total electric field in some point located in the far field of the antenna, can be expressed as:

$$E_\phi = \frac{jk_e I_m \sin\theta}{4\pi} \int_{-l}^{l} \frac{\sin[k_m(l - |z|)]}{R'} \exp(-jk_e R') dz \tag{2.23}$$

The time dependence $e^{j\omega t}$ will further be omitted in this report. In Equation (2.23) R' is the distance from a point on the antenna to a far-field observation point. At a large distance from the slot, the difference between R and R' can be neglected regarding its effect on the amplitude although its effect on the phase must be taken into account.

For R' can be written:

$$R' = R - z\cos\theta \tag{2.24}$$

Using Equation (2.24) and evaluating the integral reduces Equation (2.23) to:

$$E_\phi = \frac{2jk_e k_m I_m \sin\theta}{4\pi R}\left[\frac{\cos(k_e l\cos\theta)-\cos(k_m l)}{k_m^2 - k_e^2\cos^2\theta}\right]\exp(-jk_e R) \tag{2.25}$$

The radiation intensity is defined as the power radiated per unit solid angle and can be calculated as:

$$P(\theta,\phi) = \tfrac{1}{2}R^2 Re[\underline{E}\,x\,\underline{H}^*] = \frac{R^2|E(R,\theta,\phi)^2|}{2Z_e} \tag{2.26}$$

Next the directive gain function or power pattern $G(\theta,\phi)$ can be found, simply by dividing the radiation intensity of the selected antenna by the radiation intensity of an isotropic radiator, with the same input power (P_{tot}). Thus,

$$G(\theta,\phi) = 4\pi\frac{P(\theta,\phi)}{P_{tot}} \tag{2.27}$$

with

$$P_{tot} = \int_0^{2\pi}\int_0^{\pi} P(\theta,\phi)\sin\theta\, d\theta\, d\phi \tag{2.28}$$

The input power (P_{tot}) is equal to the total radiated power by the feed antenna. If Equations (2.25) and (2.26) are substituted into Equation (2.27) the directive gain function of the slot antenna, on top of a dielectric half-space, is obtained:

$$G(\theta,\phi) = \frac{k_e^2 k_m^2 I_m^2 \sin^2\theta}{2\pi Z_e P_{tot}}\left[\frac{\cos(k_e l\cos\theta)-\cos(k_m l)}{(k_m^2 - k_e^2\cos^2\theta)}\right]^2 \tag{2.29}$$

It is good to note here that the input power P_{tot} is a function of the magnetic current amplitude I_m. In the E-plane the power pattern is constant, because $\theta = \pi/2$ and the pattern is independent of ϕ. In the H-plane on the other hand, it is obvious that the pattern is not uniform but varies with the angle θ.

Power patterns have been calculated for one frequency (246 GHz) and three different relative dielectric constants ($\varepsilon_r = 2.31$, 4 and 11.7). This frequency is chosen to compare our results with the results obtained by Filipovic et al. [1], further on in this report. The length of their slot antennas on silicon was $0.28\lambda_0$. In Figures 2.4 to 2.6 these patterns have been plotted and both the radiation in the air and in the dielectric half-space are shown. It appears that the beamwidth into the dielectric is always narrower than the beamwidth into the air. For the directivity at the dielectric side it may be concluded that it increases when the relative dielectric constant of the dielectric increases. The computed directivity is 6.1 dBi for silicon, 4.7 dBi in case of quartz and 3.9 dBi when a HDP dielectric is used. Of course this is partially due to the backward radiation losses. For example the power radiated into the air contains 3.2% and 22.8% of the total radiated power, when silicon or HDP is used, respectively. The discontinuities in Figures 2.4 to 2.6 at angles of -90 and 90° from boresight can physically exist, because of the metal ground plane between both media. This implies that a net current will flow through the metal as a result of the different field strengths at both sides of the ground plane.

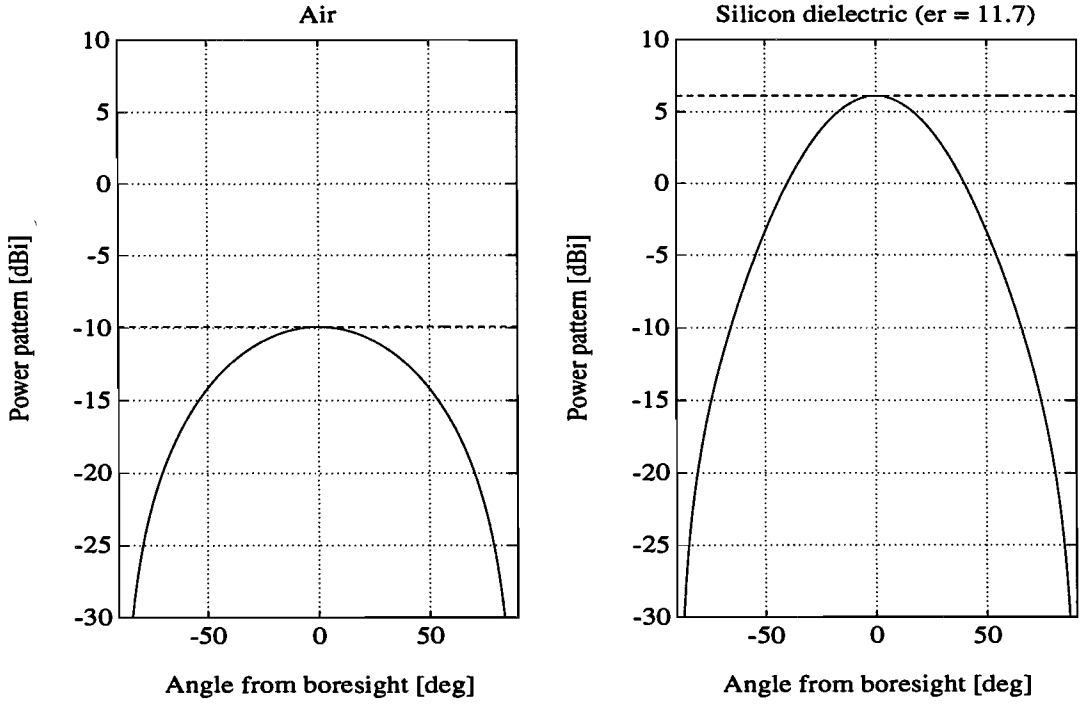

Figure 2.4 : Power patterns of a slot antenna in the air and in a silicon dielectric half-space at a frequency of 246 GHz (solid line: H-plane, and dashed line: E-plane).

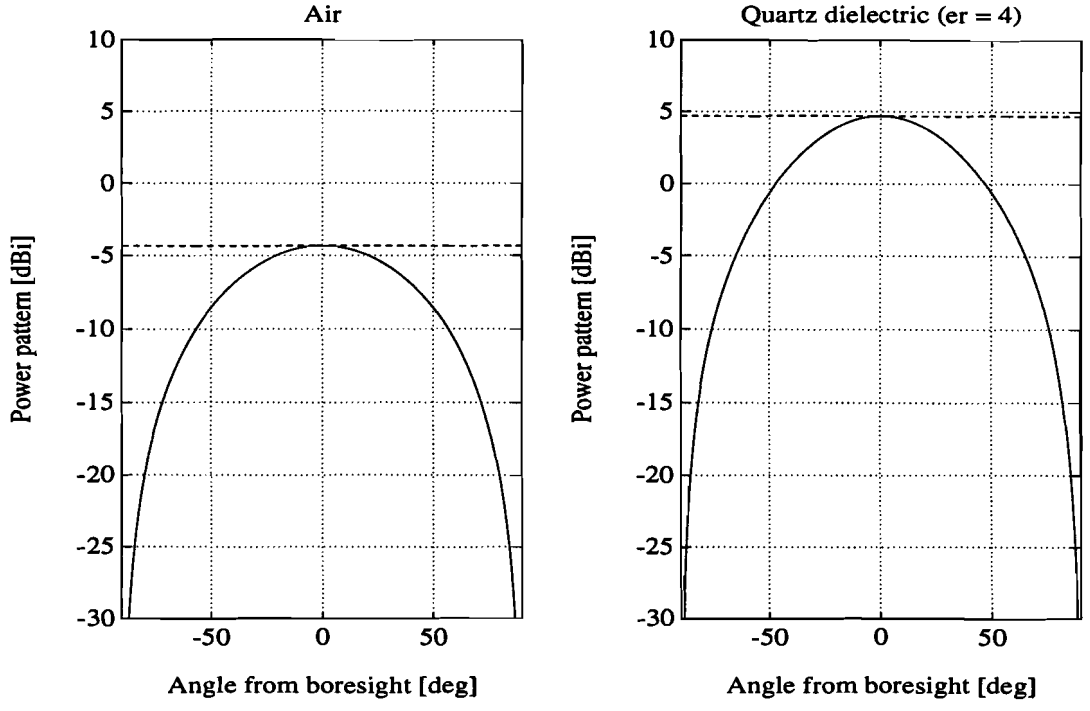

***Figure 2.5** : Power patterns of a slot antenna in the air and in a quartz dielectric half-space at a frequency of 246 GHz (solid line: H-plane, and dashed line: E-plane).*

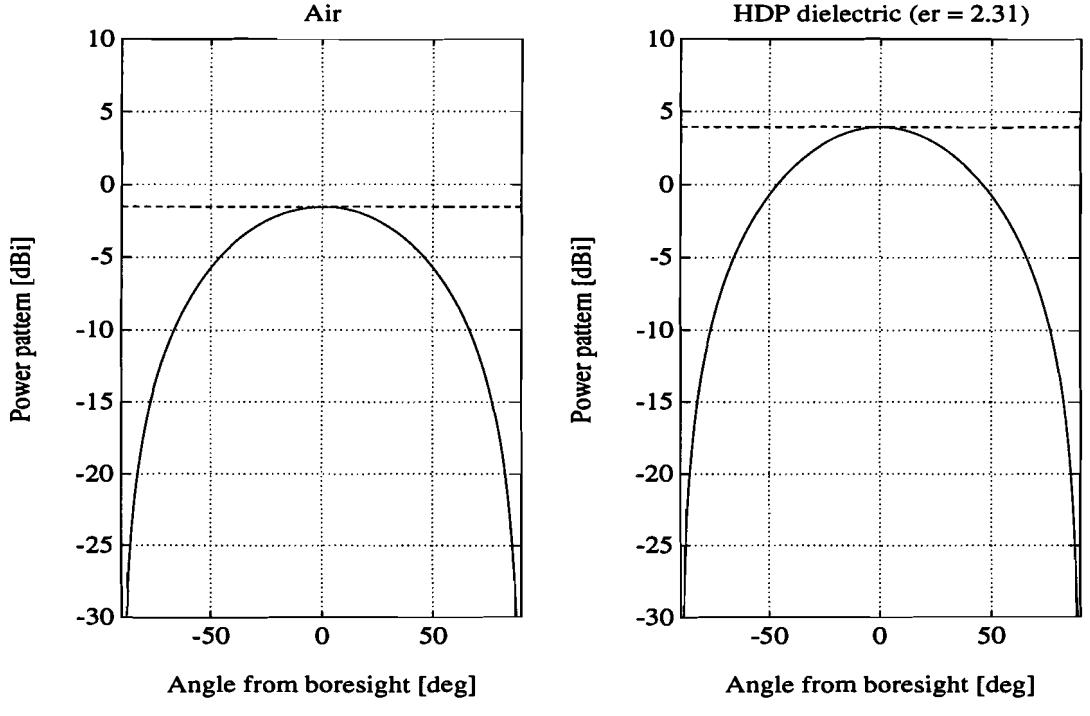

***Figure 2.6** : Power patterns of a slot antenna in the air and in a HDP dielectric half-space at a frequency of 246 GHz (solid line: H-plane, and dashed line: E-plane).*

Because the E-plane pattern is constant in the air and in the dielectric, the single slot is not very useful as feed for the actual integrated lens antenna. One way to solve this inconvenience is to make an array of two equal slot antennas. Such an antenna is called a double-slot antenna and will be discussed in the next section.

2.2.2 Double-slot antenna

The antenna array, which is mounted on top of the dielectric half-space, lies in the xz-plane and each slot element is placed parallel to the z-axis. Figure 2.7 shows a picture of such a planar double-slot antenna.

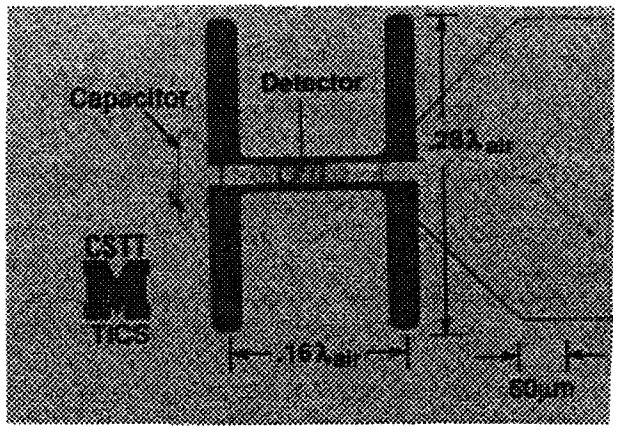

***Figure 2.7** : Picture of a double-slot antenna on top of a silicon dielectric [1].*

The double-slot antenna power patterns are calculated in a similar way as the power patterns of the single-slot antenna, except for the inclusion of an array factor. For the element pattern Equation (2.25) is used. The array factor in the x-direction can be determined by [11]:

$$AF_x = \left[\frac{E}{n_x E_0}\right] = \left[\frac{\sin\frac{1}{2}n_x\psi_x}{n_x\sin\frac{1}{2}\psi_x}\right] \tag{2.30}$$

In Equation (2.30) $n_x=2$ and $\psi_x=k_e\Delta d\cos\phi\sin\theta$, so that it is possible to write:

$$AF_x = \cos(\tfrac{1}{2}k_e\Delta d\cos\phi\sin\theta) \tag{2.31}$$

for the array factor, where ϕ is the angle from the x-axis in the xy-plane and Δd the spacing between the two slot antennas. The E-plane is given by $\theta = \pi/2$ and the H-plane by $\phi = \pi/2$, which means that the array factor is constant in the H-plane. The directive gain function of the double-slot antenna can be written as:

$$G(\theta,\phi) = \frac{k_e^2 k_m^2 I_m^2 \sin^2\theta}{2\pi Z_e P_{tot}} \cos^2\left(\frac{1}{2}k_e \Delta d \cos\phi \sin\theta\right) \left[\frac{\cos(k_e l\cos\theta) - \cos(k_m l)}{(k_m^2 - k_e^2\cos^2\theta)}\right]^2 \qquad (2.32)$$

To show the difference between the radiation patterns of a slot and a double-slot antenna, also the powers patterns in the air and in the dielectric half-space of the latter are computed. Figures 2.8 to 2.10 all are calculated for a frequency of 246 GHz. The spacing Δd between the slot elements is so chosen that the power pattern in the E-plane is nearly the same as the power pattern in the H-plane (in the dielectric), for angles smaller than approximately 30 to 50°, depending on the dielectric material being used. This results in a spacing Δd of $0.16\lambda_0$ in case of a silicon dielectric, $0.20\lambda_0$ with quartz and $0.25\lambda_0$ when HDP is used as substrate material.

From Figures 2.8 to 2.10 it can be seen that the directivity (10.5 dBi) is approximately 3.4 dB higher when silicon is used instead of quartz. The directivity in the HDP dielectric has a value of 6.0 dBi, which is the smallest of the three. This can be explained by the fact that the power radiated in the air is only 9.9% of the total radiated power with the silicon dielectric, while the double-slot antenna on quartz radiates 17.7% of the total power directly into the air. This even increases to 28.6% in case of a HDP substrate.

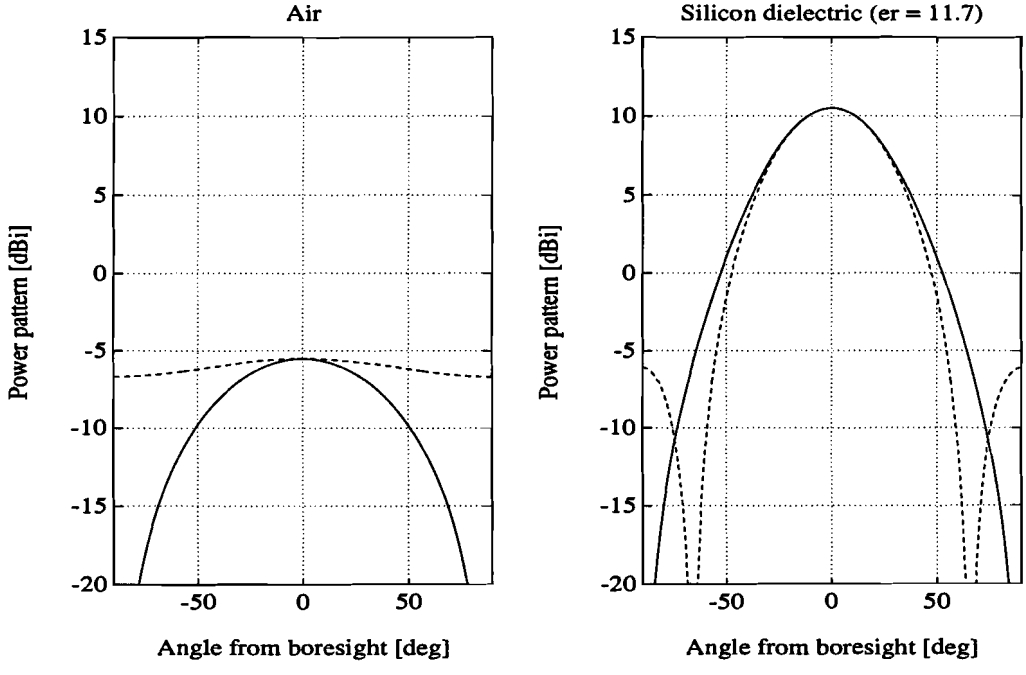

***Figure 2.8** : Power patterns of a double-slot antenna in the air and in a silicon dielectric half-space at a frequency of 246 GHz (solid line: H-plane, and dashed line: E-plane).*

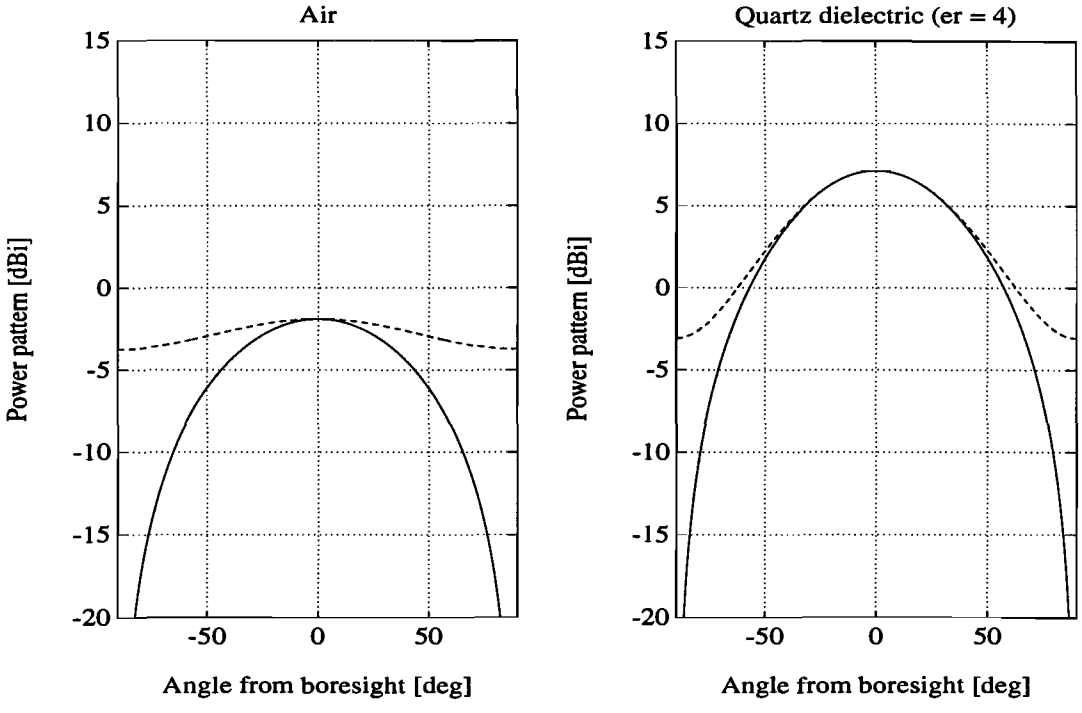

***Figure 2.9** : Power patterns of a double-slot antenna in the air and in a quartz dielectric half-space at a frequency of 246 GHz (solid line: H-plane, and dashed line: E-plane).*

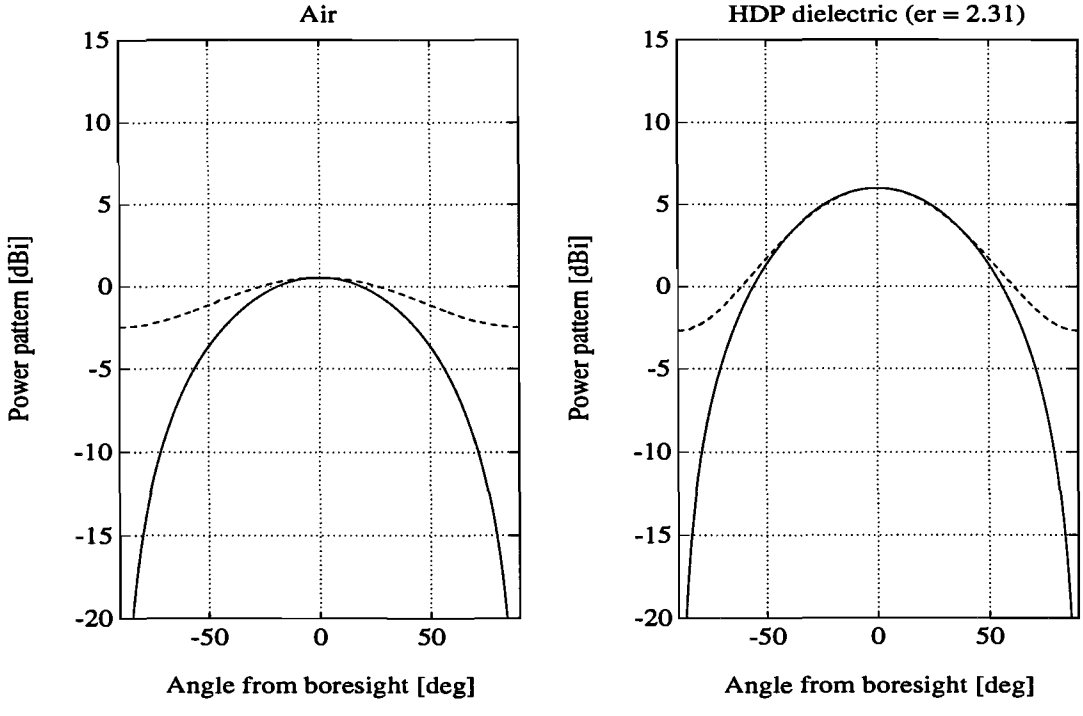

***Figure 2.10** : Power patterns of a double-slot antenna in the air and in a HDP dielectric half-space at a frequency of 246 GHz (solid line: H-plane, and dashed line: E-plane).*

A comparison between the radiation patterns of the single- and the double-slot antenna shows that the difference in directivity is not equal to 3 dB, but varies with the different configurations. Normally, when an array of two elements is used instead of a single element, a directivity improvement of 3 dB is obtained. The reason for this apparent contradiction is, that the two slot antennas are placed too close to each other to neglect the mutual coupling. This mutual coupling affects the radiation resistance of the single-slot elements in such a way that with the same input power the field strength in the forward direction changes as a function of the distance between the elements.

As an example, the directivity improvement of a double-slot antenna compared to a single-slot antenna is calculated as a function of the distance between the two elements, as shown in Figure 2.11. The double-slot antenna is placed on top of a silicon dielectric substrate. To indicate the improvement of an array of two elements, with no mutual coupling between the elements, the dashed line in Figure 2.11 is used.

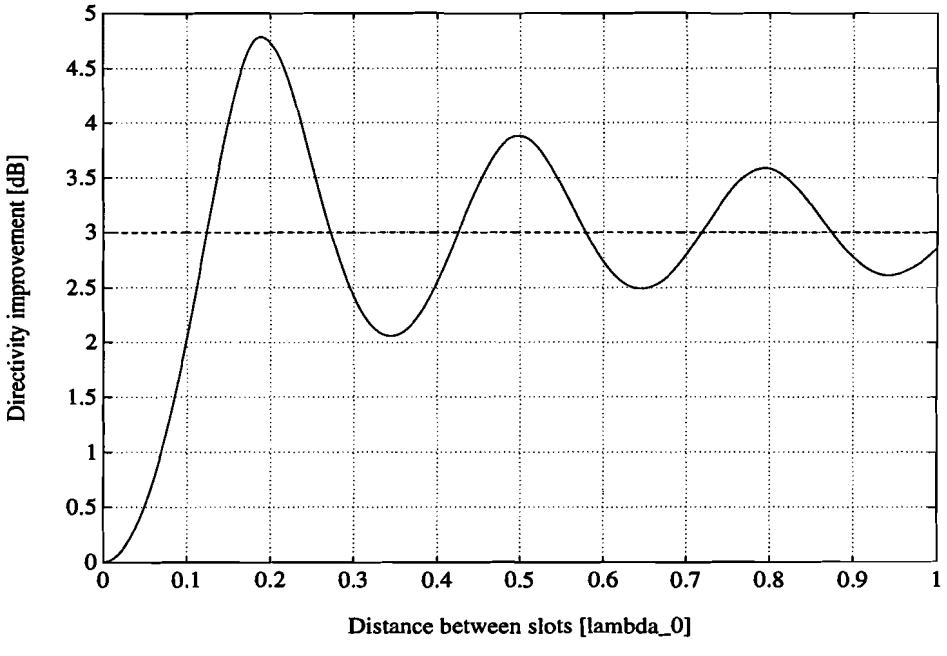

***Figure 2.11** : Directivity improvement of a double-slot antenna compared to a single-slot antenna at 246 GHz, when the antenna is put on a silicon dielectric ($2l = 0.28\ \lambda_0$).*

The directivity-improvement curve of the double-slot antenna can be explained by two simple cases. Firstly, as the distance between the slot elements approaches zero the two elements become a single-slot antenna and the directivity improvement then is 0 dB. If, on the other hand, the distance between the two slot elements is increased to values where the mutual

coupling is zero, the improvement in directivity becomes 3 dB. This 3-dB value is the normal directivity improvement of an array of two elements compared to a single element. When the distance is between zero and infinite (or a few wavelengths) the directivity-improvement curve oscillates around 3 dB. The mutual coupling between the slot elements is the cause for this oscillation. Now it is clear that the directivity improvement of the double-slot antenna on silicon is more than 3 dB, as seen from Figure 2.11, when the distance between the elements is 0.16 λ_0. In fact the improvement is close to 4.4 dB.

2.2.3 Double-dipole antenna with a backing reflector

From the previous antenna type, being a magnetic dipole, it has become clear that a substantial part of the input power is directly radiated into the air. Of course this is a power-loss factor, which should be diminished. Therefore, in this section a double-dipole (electric) antenna is considered, which has a perfectly conducting metal plane at a distance s from the antenna. As an illustration such a double-dipole antenna is shown in Figure 2.12.

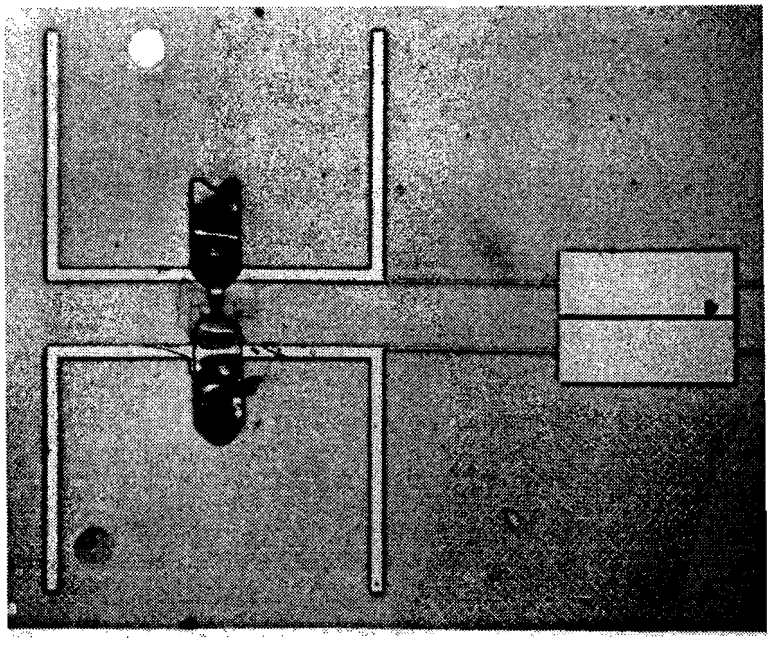

***Figure 2.12** : Picture of a double-dipole antenna on top of a dielectric substrate [6].*

The reflector prevents that some of the total power will be directly radiated into the air and of course this will increase the directivity of the antenna. With image theory, as seen in Figure 2.13, the reflector can be replaced by two dipole antennas which have the same radiation patterns as the real dipole antennas, only a phase shift of π radian is introduced for horizontal polarization (antenna parallel to the reflector). Of course the distance between the antenna and its image is much smaller than the thickness of the dielectric slab. The calculation of the radiation pattern in a dielectric half-space becomes much easier now, because the antenna is entirely surrounded by the dielectric medium.

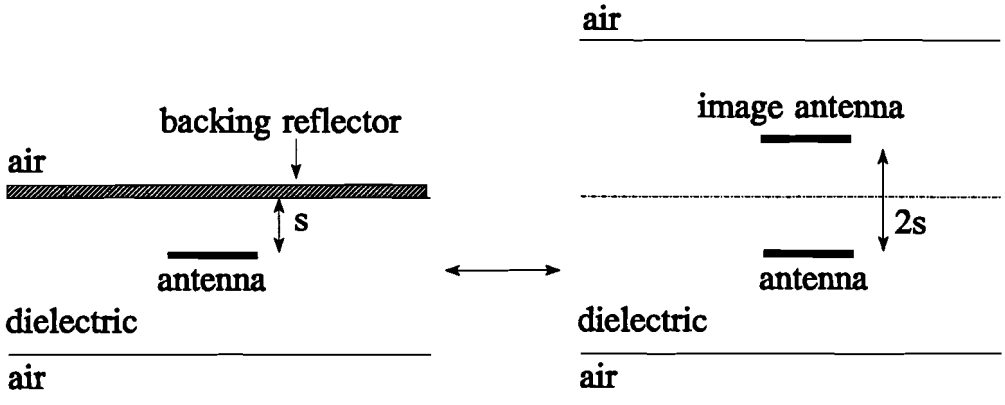

***Figure 2.13** : Equivalent configuration with image theory.*

It is started by calculating the far-field E-component of a double-dipole in a dielectric medium. Both dipoles are polarized in the z-direction ($-l \le z \le l$) and have a spacing of Δd in the x-direction. The field of a single dipole can be expressed as [9]:

$$E_\theta = \frac{jZ_d I_e}{2\pi R} \frac{\cos(k_d l \cos\theta) - \cos(k_d l)}{\sin\theta} \exp(-jk_d R) \tag{2.33}$$

To obtain the total field of the dipole array, only the field of the single dipole has to be multiplied by an array factor in the x-direction. This array factor is given by Equation (2.31), which results in the following electric field:

$$E_\theta = \frac{jZ_d I_e}{2\pi R} \frac{\cos(k_d l \cos\theta) - \cos(k_d l)}{\sin\theta} \cos(\tfrac{1}{2} k_d \Delta d \cos\phi \sin\theta) \exp(-jk_d R) \tag{2.34}$$

The reflector behind the double-dipole antenna also introduces an array factor, but this time

in the y-direction. The spacing between the real double-dipole and its image antenna is $2s$. This results in the following array factor in the y-direction:

$$AF_y = \cos\left(sk_d \sin\phi \sin\theta + \frac{\pi}{2}\right) \tag{2.35}$$

Multiplication of Equations (2.34) and (2.35) yields the electric field for a double-dipole antenna with a backing reflector in a dielectric half-space as:

$$E_\theta = \frac{jZ_d I_e}{2\pi R} \frac{\cos(k_d l \cos\theta) - \cos(k_d l)}{\sin\theta} \cos(\tfrac{1}{2} k_d \Delta d \cos\phi \sin\theta) *$$

$$\cos\left(sk_d \sin\phi \sin\theta + \frac{\pi}{2}\right) \exp(-jk_d R) \tag{2.36}$$

Finally, the power pattern can be calculated with Equations (2.26) to (2.28). For the computations of the next power pattern plots the antenna is placed within a silicon dielectric and the reflector is responsible for a zero radiation pattern in the air. One of the demands is that the patterns in the E- and H-plane will be nearly the same (for small angles) and therefore the following two double-dipole antennas are considered. In the first example an array of two dipoles is used with a length of $0.5\lambda_d$ (half-wave dipoles) and a spacing $0.4\lambda_d$, while the second double-dipole has a length of $0.80\lambda_d$ and the dipoles are now separated by $0.49\lambda_d$. In Figure 2.14 and 2.15 the calculated power patterns are shown. The distance between the dipole array and the backing reflector is $0.25\lambda_d$ in both cases.

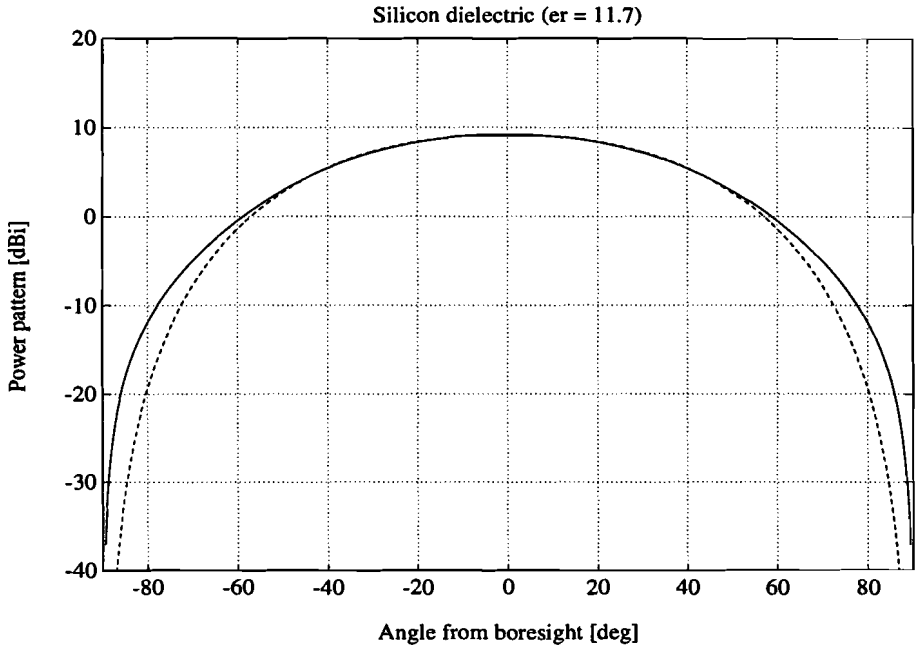

***Figure 2.14** : Power patterns of a double-dipole antenna ($2l=0.5\lambda_d$ and $\Delta d=0.4\lambda_d$) with a backing reflector in a silicon half-space at a frequency of 246 GHz (solid line: H-plane, and dashed line: E-plane).*

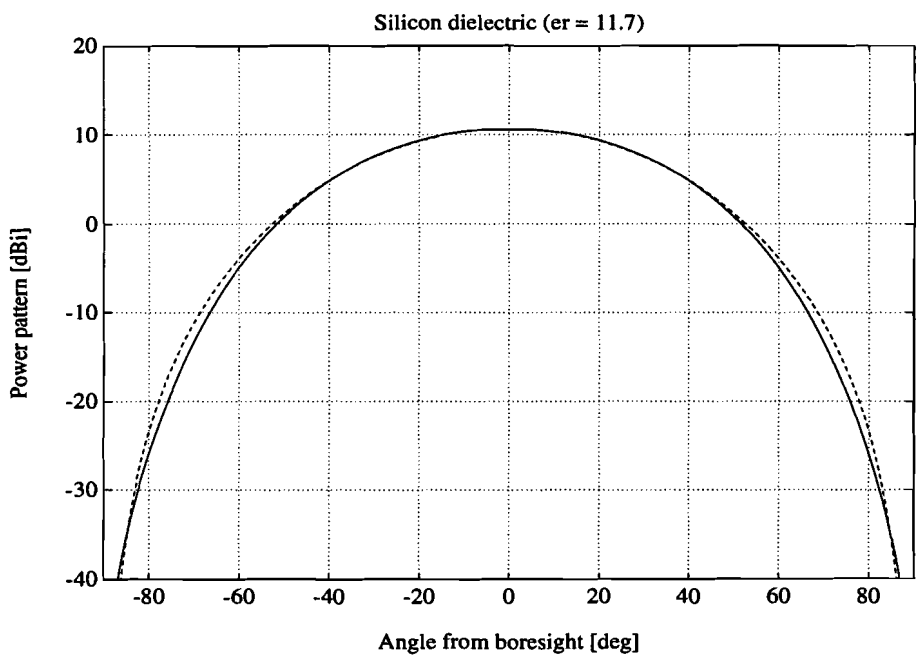

***Figure 2.15** : Power patterns of a double-dipole antenna ($2l=0.8\lambda_d$ and $\Delta d=0.49\lambda_d$) with a backing reflector in a silicon half-space at a frequency of 246 GHz (solid line: H-plane, and dashed line: E-plane).*

It appears that the directivity of the double-dipole antenna with the longest dipoles is almost 1.0 dB higher. Of course, this corresponds to the smaller beamwidth of the second dipole array. For the array with the half-wave dipole elements the 10-dB beamwidth is around 120°, while for the largest array this beamwidth has a value of 100° at the same frequency of 246 GHz. Also for both designs can be said that the E- and H-plane patterns are equal up to an angle of 50° from boresight.

3. Integrated lens antennas

If an antenna is put on top of a dielectric substrate, it is clear that the substrate-mode losses have to be diminished to achieve the best performance. In fact, most of the power transmitted by the planar antenna should be radiated through the dielectric into the air, and not be trapped as substrate modes. One way to solve the problem of these substrate modes is to make the slab very thin, which reduces the number of propagating modes. However, this has the disadvantage that the slab will become too fragile. It has to be stated here that one has made such designs with thin dielectric membranes [12]. Another very attractive solution is to mount a lens with the same index of refraction at the bottom of the dielectric slab. The shape of the lens then should be elliptical or something close to elliptical to guarantee that no power (little power) will be lost to substrate modes. This can be explained by the fact that, because of the shape of the lens, the angle of incidence of the incident wave will be smaller than when the dielectric slab has a flat surface, so less power will be reflected at the dielectric-air interface. The lens also bends the rays radiated by the planar antenna more towards the boresight direction, thereby sharpening the power pattern and effectively increasing the directivity of the integrated lens antenna [12]. In this chapter an elliptical and an extended hemispherical lens will be analyzed.

3.1 Theoretical analysis of the lens antenna

First the theoretical analysis of a planar antenna on top of a dielectric slab, with an arbitrarily mounted lens, will be treated here. The mounted lens is assumed to have the same dielectric constant as the slab, and here its shape is not yet defined. In Figure 3.1 a two-dimensional cross-section of such a lens-antenna combination is shown.

In the following, the feed antenna which illuminates the lens is either a double-slot or a double-dipole antenna with a backing reflector, which is normally some kind of thin metal plate. In Figure 3.1 only a cross-section of the integrated lens antenna is shown, because the shape of the lens is rotationally symmetric around the y-axis. Without any specific reason it is chosen that the center of the dielectric lens is always placed on top of the slab. The symbols used in Figure 3.1 will be explained later.

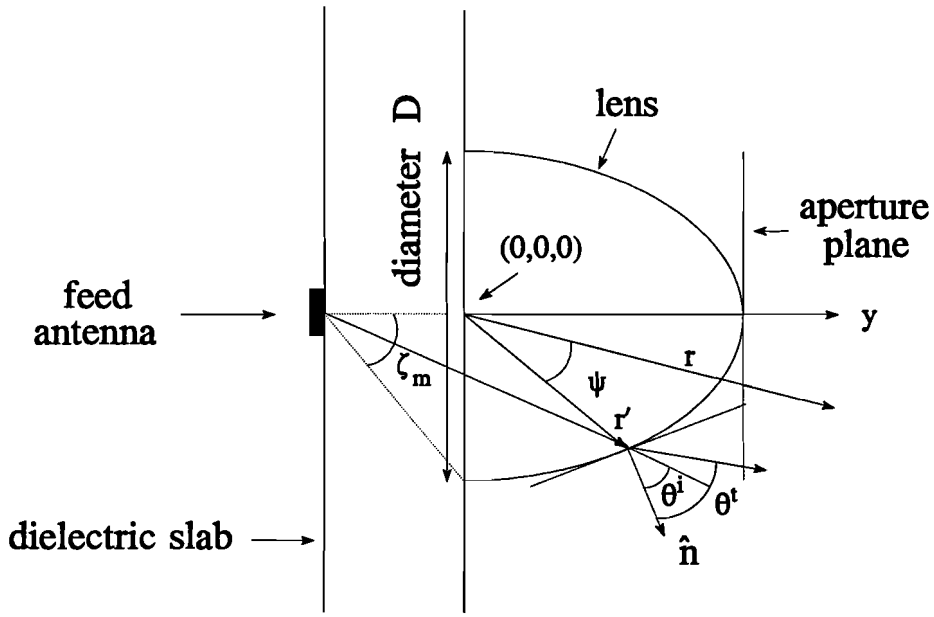

Figure 3.1 : Planar antenna on a dielectric slab with a mounted lens.

The theoretical analysis of the integrated lens antenna will contain the following antenna properties.

* Far-field radiation patterns
* Directivity
* Antenna efficiencies:
    - aperture efficiency (only in a focused system)
    - polarization efficiency (only in a focused system)
    - combined aperture efficiency (only in a non-focused system)
    - spillover efficiency
    - transmission efficiency
* Beam efficiency
* Gaussian beam efficiency

It is noted that if the lens does not convert the incident wave into a plane wave, the aperture and polarization efficiency are not calculated separately. This means that only the product of these two efficiencies will be determined when the directivity and the other antenna efficiencies are known. In a non-focused lens-antenna system, which means that the phase distribution in the aperture plane is not uniform, the product of the aperture and polarization

efficiency will be called the combined aperture efficiency.

3.1.1 Far-field radiation patterns

In the previous chapter the radiation patterns of different feed antennas mounted on a dielectric half-space (thick slab) have been calculated. Now, the half-space is replaced by some kind of dielectric lens and a second dielectric-air interface is introduced. The electric and magnetic fields at the second dielectric-air interface (lens surface) are computed using a ray-analysis technique [13], where the radiation pattern of the feed in the dielectric is needed. It is good to note here that this analysis is not limited to the antenna types considered, but it is possible to calculate the far-field radiation patterns with any feed antenna, when its radiation properties into the dielectric are known. Using the far-field pattern of these feed antennas implies that the lens surface is supposed to be far away from the feed, so that the feed antenna can be treated as a point source. Planar antennas that can be used as a feed are for example a double-slot, a double-dipole with a backing reflector, a spiral or a log-periodic antenna. In this report only the two narrowband antennas are treated.

Once the electric and magnetic fields at the lens-air interface are known, these fields have to be decomposed, for a certain ray, into parallel ($\parallel$) and perpendicular ($\perp$) components to obtain the fields just outside the dielectric lens. Each component then must be multiplied by the appropriate Fresnel transmission coefficient. The transmission (τ) and reflection coefficients (ρ) are calculated in Appendix A as:

$$\rho_{\perp} = \frac{Z_2\cos\theta^i - Z_1\cos\theta^t}{Z_2\cos\theta^r + Z_1\cos\theta^t} \tag{3.1}$$

$$\tau_{\perp} = \frac{Z_2\cos\theta^i + Z_2\cos\theta^r}{Z_2\cos\theta^r + Z_1\cos\theta^t} = 1+\rho_{\perp} \tag{3.2}$$

$$\rho_{\parallel} = \frac{Z_1\cos\theta^i - Z_2\cos\theta^t}{Z_1\cos\theta^r + Z_2\cos\theta^t} \tag{3.3}$$

$$\tau_{\parallel} = \frac{Z_2\cos\theta^i + Z_2\cos\theta^r}{Z_1\cos\theta^r + Z_2\cos\theta^t} = (1+\rho_{\parallel})n \tag{3.4}$$

With Snell's laws θ^r and θ^t can be eliminated:

$$\theta^r = \theta^i \;,\; \beta_1 \sin\theta^i = \beta_2 \sin\theta^t \tag{3.5}$$

If the wave impedance $Z=\omega\mu_0/\beta=\omega\mu_0/(n\beta_0)$ and Equation (3.5) are substituted in Equations (3.1) to (3.4) the following reflection and transmission coefficients are obtained:

$$\rho_\perp = \frac{\cos\theta^i - \sqrt{(\frac{n_2}{n_1})^2 - \sin^2\theta^i}}{\cos\theta^i + \sqrt{(\frac{n_2}{n_1})^2 - \sin^2\theta^i}} \tag{3.6}$$

$$\tau_\perp = \frac{2\cos\theta^i}{\cos\theta^i + \sqrt{(\frac{n_2}{n_1})^2 - \sin^2\theta^i}} \tag{3.7}$$

$$\rho_\parallel = \frac{(\frac{n_2}{n_1})^2\cos\theta^i - \sqrt{(\frac{n_2}{n_1})^2 - \sin^2\theta^i}}{(\frac{n_2}{n_1})^2\cos\theta^i + \sqrt{(\frac{n_2}{n_1})^2 - \sin^2\theta^i}} \tag{3.8}$$

$$\tau_\parallel = \frac{2(\frac{n_2}{n_1})\cos\theta^i}{(\frac{n_2}{n_1})^2\cos\theta^i + \sqrt{(\frac{n_2}{n_1})^2 - \sin^2\theta^i}} \tag{3.9}$$

In the equations above, n is the index of refraction and θ^i is the angle of incidence measured from the normal towards the lens surface. The indices 1 and 2 refer to the dielectric and air side, respectively. After the fields have been multiplied by the appropriate transmission coefficients, the equivalent electric ($\underline{J}_s$) and magnetic ($\underline{M}_s$) current densities are determined just outside the dielectric surface. For these current densities it is possible to write [14]:

$$\underline{J}_s = \hat{n} \times \underline{H} \tag{3.10}$$

$$\underline{M}_s = -\hat{n} \times \underline{E} \tag{3.11}$$

where $\hat{n}$ is the normal to the lens surface.

When the far-field of the complete antenna (antenna plus lens) is considered, the transverse electric field components equal [14]:

$$E_\theta = -\frac{jk\exp(-jkr)}{4\pi r}(L_\phi + Z_0 N_\theta) \tag{3.12}$$

$$E_\phi = +\frac{jk\exp(-jkr)}{4\pi r}(L_\theta - Z_0 N_\phi) \tag{3.13}$$

where $\underline{N}$ and $\underline{L}$ in Equations (3.12) and (3.13) are defined by:

$$\underline{N} = \iint_S \underline{J}_s \exp(jkr'\cos\psi)\,dS \tag{3.14}$$

$$\underline{L} = \iint_S \underline{M}_s \exp(jkr'\cos\psi)\,dS \tag{3.15}$$

In Equations (3.14) and (3.15) S is the surface just outside the lens. The distance from the origin of the coordinate system to the equivalent electric and magnetic current densities is denoted by r', while r is the distance from the origin to the far-field observation point. The angle between $\underline{r}$ and $\underline{r}'$ is given by ψ.

3.1.2 Aperture field and antenna efficiencies

The field in the aperture of a focused lens-antenna system is calculated in a similar way as the field just outside the dielectric lens. Also a ray-analysis technique is applied, but now from the feed antenna to the aperture plane. Because the rays will leave the lens surface parallel to each other, no divergence factor is needed from the surface of the lens to the aperture plane. Only the phase of the field along a ray will change and the field strength itself not. The field in the aperture is needed for the calculation of the aperture and polarization efficiency. In a non-focused system, no unique planar aperture can be defined and consequently only the combined aperture efficiency will be calculated.

Once the antenna efficiencies are all known, it is possible to determine the directivity of the integrated lens antenna by the following equation:

$$\text{Directivity} = \left[\frac{\pi D}{\lambda_0}\right]^2 \eta_a \eta_s \eta_p \eta_{tr} \tag{3.16}$$

where D is the diameter of the circular aperture of the integrated lens antenna. The term directivity is used instead of gain, because the reflected power at the lens surface is not seen as some sort of loss and eventually comes out the lens contributing to the radiation pattern. Equation (3.16) is exactly the same as for a focused parabolic reflector antenna, except for the transmission efficiency which is needed to account for the reflected power at the lens surface.

The next problem is to calculate the different antenna efficiencies and the aperture efficiency will be treated first. For the computation of this efficiency the field in the aperture is needed and the complex electric field in the aperture will be denoted by $E(\rho,\delta)$, with ρ and δ being the polar coordinates in the aperture plane. The aperture efficiency describes the coupling of the antenna to a uniform plane wave and is calculated as:

$$\eta_a = \frac{4}{\pi D^2} \frac{\left| \int_0^{2\pi} \int_0^{D/2} E(\rho,\delta)\rho\, d\rho\, d\delta \right|^2}{\int_0^{2\pi} \int_0^{D/2} |E(\rho,\delta)|^2 \rho\, d\rho\, d\delta} \tag{3.17}$$

When the field in the aperture plane has a uniform phase and amplitude distribution, the aperture efficiency is unity, otherwise it will be smaller than one. Next the polarization efficiency is discussed. This efficiency indicates the part of the total power that is presented by the co-polarized field in the aperture. A polarization efficiency of one means that the field in the aperture in any point is polarized in the same direction as the antenna itself. For an arbitrarily polarized aperture field, the polarization efficiency is found by:

$$\eta_p = \frac{\left[\int_0^{2\pi} \int_0^{D/2} |E_{co}(\rho,\delta)| \rho\, d\rho\, d\delta \right]^2}{\left[\int_0^{2\pi} \int_0^{D/2} \sqrt{|E_{co}(\rho,\delta)|^2 + |E_{cr}(\rho,\delta)|^2}\, \rho\, d\rho\, d\delta \right]^2} \tag{3.18}$$

with E_{co} and E_{cr} the co- and cross-polarized field components, respectively.

The above-mentioned efficiencies are only calculated in a focused antenna system. However, the next efficiencies will be determined in a focused as well as in a non-focused lens-antenna system, because no unique aperture is needed.

The spillover efficiency contains information about the percentage of the total radiated power that is actually illuminating the lens surface and can be determined by the following equation:

$$\eta_s = \frac{\int_0^{2\pi}\int_0^{\zeta_m} P(\zeta,\delta)\sin\zeta\, d\zeta\, d\delta}{\int_0^{2\pi}\int_0^{\pi} P(\zeta,\delta)\sin\zeta\, d\zeta\, d\delta} \tag{3.19}$$

The angle δ is the angle in the xz-plane measured from the z-axis and ζ is the angle with the y-axis. The feed antenna is located in the origin of the coordinate system shown in Figure 3.2.

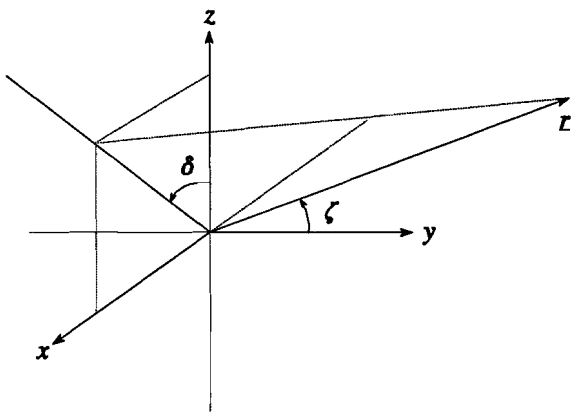

***Figure 3.2** : Coordinate system with the spherical coordinates (r, δ, ζ).*

For the maximum angle of a propagating ray that illuminates the lens, the symbol ζ_m is used. In Equation (3.19) the radiation intensity $P(\zeta,\delta)$ can be calculated with Equation (2.26). The last efficiency needed to determine the directivity of the integrated lens antenna is the transmission efficiency. This efficiency is defined as the total power after transmission divided by the total power illuminating the lens surface and is expressed as:

$$\eta_{tr} = \frac{\frac{1}{2}\int_S \int Re(\underline{E}_{tr} \times \underline{H}_{tr}^*)\cdot\hat{n}\, dS}{\int_0^{2\pi}\int_0^{\zeta_m} P(\zeta,\delta)\sin\zeta\, d\zeta\, d\delta} \tag{3.20}$$

with $\underline{E}_{tr}$ and $\underline{H}_{tr}$ the electric and magnetic fields just outside the lens surface. This lens surface is denoted by S.

3.1.3 Main beam and Gaussian beam efficiency

Because millimeter-wave integrated antennas have small collecting apertures, they usually are placed at the focal plane of a parabolic reflector. Then, some useful efficiency parameters for these feed antennas are the (main) beam efficiency and the Gaussian beam efficiency. The main beam efficiency is defined as the power within the main beam down to a certain level (-10 dB, -20 dB) divided by the total power radiated after transmission through the lens surface. The power radiated through the lens is found by multiplication of the total power radiated by the feed and the spillover and transmission efficiency. In formula form the beam efficiency is written as:

$$\eta_{beam} = \frac{\int_0^{2\pi}\int_0^{\zeta_e} G(\zeta,\delta)\sin\zeta\, d\zeta\, d\delta}{4\pi\eta_s\eta_{tr}} \tag{3.21}$$

The width of the main beam is denoted by ζ_e and this angle is constant for a rotationally symmetric main beam. In any other case it will depend on the angle δ.

Another important parameter in quasi-optical systems is the coupling efficiency between an antenna and a Gaussian beam. According to Ref. [12] a Gaussian beam allows nearly lossless propagation and conversion of an RF-signal using lenses, reflectors and quasi-optical components. From all Gaussian beams the first-order (fundamental) Gaussian beam is the most important one in quasi-optical systems, because it results in the smallest possible optics. Therefore, integrated antennas should be designed to couple highly to the first-order Gaussian beam. The Gaussian beam efficiency is calculated using a normalized inner product between the antenna radiation pattern and the Gaussian-beam pattern in the angular domain [15]. With the substitution of the appropriate field representations, the Gaussian beam efficiency can be written as:

$$\eta_{gaus} = \frac{\left|\iint[\hat{n}_{co}\cdot\underline{E}(\zeta,\delta)]\exp(-(\zeta/\zeta_0)^2)\exp(\pm j\pi(\zeta/\zeta_1)^2)\sin\zeta\, d\zeta\, d\delta\right|^2}{\iint|\underline{E}(\zeta,\delta)|^2\sin\zeta\, d\zeta\, d\delta \iint\exp(-2(\zeta/\zeta_0)^2)\sin\zeta\, d\zeta\, d\delta} \tag{3.22}$$

The polarization of the Gaussian beam is denoted by $\hat{n}_{co}$, which is $\hat{e}_x$ for the double-slot feed

and $\hat{e}_z$ for the double-dipole feed. In the calculation of the integrals only angles of ζ between -40 and 40° are used, because above these angles very little power is radiated by the integrated lens antenna. For large antenna apertures ($D \geq 2\lambda_0$) Equation (3.22) can also be written out in the near-field:

$$\eta_{gaus} = \frac{\left| \iint [\hat{n}_{co} \cdot \underline{E}(\rho,\delta)] \exp(-(\rho/w(y))^2) \exp(-jk(\rho^2/2\Re(y))) \rho \, d\rho \, d\delta \right|^2}{\iint |\underline{E}(\rho,\delta)|^2 \rho \, d\rho \, d\delta \iint \exp(-2(\rho/w(y))^2) \rho \, d\rho \, d\delta} \tag{3.23}$$

where the Gaussian beam is represented by its two-dimensional form, assuming circular symmetry. The waist and the radius of curvature of the Gaussian beam are denoted by $w(y)$ and $\Re(y)$, respectively.

When the Gaussian beam efficiency is calculated using the far-field patterns of the first-order Gaussian beam and the integrated lens antenna, it is clear that the waist and the radius of curvature in the aperture plane of the antenna are not directly known. However, in many cases it is necessary to have these values. For example, when the integrated lens antenna is part of a quasi-optical lens system. Therefore, relations between (ζ_0, ζ_1) and $(\Re, w)$ have to be found. In Appendix B these relations have been derived and appear to be:

$$\Re_{aper} = \frac{\left[\Delta y + \frac{2\pi}{k\zeta_1^2}\right]^2 + \frac{4}{k^2\zeta_0^4}}{\left[\Delta y + \frac{2\pi}{k\zeta_1^2}\right]} \tag{3.24}$$

and

$$w_{aper} = \frac{1}{k\zeta_0} \sqrt{4 + k^2\zeta_0^4 \left[\Delta y + \frac{2\pi}{k\zeta_1^2}\right]^2} \tag{3.25}$$

where the index *aper* stands for aperture. The distance between the center of the dielectric lens and the aperture plane is denoted by Δy.

3.2 Elliptical lens

First it is started by considering an elliptical lens with a rotationally symmetric shape. For an ellipsoid with its long axis parallel to the y-axis, it is possible to write the following defining equation:

$$\frac{x^2+z^2}{a^2} + \frac{y^2}{b^2} = 1 \tag{3.26}$$

with a and b being half the length of the short and long axis, respectively. From optics it is known that, for a given index of refraction n_d, all rays coming from the more distant focus of the ellipse will leave the lens parallel to the y-axis, if the eccentricity of the elliptical lens satisfies the following equation [16]:

$$\text{eccentricity} = \frac{\sqrt{b^2-a^2}}{b} = \frac{c}{b} = \frac{1}{n_d} \tag{3.27}$$

Therefore, the feed antenna must be located at the second focus ($y=-c$) of the dielectric ellipse, where the focal distance is determined by $c=\sqrt{b^2-a^2}$. The index of refraction determines for the shape of the elliptical lens. Any antenna, placed at the focus of the elliptical lens, will result in a far-field pattern with a main beam that is diffraction limited by the aperture of the dielectric lens. This means that the main beam cannot be smaller than the main beam of a uniformly illuminated aperture. In Figure 3.3 the elliptical lens with its planar feed antenna is shown. In this figure the same coordinate system as in Figure 3.1 is used.

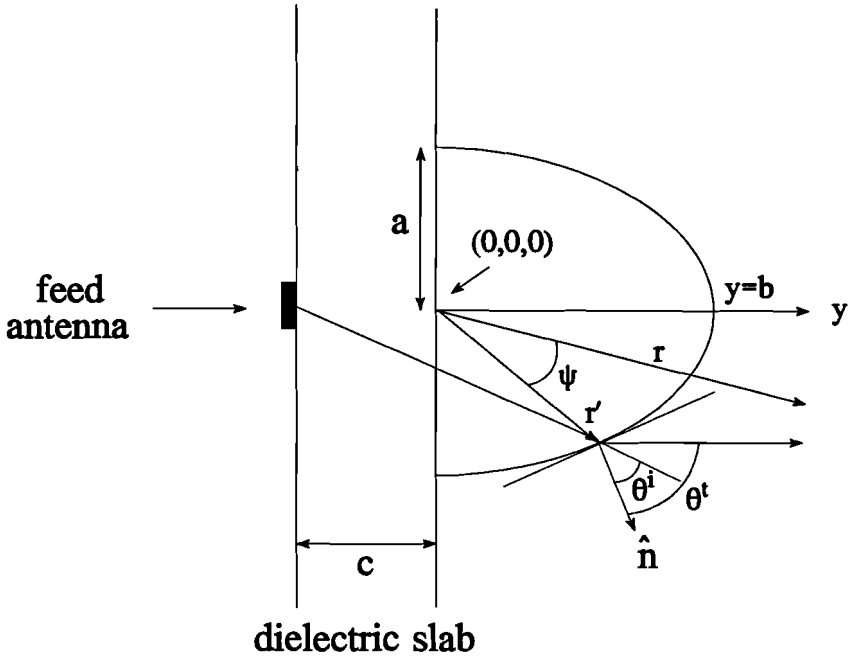

Figure 3.3 : Planar antenna on a dielectric slab in combination with an elliptical lens.

3.2.1 Calculated far-field radiation patterns

3.2.1.1 Double-slot antenna

In this section the power patterns of a double-slot antenna in combination with an elliptical lens are presented. The diameter of the lenses is 15.0 mm and for the dielectric materials silicon, quartz and HDP are used. To compare the elliptical lenses on top of the appropriate slab thickness (c) with each other, the shapes of the three lenses are shown in Figure 3.4. In this figure can be seen that the lens with the smallest dielectric constant (HDP) has the largest dimensions. The feed antenna is always placed in the origin of the coordinate system. Figures 3.5 and 3.8 hold for a silicon lens, while in Figures 3.6 and 3.9 the planar antenna is placed on top of a quartz dielectric lens. Finally, the power patterns of the double-slot antenna on a HDP lens are shown in Figures 3.7 and 3.10. The frequencies that are used in these calculations are 246 and 500 GHz. In these examples the slot antennas always have a length of $0.28\lambda_0$, while the spacing is $0.16\lambda_0$ (silicon), $0.20\lambda_0$ (quartz) or $0.25\lambda_0$ (HDP), respectively.

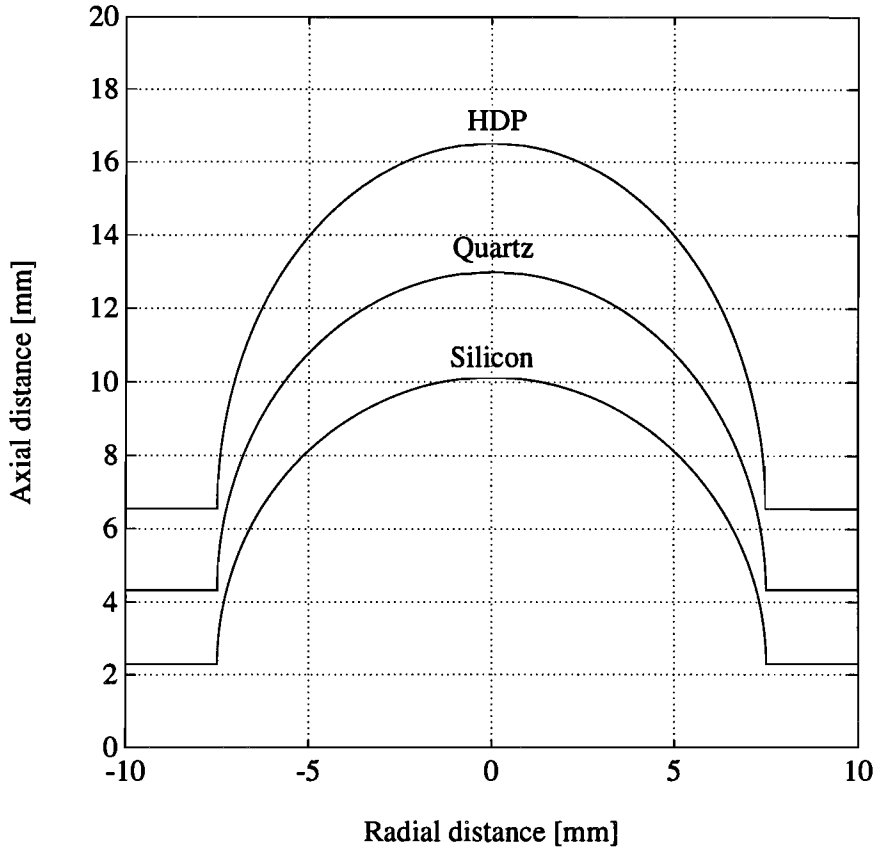

Figure 3.4 : The shape of three different elliptical lenses.

From Figures 3.5 to 3.10 it can be seen that the integrated lens antenna with the silicon dielectric has the highest directivity (29.4 dBi). This is partially explained by the relatively small spillover losses, which are a function of the maximum angle (ζ_m) of a propagating ray illuminating the lens surface, assuming that the radiation patterns in the different dielectrics are more or less the same. This maximum angle is increasing with the dielectric constant and therefore with the silicon material less power is radiated beside the lens surface.

In the choice of the length $2l$ and the distance Δd between the slot antennas, the correspondence between the E- and H-plane patterns was an important criterion. It appears that in the three designs the E- and H-plane power patterns are almost identically, with the remark that the sidelobes in the E-plane are the highest. For example the first sidelobes in the E-plane at 246 GHz are 17.5, 15.0 and 15.0 dB down in case of silicon, quartz and HDP respectively. Also the sidelobe envelope is decreasing faster with the silicon dielectric than with the other two, for both frequencies used.

The nearly identical E- and H-plane patterns result in the same 10-dB beamwidth in both planes. In silicon the 10-dB beamwidth has a value of around 8.8° at 246 GHz, while this is 8.0° and 7.9° for quartz and HDP, respectively.

Because the power patterns have been calculated for two different frequencies, i.e. 246 and 500 GHz, it is possible to check the frequency dependence of some antenna properties. From Equation (3.16) one can see that the directivity is proportional to f^2. This implies that the directivity improvement should be $20\log_{10}(500/246) = 6.16$ dB when the frequency is increased from 246 to 500 GHz. Figures 3.5 to 3.10 show that this is indeed true for all three dielectrics. At 500 GHz the 10-dB beamwidths are 4.3, 4.0 and 3.8° for silicon, quartz and HDP respectively. All these values are approximately one half (246/500) of the beamwidths at 246 GHz. Thus, according to the calculations of the far-field radiation patterns, the beamwidths are nearly proportional to $1/f$.

For clarity the important antenna properties and efficiencies have been put into Table 3.1. In this table the beamwidth is the 10-dB beamwidth and this is an average value of both the E- and H-plane beamwidths. The relative first sidelobe levels are all computed in the E-plane, because in this plane the levels are worse (i.e. higher) than the sidelobe levels in the H-plane.

***Table 3.1** : Properties and efficiencies of an elliptical lens antenna illuminated by a double-slot feed, with slot elements having a length of $0.28\lambda_0$.*

f (GHz)	Δd (λ_d)	ε_r	Directivity (dBi)	Beamwidth (°)	Rel. first side-lobe level (dB)	η_{beam} (%)
246	0.16	11.7	29.4	8.8	-17.5	90.7
246	0.20	4.00	28.6	8.0	-15.0	75.8
246	0.25	2.31	26.8	7.9	-15.0	71.5
500	0.16	11.7	35.6	4.3	-17.8	89.3
500	0.20	4.00	34.8	4.0	-15.0	74.9
500	0.25	2.31	33.0	3.8	-14.7	69.9

The directivities are determined by Equations (2.27) and (2.28). In Table 3.1 also the beam efficiencies of the different antenna configurations are given. These beam efficiencies have been calculated from the power patterns by taking the power in the main beam to a level of -20 dB relative to the peak in the power patterns. It is good to note that this efficiency does not include the spillover and reflection losses of the integrated lens antenna, because the power in the main beam is only divided by the power radiated through the surface of the lens. From Table 3.1 it is seen that the beam efficiency is the best for the silicon lens antenna, and that this efficiency is decreasing with the relative dielectric constant. A possible explanation for this fact might be the combination of the actual beamwidth and the directivity of the different dielectric lens antennas. The higher the directivity and the larger the beamwidth, the better the beam efficiency is. Also from Table 3.1 one can see that for silicon both the directivity and the beamwidth have the greatest values, compared with the other two dielectrics. Furthermore, an increase of the frequency results in a smaller beam efficiency in all three cases.

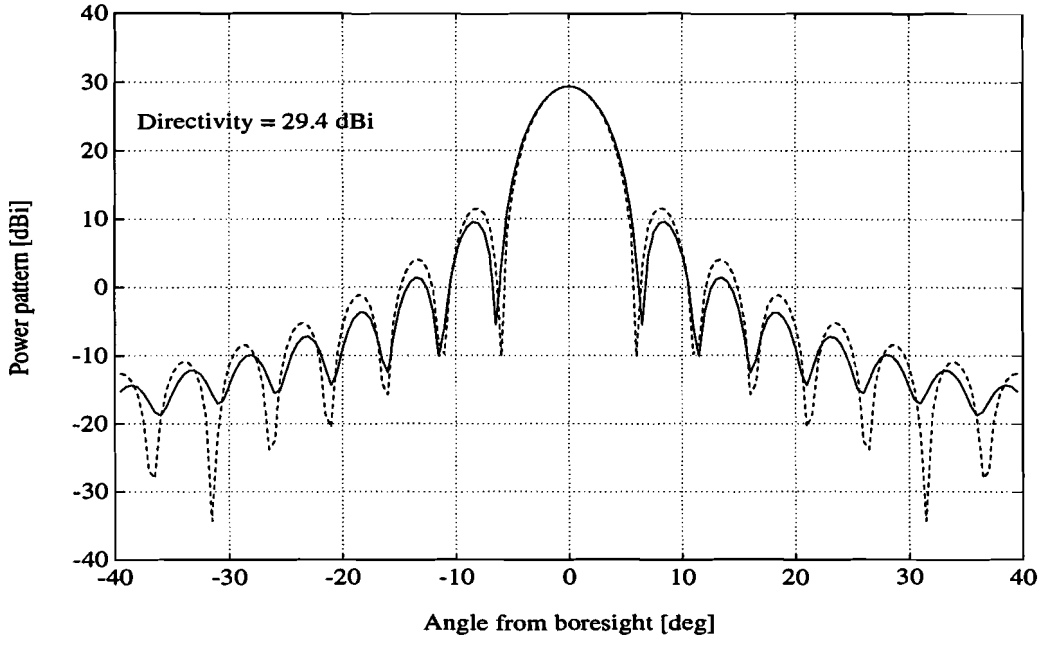

***Figure 3.5** : Power patterns of a double-slot antenna in combination with an elliptical silicon lens at a frequency of 246 GHz (solid line: H-plane, and dashed line: E-plane).*

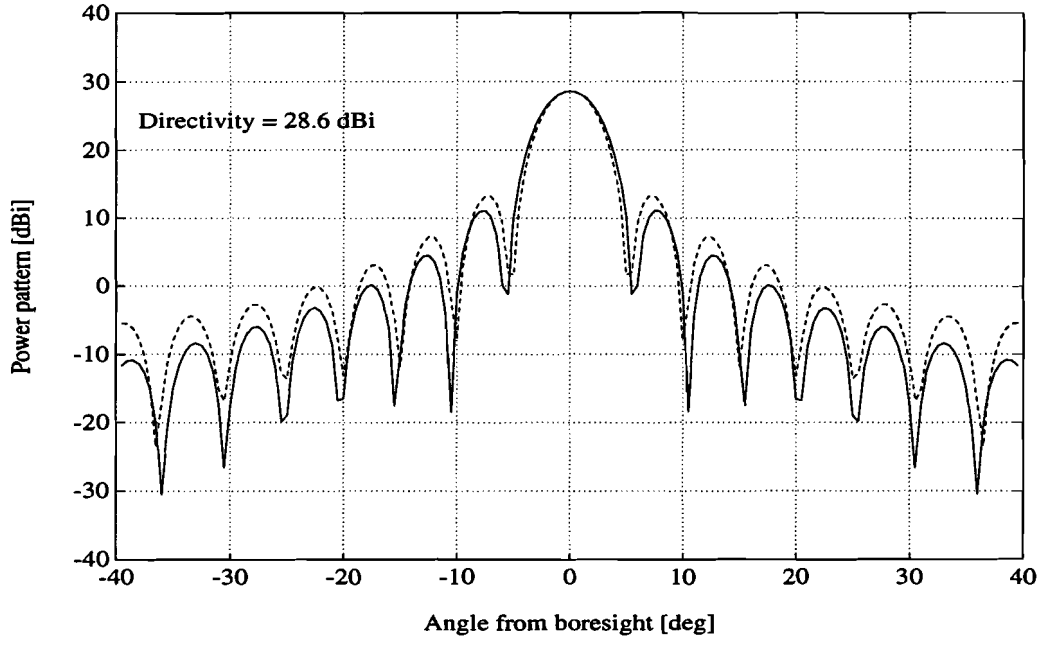

***Figure 3.6** : Power patterns of a double-slot antenna in combination with an elliptical quartz lens at a frequency of 246 GHz (solid line: H-plane, and dashed line: E-plane).*

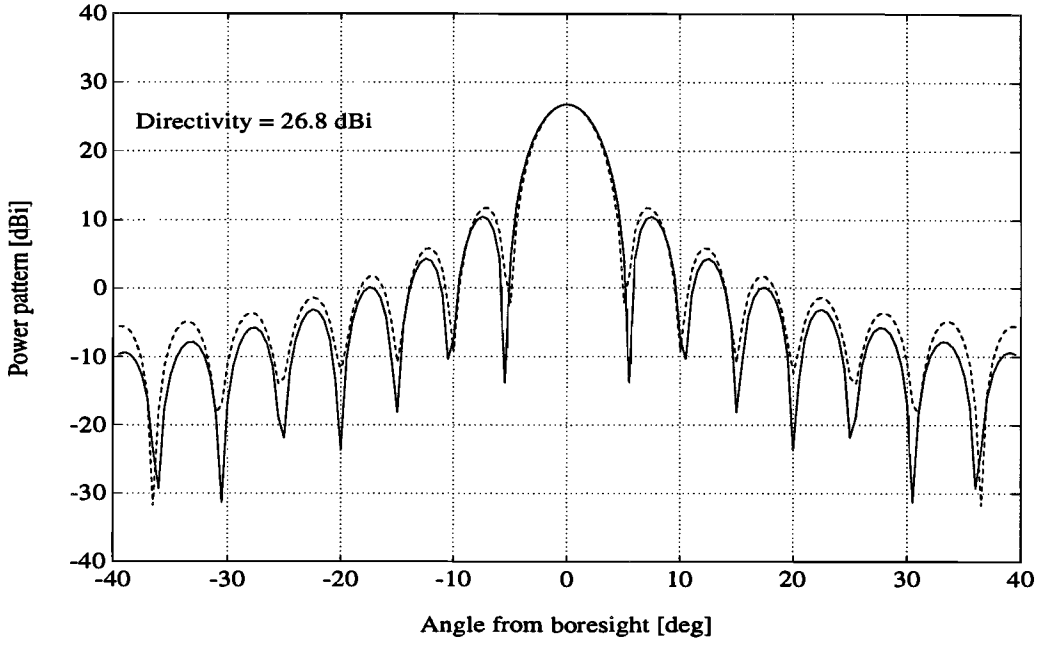

***Figure 3.7** : Power patterns of a double-slot antenna in combination with an elliptical HDP lens at a frequency of 246 GHz (solid line: H-plane, and dashed line: E-plane).*

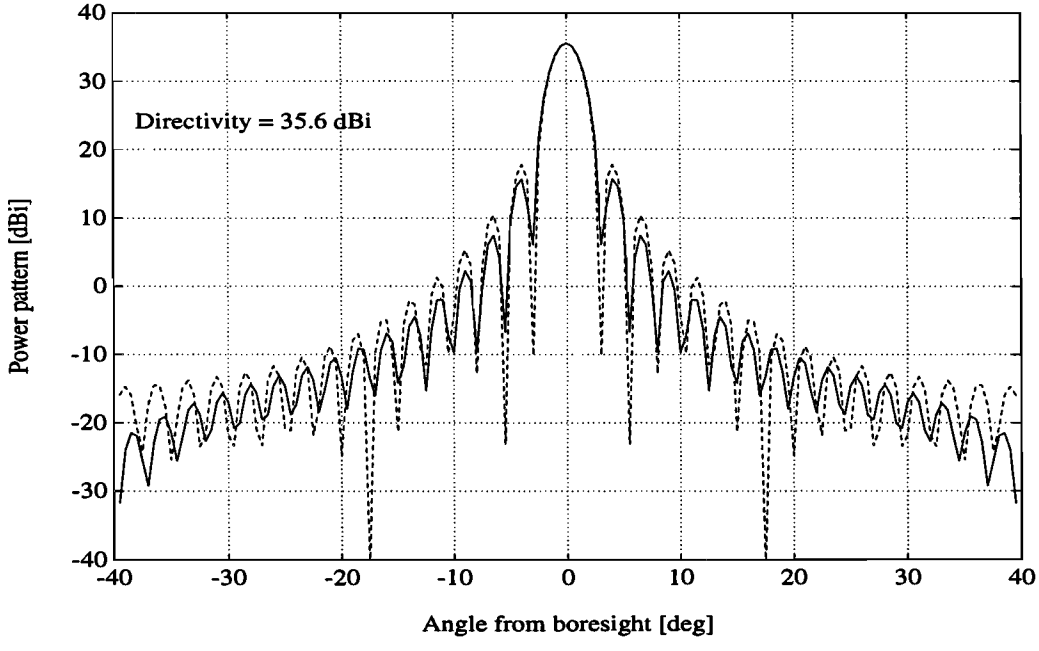

***Figure 3.8** : Power patterns of a double-slot antenna in combination with an elliptical silicon lens at a frequency of 500 GHz (solid line: H-plane, and dashed line: E-plane).*

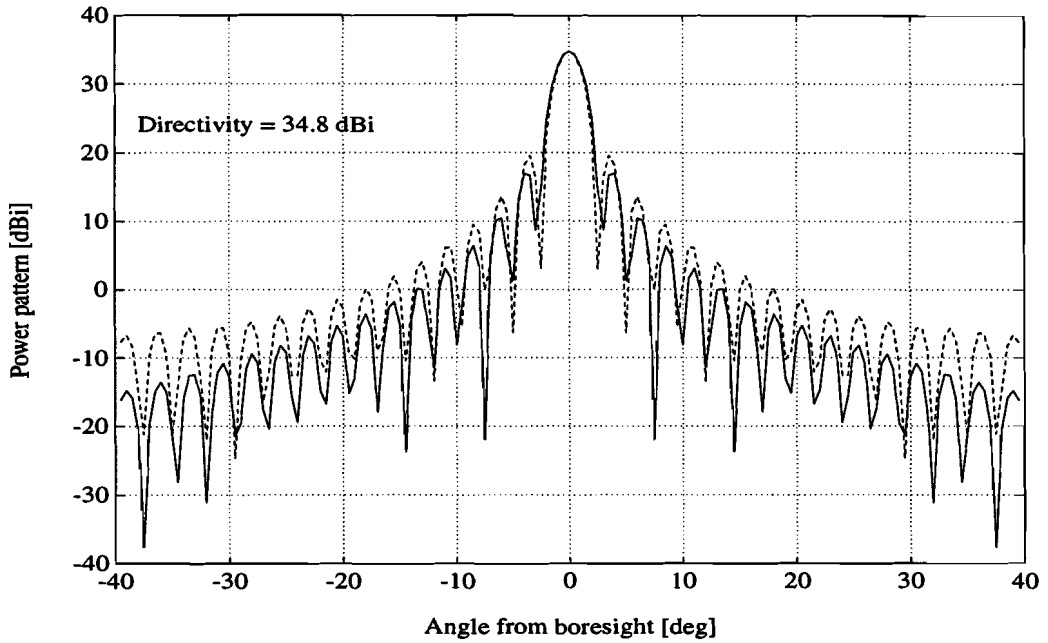

Figure 3.9 *: Power patterns of a double-slot antenna in combination with an elliptical quartz lens at a frequency of 500 GHz (solid line: H-plane, and dashed line: E-plane).*

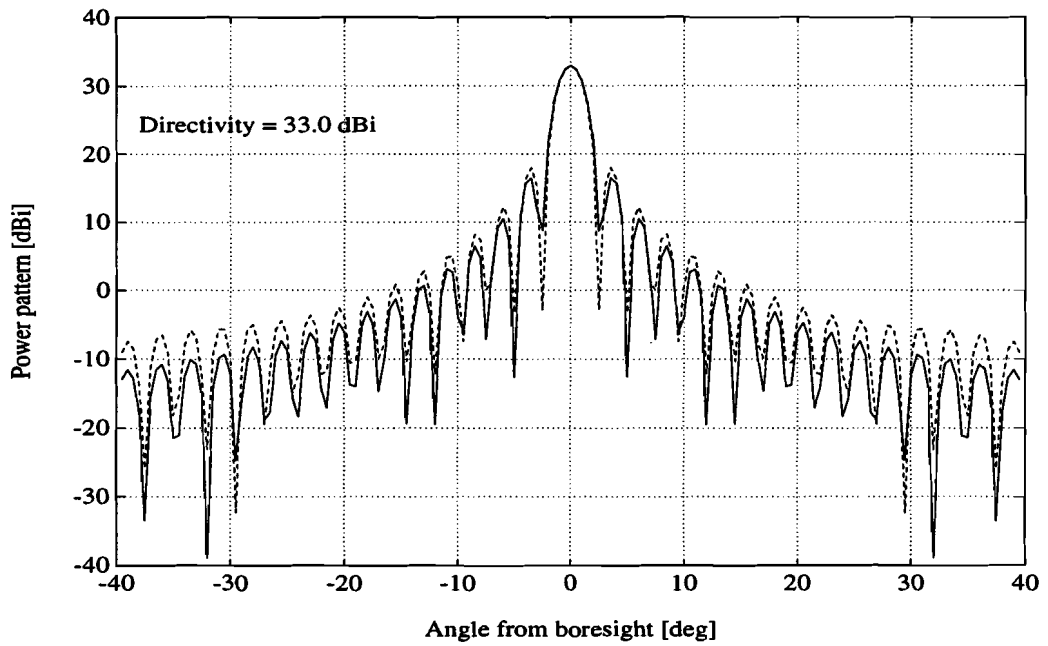

Figure 3.10 *: Power patterns of a double-slot antenna in combination with an elliptical HDP lens at a frequency of 500 GHz (solid line: H-plane, and dashed line: E-plane).*

3.2.1.2 Double-dipole antenna with a backing reflector

The next planar antenna to be used as a feed for the dielectric lens with a diameter of 15.0 mm, is the double-dipole. To prevent that any power will be lost directly to the air, a reflector has been placed behind the feed antenna at a distance of $0.25\lambda_d$, where λ_d is the wavelength in the dielectric. As already explained, this kind of backing reflector cannot be used in case of a double-slot antenna, because the double-slot antenna itself already consists of a metal ground plane. Between the reflector and the double-dipole antenna the same dielectric material as the lens is used. Power patterns have been calculated only for the frequency 246 GHz. The first three plots are made for a double-dipole antenna with two half-wave dipole elements separated by $0.4\lambda_d$. Figures 3.14 to 3.16, on the other hand, show the radiation patterns of a double-dipole antenna with two $0.80\lambda_d$ long dipole elements, which are placed parallel to each other at a distance of $0.49\lambda_d$. As dielectric materials silicon, quartz and HDP are used again.

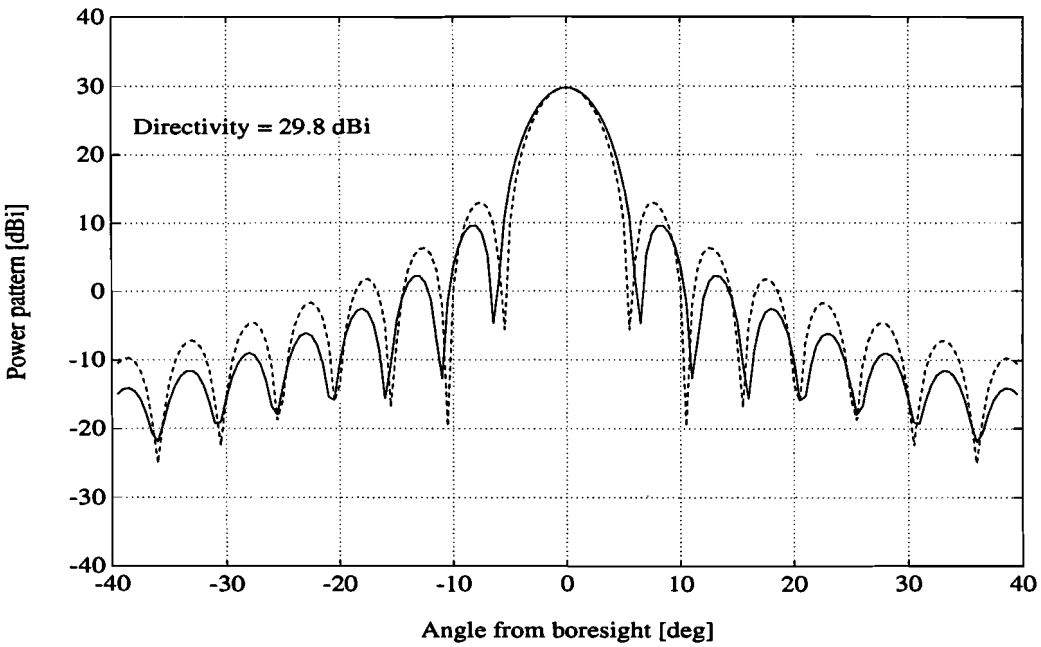

Figure 3.11 : Power patterns of a double-dipole antenna with a backing reflector on an elliptical silicon lens at a frequency of 246 GHz (solid line: H-plane, and dashed line: E-plane).

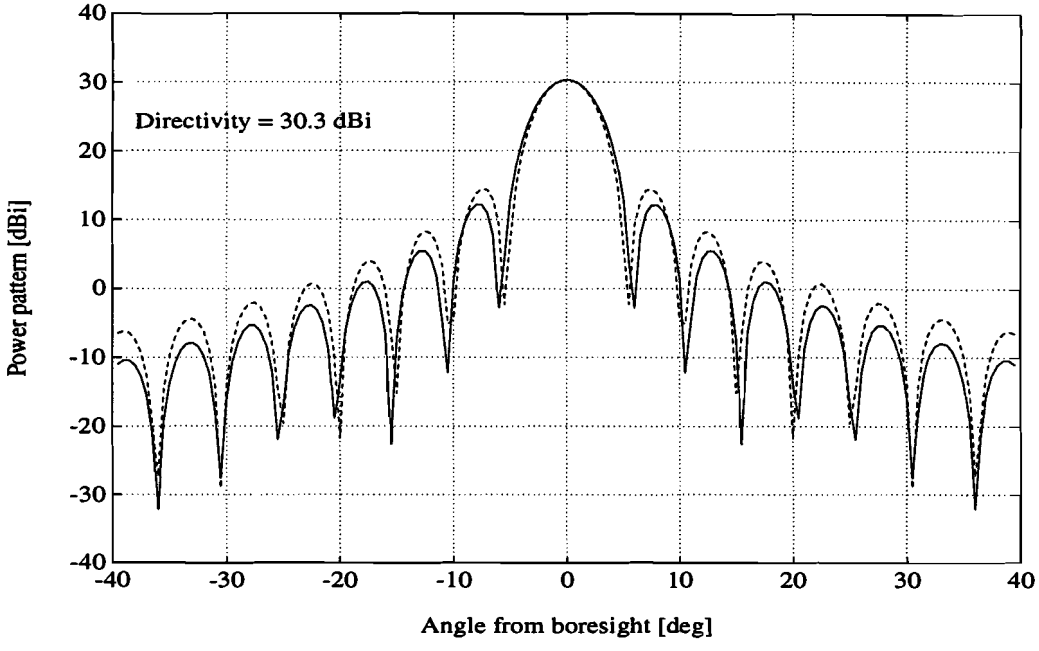

***Figure 3.12** : Power patterns of a double-dipole antenna with a backing reflector on an elliptical quartz lens at a frequency of 246 GHz (solid line: H-plane, and dashed line: E-plane).*

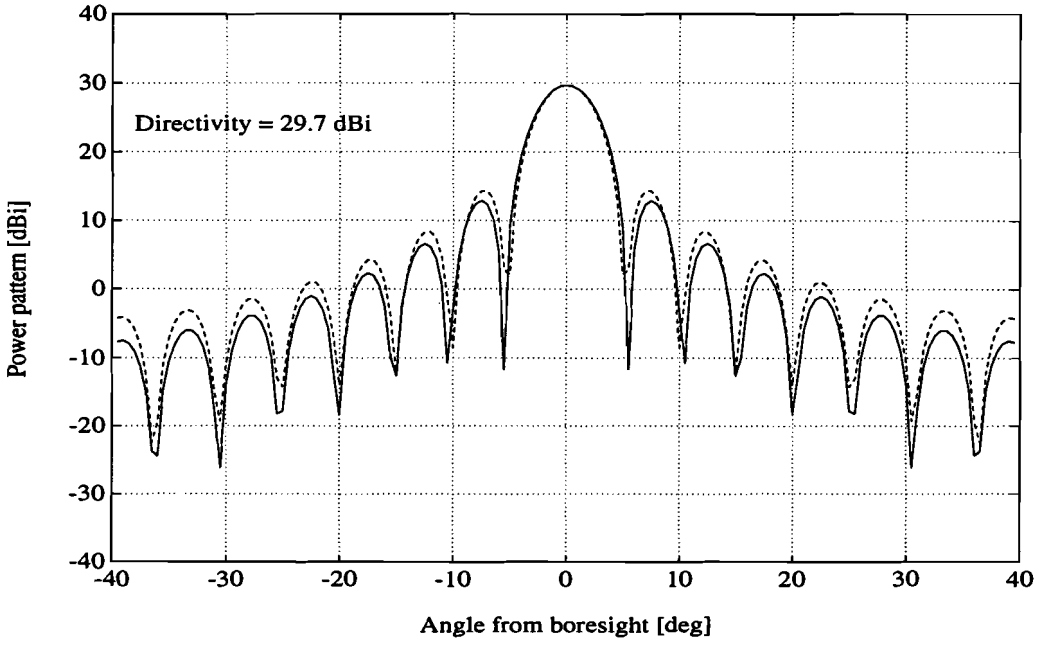

***Figure 3.13** : Power patterns of a double-dipole antenna with a backing reflector on an elliptical HDP lens at a frequency of 246 GHz (solid line: H-plane, and dashed line: E-plane).*

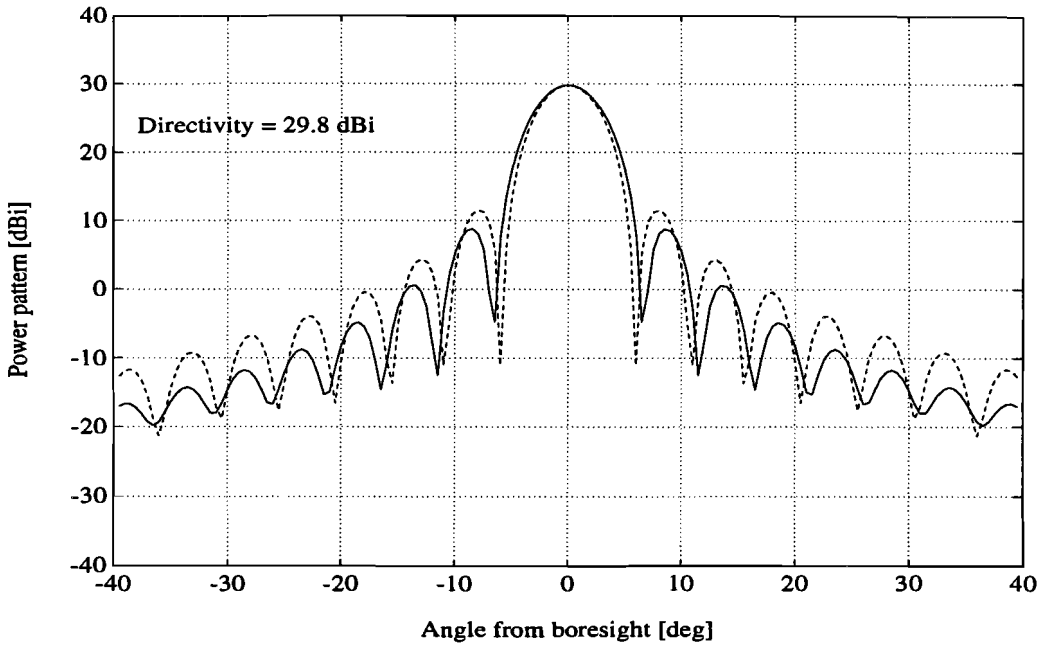

Figure 3.14 : Power patterns of a double-dipole antenna with a backing reflector on an elliptical silicon lens at a frequency of 246 GHz (solid line: H-plane, and dashed line: E-plane).

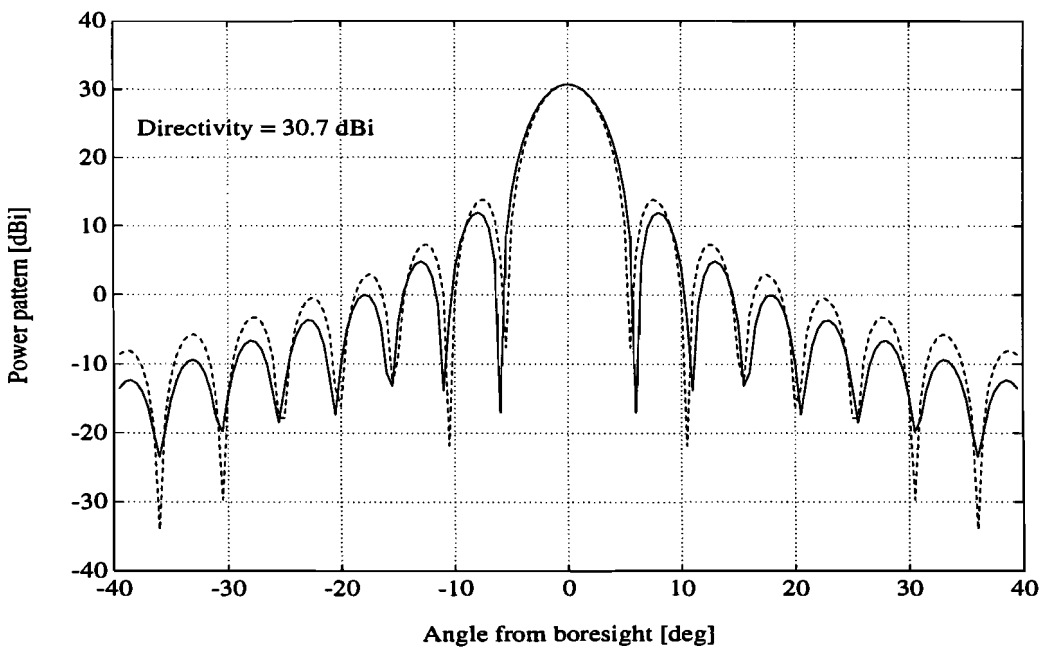

Figure 3.15 : Power patterns of a double-dipole antenna with a backing reflector on an elliptical quartz lens at a frequency of 246 GHz (solid line: H-plane, and dashed line: E-plane).

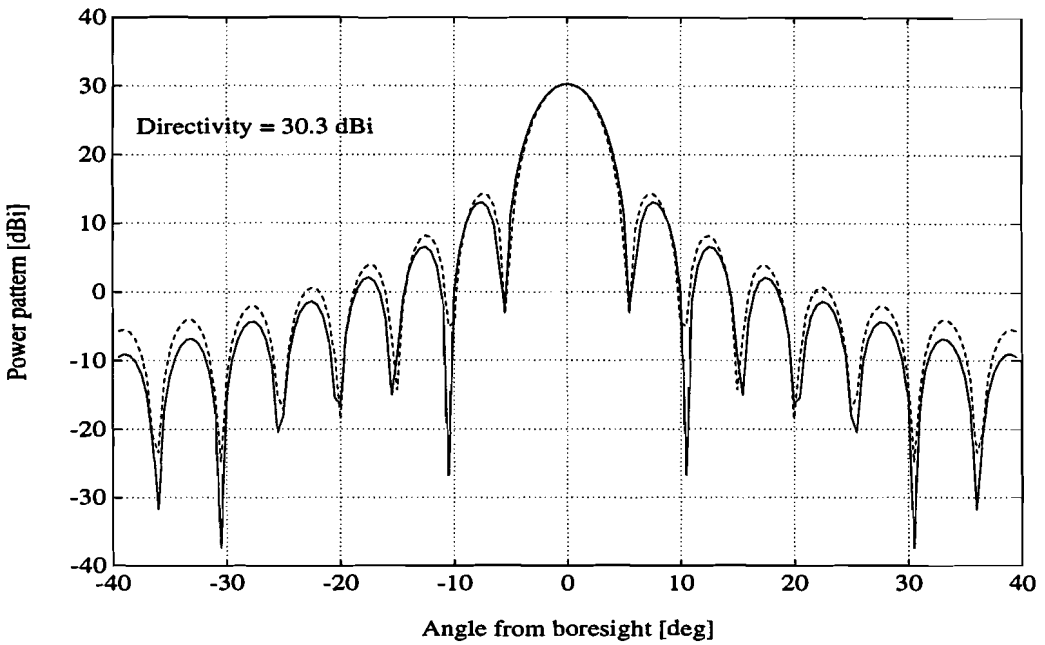

***Figure 3.16** : Power patterns of a double-dipole antenna with a backing reflector on an elliptical HDP lens at a frequency of 246 GHz (solid line: H-plane, and dashed line: E-plane).*

The directivity of the integrated lens antenna with the double-dipole feed is around 30 dBi at 246 GHz. With the quartz dielectric this directivity is the highest (30.3 and 30.7 dBi) for both double-dipole feeds. Compared to the double-slot feeds, the directivity is increased by approximately 1.5 dB. Of course this is for a great part due to the backing reflector, which causes the spillover losses to decrease. With the backing reflector no power is radiated directly into the air, and only little radiation will pass the dielectric lens. It is also seen that the double-dipole feed with the longest dipole elements has the highest directivity in all three examples.

For convenience some important antenna properties and efficiencies are summarized in Table 3.2. From this table one can see that the beamwidth of the double-dipole with the half-wave dipole elements is smaller than the beamwidth of the second double-dipole feed, for every dielectric material. These 10-dB beamwidths are comparable with the beamwidths of the double-slot fed integrated lens antennas. In contradiction to the beamwidth, the relative first sidelobe levels are higher or worse with the half-wave dipole elements than with the double-dipole feed with a length of 0.80 λ_d. Furthermore, the silicon dielectric lens antenna seems to be the best solution for a low relative first sidelobe level and a good sidelobe envelope.

***Table 3.2** : Properties and efficiencies of an elliptical lens antenna illuminated by a double-dipole feed with a backing reflector at a frequency of 246 GHz.*

$2l$ (λ_d)	Δd (λ_d)	ε_r	Directivity (dBi)	Beamwidth (°)	Rel. first side-lobe level (dB)	η_{beam} (%)
0.50	0.40	11.7	29.8	8.5	-17.0	87.8
0.50	0.40	4.00	30.3	8.3	-15.5	80.7
0.50	0.40	2.31	29.7	7.9	-15.0	74.7
0.80	0.49	11.7	29.8	8.8	-18.0	92.2
0.80	0.49	4.00	30.7	8.5	-17.0	85.6
0.80	0.49	2.31	30.3	8.0	-16.2	78.9

As with the double-slot feed the beam efficiency of the elliptical lens antenna, illuminated by the double-dipole feed, is the highest for silicon (87.8 and 92.2%). HDP appears to have the worst beam efficiency of the three dielectrics considered. Furthermore, the beam efficiency is better for the second double-dipole feed (with the longer dipole elements) than for the first one and changes close to 5% for all three dielectrics. When comparing these beam efficiencies to the ones obtained from the double-slot fed lens antennas, it is seen that the double-dipole with a backing reflector gives more or less the best results. This is certainly true for the largest double-dipole feed.

3.2.2 Calculated aperture field and antenna efficiencies

In this section the antenna efficiencies will be determined, which make up the directivity of the lens antenna. Some of these efficiencies, aperture and polarization efficiency, can only be computed when the field values are known in a planar aperture. Another restriction is that this planar aperture should also be an equiphase plane for the radiated field of the antenna. When using an elliptical lens which satisfies Equation (3.27) both criteria are fulfilled.

3.2.2.1 Double-slot antenna

As an illustration, the aperture field has been computed for a silicon dielectric lens, which is illuminated by a double-slot feed antenna with the following dimensions: $2l=0.28\lambda_0$ and $\Delta d=0.16\lambda_0$. For the lens a diameter of 13.7 mm is chosen. The field strength distribution is shown in Figure 3.17 with the remark that these values are normalized to the field strength in the origin of the xz-coordinate system.

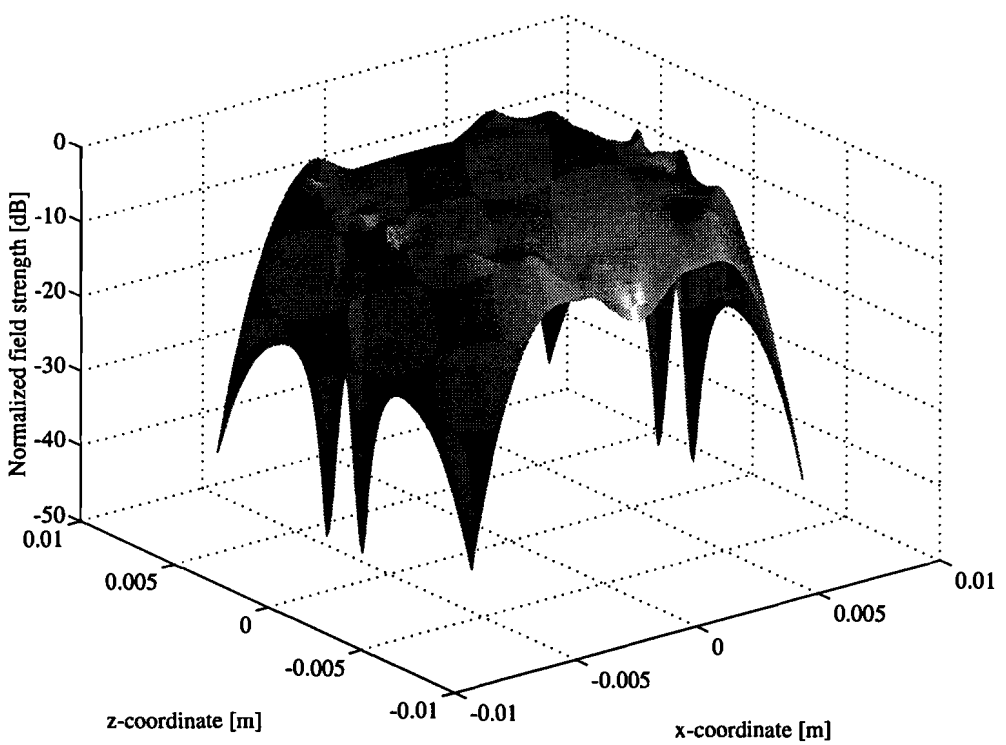

Figure 3.17 : The normalized aperture field distribution of an elliptical silicon lens, illuminated by a double-slot feed at a frequency of 246 GHz.

If Figure 3.17 is examined more precisely one can see that the field is not rotationally symmetric but the aperture field distribution can be divided into four equal parts. This is of course very logical, since the feed antenna is an array of two elements. The elliptical lens ensures that the phase will be uniform in the aperture, but how uniform is the field strength? In Figure 3.17 can be seen that the amplitude distribution is quite flat in the middle of the aperture, and drops very quickly to zero when the x- or z-coordinate approaches the radius of the lens.

Next the antenna efficiencies have been calculated for the antenna designs used in Section 3.2.1.1 and are shown in Table 3.3. The applied elliptical lens has a diameter of 15.0 mm.

***Table 3.3** : Properties and efficiencies of an elliptical lens antenna illuminated by a double-slot feed, with slot elements having a length of $0.28\lambda_0$.*

f (GHz)	Δd (λ_0)	ε_r	Directivity (dBi)	η_a (%)	η_s (%)	η_p (%)	η_{tr} (%)	η_{gaus} (%)	w_0 (mm)
246	0.16	11.7	29.41	94.9	91.1	96.0	70.4	87.8	6.00
246	0.20	4.00	28.64	97.8	65.1	97.8	78.7	73.1	6.75
246	0.25	2.31	26.81	96.0	44.0	99.0	76.8	69.2	7.13
500	0.16	11.7	35.57	94.9	91.1	96.0	70.4	87.8	6.00
500	0.20	4.00	34.80	97.8	65.1	97.8	78.7	73.1	6.75
500	0.25	2.31	32.97	96.0	44.0	99.0	76.8	69.2	7.13

From Table 3.3 one can see that the directivities, which are calculated with Equation (3.16), do agree very well with the directivities from Table 3.1. The aperture and polarization efficiency is for all three designs better than approximately 95%. The difference in directivity is thus explained by the rapidly decreasing spillover efficiency, if one goes from a high to a low dielectric constant. It is obvious that the HDP dielectric design is not very useful in this way as a feed for a parabolic reflector. Of course the spillover efficiency can be increased, if the radiation pattern of the double-slot is narrowed. But the question that remains is, whether this will affect the other efficiencies.

The Gaussian beam efficiency is the highest for silicon (87.8%) and this corresponds with a low aperture efficiency. Apparantely a high aperture efficiency excludes a high Gaussian beam efficiency, which is logical because of the difference in aperture distributions. An 100% aperture efficiency corresponds to a flat amplitude distribution, while the Gaussicity is optimal for a Gaussian amplitude distribution. The efficiencies at 500 GHz are exactly the same as the efficiencies at 246 GHz, because all the (antenna) efficiencies depend on the radiation pattern in the dielectric and this pattern is not changed by an increase of the frequency.

From a communication point of view it is interesting to know what the bandwidth of the investigated antenna is. Of course the maximum achievable bandwidth is limited by two factors. The first one is the input impedance of the integrated lens antenna and secondly the directivity will also limit the bandwidth. These two factors can be combined when the gain of the antenna is considered. In this report the input impedance is not calculated and only the role of the directivity can be examined. Therefore, the directivity of a double-slot elliptical lens antenna has been computed from 400 to 700 GHz. The length of and the distance between the slot elements are $2l=0.28\lambda_0$ and $\Delta d=0.16\lambda_0$ respectively, with an operating frequency of 500 GHz. In Figure 3.18 the directivity of the considered antenna is plotted. From Equation (3.16) one can see that the directivity is a product of two factors. The first part is the maximum directivity of an aperture type antenna with diameter D, while the second term consist of the product of the different antenna efficiencies. These two factors are also shown in Figure 3.18. For readability the efficiency curve is raised by 40 dB.

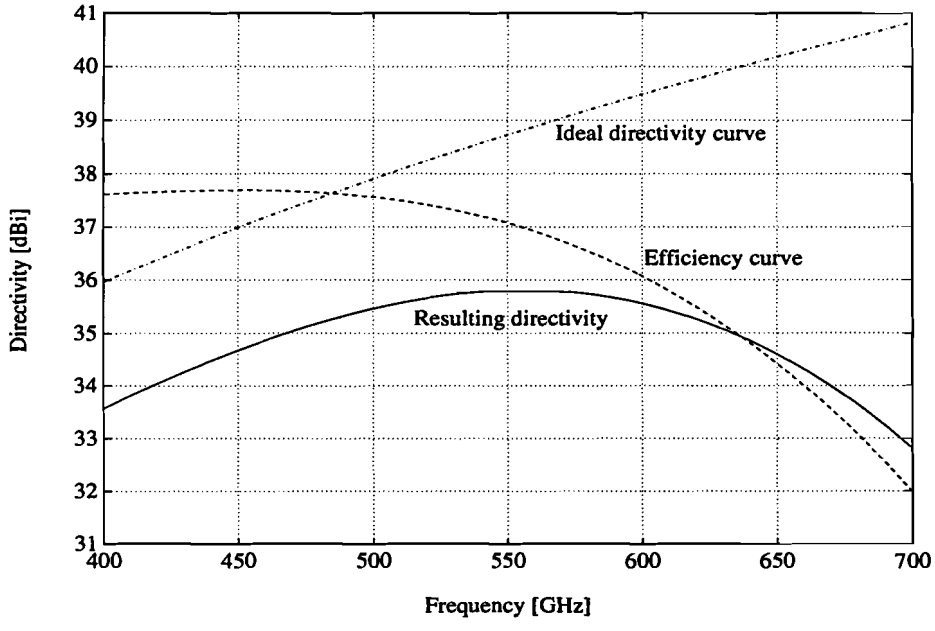

***Figure 3.18** : The directivity curve of a 15 mm silicon lens antenna illuminated by a double-slot feed.*

It is directly seen from Figure 3.18 that the optimum operating frequency, for a high directivity, is around 550 GHz for the chosen antenna design. The 3-dB bandwidth appears to be more than 300/550 = 55% when the operating center frequency is 550 GHz. A short remark is needed here, because this bandwidth is only determined by the directivity of the integrated lens antenna and the reflection losses at the terminals of the feed antenna are not included.

3.2.2.2 Double-dipole antenna with a backing reflector

The advantage of using a twin array with a backing reflector instead of a single twin array, is that an extra parameter can be varied to optimize the pattern in terms of rotation symmetry. To demonstrate this, the aperture-field distribution of a double-dipole antenna with a backing reflector is computed and shown in Figure 3.19. The diameter of the silicon lens is 13.7 mm, while for the feed the following dimensions are chosen: $2l = 0.80\lambda_d$ and $\Delta d = 0.49\lambda_d$. A quarter-wave length behind the feed the metallic reflector is placed.

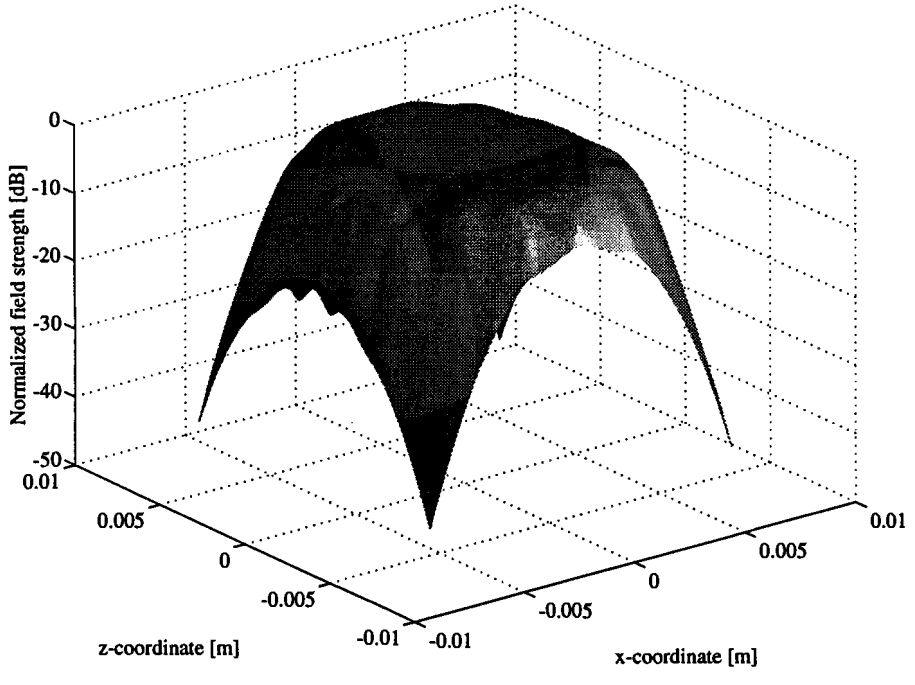

Figure 3.19 : The normalized aperture-field distribution of an elliptical silicon lens, illuminated by a double-dipole feed with a backing reflector at a frequency of 246 GHz.

As expected the field is more rotationally symmetric now than with the double-slot array as shown in Figure 3.17. In the middle of the aperture the field-strength distribution is nearly

flat and near the end it drops quickly to zero. A more uniform amplitude distribution in the aperture should result in a higher aperture efficiency, which can be checked by looking at the following computed and tabulated antenna efficiencies.

***Table 3.4** : Properties and efficiencies of an elliptical lens antenna illuminated by a double-dipole feed with a backing reflector at a frequency of 246 GHz.*

$2l$ (λ_d)	Δd (λ_d)	ε_r	Directivity (dBi)	η_a (%)	η_s (%)	η_p (%)	η_{tr} (%)	η_{gaus} (%)	w_0 (mm)
0.50	0.40	11.7	29.80	97.7	99.9	100.0	65.6	85.6	6.38
0.50	0.40	4.00	30.33	99.3	94.2	100.0	77.3	78.5	6.75
0.50	0.40	2.31	29.66	97.7	82.0	100.0	77.4	72.3	6.75
0.80	0.49	11.7	29.80	93.8	100.0	100.0	67.5	90.2	6.00
0.80	0.49	4.00	30.69	99.1	98.2	100.0	80.7	83.5	6.56
0.80	0.49	2.31	30.34	99.2	90.3	100.0	80.9	76.8	6.75

The antenna efficiencies appear to be much better with the double-dipole antenna with backing reflector than with the double-slot. Especially the spillover efficiencies of the HDP and quartz dielectric lens antenna have been improved a lot. This is due to the reflector and the narrower beam of the double-dipole feed. Another interesting thing is the 100% polarization efficiency. Thus, the field in the aperture is (nearly) uniformly polarized in the z-direction, for the six designs. A comparison between the transmission efficiencies shows that the dielectric with the highest refractive index has the highest reflection losses. These reflection losses vary from 19% for HDP to 35% for silicon.

Naturally, also a high Gaussicity is wanted. From Table 3.4 can be concluded that only the antenna designs with the silicon material have acceptable Gaussian beam efficiencies (85.6 and 90.2%). However, compared to the corrugated horn antenna, these Gaussicities are still very low. The minimum waist values in the aperture are also given in Table 3.4. These values may be useful when the integrated lens antenna is used in a quasi-optical antenna system with for example lenses and reflectors.

3.3 Extended hemispherical lens

In Section 3.2 an elliptical lens attached to a dielectric slab was considered. However, it appears that in practice it is not so easy to manufacture a lens with an elliptical shape. Therefore, several have looked for alternative configurations that have nearly identical properties as the elliptical lens antenna system. One of these alternatives is the extended hemispherical lens, which is shown in Figure 3.20. Other ways to approximate the elliptical shape can be found in Ref. [17].

The radius and the corresponding extension length of the extended hemispherical lens are determined by considering the ellipsoid from Equation (3.26). The analysis can be done in two dimensions, because both the elliptical and the extended hemispherical lens are rotationally symmetric. Further, it is assumed that the lenses lie in the *xy*-plane.

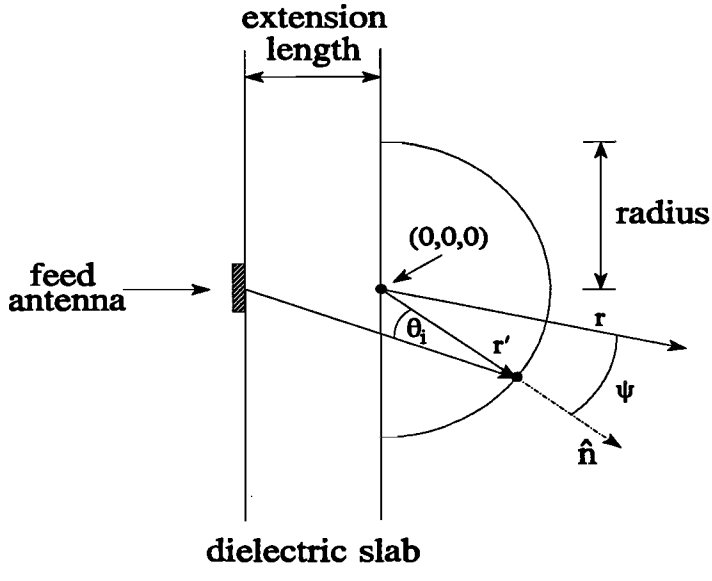

***Figure 3.20** : Planar antenna on a dielectric slab in combination with a hemispherical dielectric lens.*

From Equation (3.27) can be derived that:

$$b = \frac{a}{\sqrt{1-\frac{1}{n_d^2}}} \tag{3.28}$$

and

$$c = \frac{b}{n_d} \tag{3.29}$$

Now a hemisphere of unit radius is defined by $x^2+y^2=1$ and only positive values of y are chosen. In order to superimpose the extended hemisphere and the ellipse, the distance from the tip of the hemisphere to the antenna must be the same as the distance from the tip of the ellipse to its more distant focus, where the antenna is placed. This leads to the following equation:

$$L_{ex}+1 = b+c \tag{3.30}$$

To find the best fitted extended hemisphere for a given index of refraction, the parameter b is varied until the geometrical match, determined by the least square error, is the closest to an ellipse. For a silicon dielectric lens the fitted ellipse values are $a=1.03$ and $b=1.07691$ [1], yielding an extension length of 2608 μm with a 13.7 mm diameter lens. For a 15.0 mm diameter lens the extension length becomes 2855 μm. It appears that the higher the dielectric constant the better the geometrical approximation is. In Figure 3.21 both the elliptical and the extended hemispherical lens are shown for the best fitted solution.

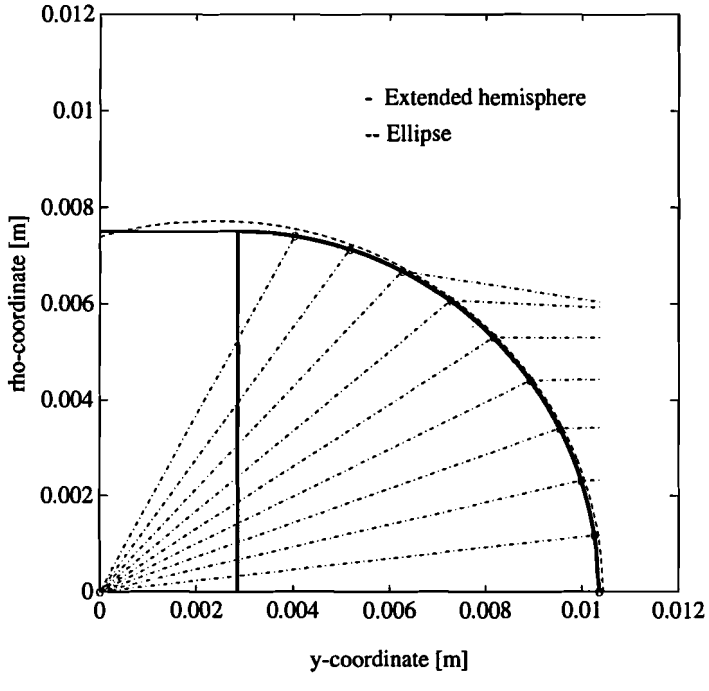

Figure 3.21 : The best fitted silicon ellipse for an extended (L_{ex} = 2855 μm) hemispherical lens with a diameter of 15.0 mm.

The approximation of the ellipse by an extended hemisphere seems very good, especially for small angles. In Figure 3.21 also a few rays from the feed to the aperture plane are drawn. It appears that the rays are refracted, by the extended hemisphere, almost parallel to the *y*-axis and that for the rays with a large angle of propagation the reflection is 100%.

3.3.1 Comparison with Filipovic's results

Previous calculations of the radiation patterns of a planar antenna on top of an extended hemispherical lens have already been done by Filipovic et al. [1]. In his paper, he calculated the normalized power patterns of a double-slot antenna on top of a silicon lens. To be absolutely sure that our results are the same as his results, a comparison is made for a double-slot antenna with a length and a spacing of $0.28\lambda_0$ and $0.16\lambda_0$, respectively. The frequency that is used is 246 GHz for all examples. In Figures 3.22 to 3.25 the results of these comparisons are shown for different extension lengths, varying between 1800 and 3000 μm, while the diameter of the hemispherical silicon lens had a value of 13.7 mm. In the following plots only the H-plane radiation patterns are shown and the results obtained by our program are denoted by EUT (Eindhoven University of Technology).

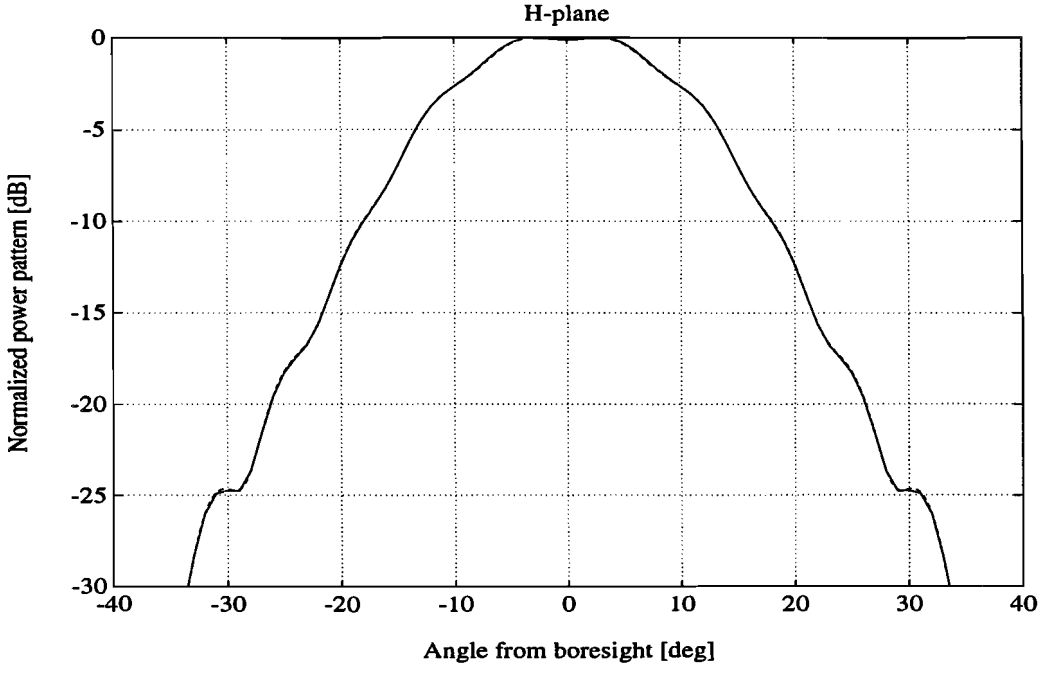

***Figure 3.22** : Normalized power patterns of a double-slot antenna on an extended (L_{ex} = 1800 μm) hemispherical silicon lens (solid line: EUT, and dashed line: Filipovic).*

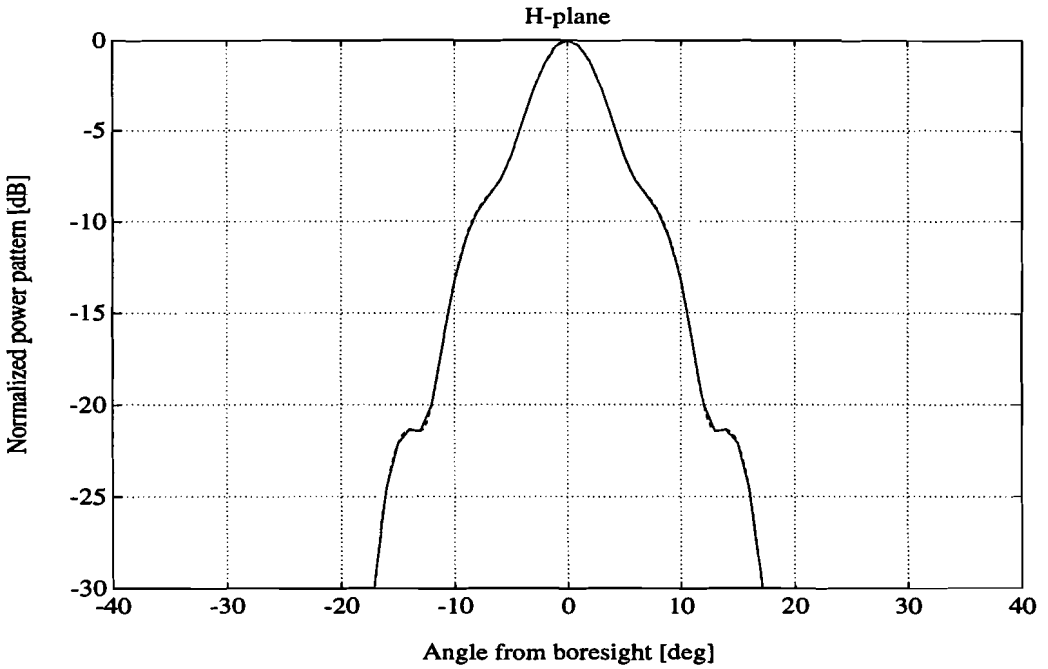

***Figure 3.23** : Normalized power patterns of a double-slot antenna on an extended (L_{ex} = 2200 μm) hemispherical silicon lens (solid line: EUT, and dashed line: Filipovic).*

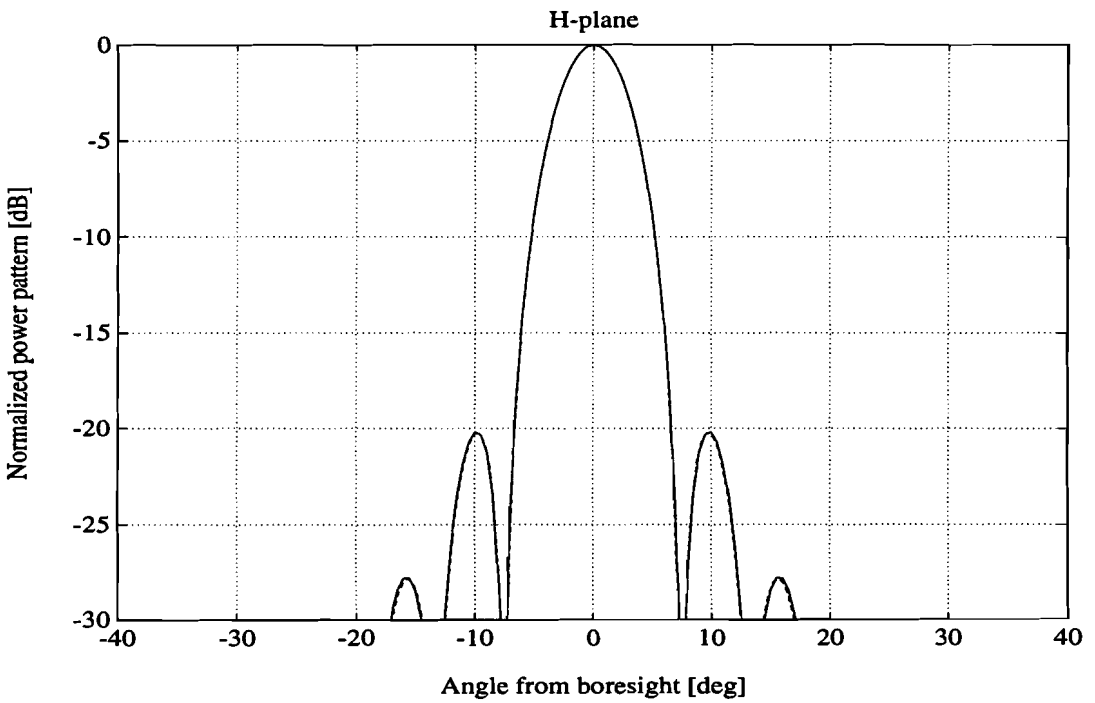

***Figure 3.24** : Normalized power patterns of a double-slot antenna on an extended (L_{ex} = 2600 μm) hemispherical silicon lens (solid line: EUT, and dashed line: Filipovic).*

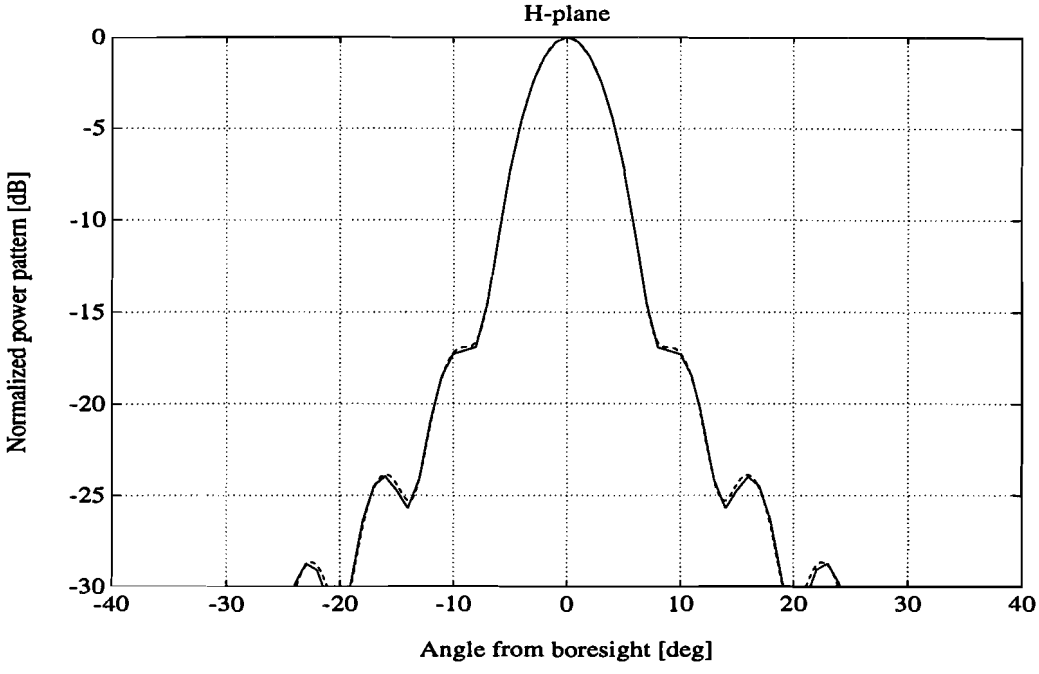

***Figure 3.25** : Normalized power patterns of a double-slot antenna on an extended (L_{ex} = 3000 μm) hemispherical silicon lens (solid line: EUT, and dashed line: Filipovic).*

The comparisons show a very good agreement for all four extension lengths. In the first three figures it is even hard to see that there are two different curves plotted. The E-plane field and the far-field phase are not shown here, despite the fact that they have been compared. Again the correspondence was very good between our computed values and Filipovic's [1].

3.3.2 Calculated far-field radiation patterns

In Section 3.2.1 radiation patterns have been calculated for the double-slot and double-dipole feed antenna with a 15.0 mm diameter elliptical silicon, quartz and HDP lens. The results of these computations varied with the different configurations, as could be expected. To machine an elliptical lens is in practice more expensive than for example a hemisphere. This is the reason that in this report also the extended hemispherical lens is analyzed. Questions that can arise are: What is the directivity degradation when an ellipse is replaced by a hemisphere, in case of the best fitted solution? What is the influence of the extension length on the directivity, Gaussian beam efficiency or radiation pattern? Some of these questions will be answered in this section. First of all the radiation pattern and the corresponding directivity are treated. Of course it is possible to consider every configuration as with the ellipse, but it is chosen to analyze only the double-slot feed on a silicon dielectric. The operating frequency is set to 246 GHz. In order to compare the directivity of the elliptical and the hemispherical

lens, the same physical aperture is required and so the diameter of the hemisphere is 15.0 mm. In Section 3.3 it is determined that the best fitted hemisphere for a silicon dielectric needs an extension length of 2855 μm for the 15.0 mm elliptical lens. For four different extension lengths, being 2000, 2400, 2800 and 3200 μm, the power patterns have been computed for both the E- and H-plane. In Figures 3.26 to 3.29 these patterns are shown for angles between -40 and 40° from boresight.

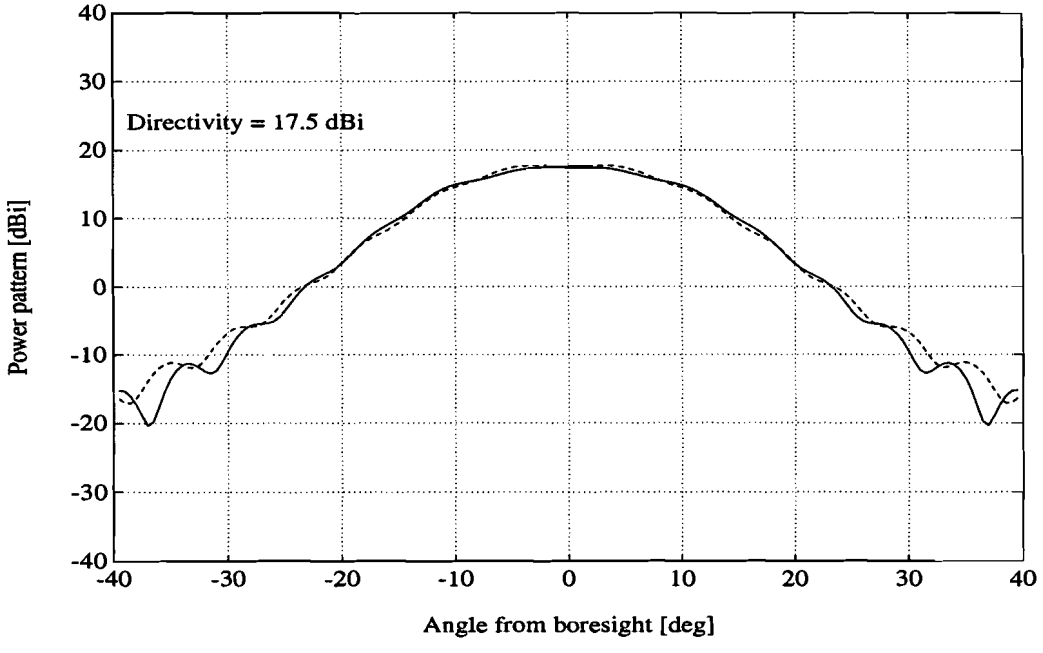

***Figure 3.26** : Power patterns of a double-slot antenna in combination with a hemispherical silicon lens (L_{ex} = 2000 μm) at a frequency of 246 GHz (solid line: H-plane, and dashed line: E-plane).*

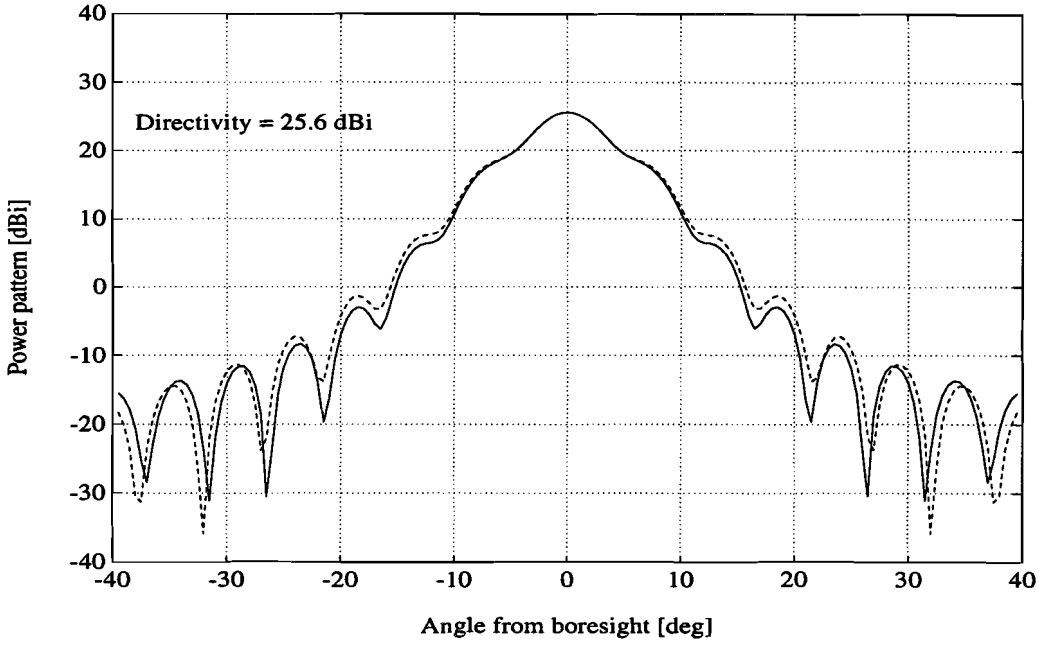

Figure 3.27 : Power patterns of a double-slot antenna in combination with a hemispherical silicon lens (L_{ex} = 2400 μm) at a frequency of 246 GHz (solid line: H-plane, and dashed line: E-plane).

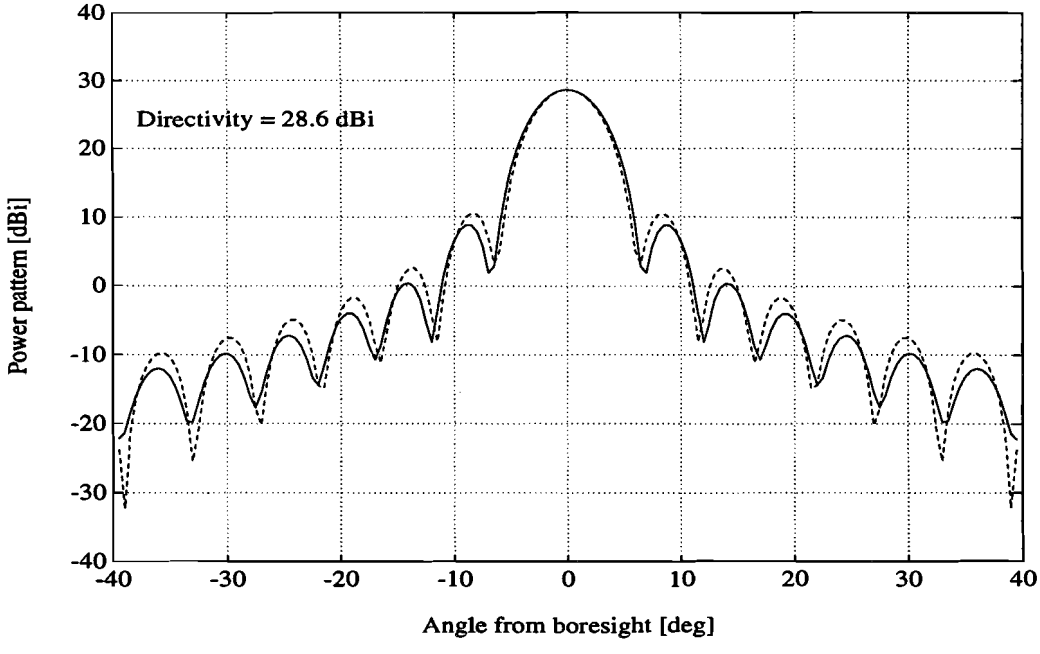

Figure 3.28 : Power patterns of a double-slot antenna in combination with a hemispherical silicon lens (L_{ex} = 2800 μm) at a frequency of 246 GHz (solid line: H-plane, and dashed line: E-plane).

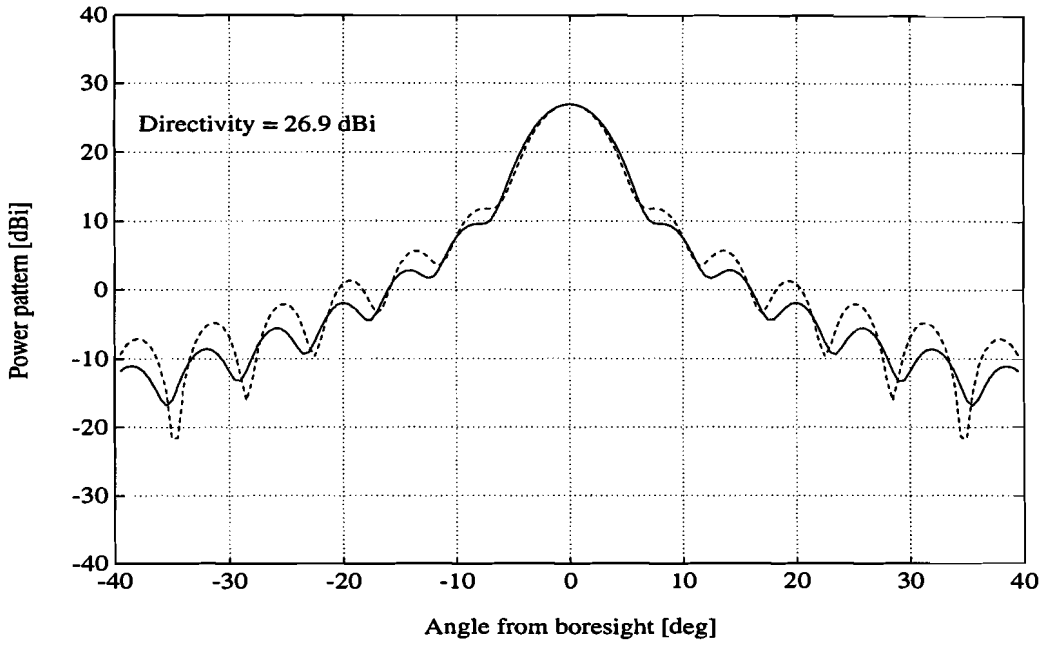

***Figure 3.29** : Power patterns of a double-slot antenna in combination with a hemispherical silicon lens (L_{ex} = 3200 μm) at a frequency of 246 GHz (solid line: H-plane, and dashed line: E-plane).*

First of all it can be said that the patterns in the E- and H-planes do agree quite well, especially for small angles from boresight. The directivity appears to be strongly dependent on the extension length. At 2000 μm it is 17.5 dBi, while for an extension length of 2800 μm an improvement of more than 10 dB is obtained. The maximum directivity will probably occur around L_{ex}=2855 μm, because then the extended hemispherical lens has the closest geometrical match to an elliptical lens. Small extension lengths seem to result in very broad beams and as a consequence the directivity is low. Naturally, the broad beams should have a large 10-dB beamwidth. These beamwidths are 34.7, 16.8, 9.5 and 10.5° for the considered extension lengths in order of occurrence in the Figures 3.26 to 3.29 and indeed the higher directivities correspond with the lower beamwidths.

It is difficult to determine the relative first sidelobes of the broader beam antennas, because the end of the main beams can not easily be indicated. This also implies that the beam efficiency is not a very good measurable quantity. However, the coupling to the fundamental Gaussian beam can very well be determined. As already explained, the Gaussicity is computed using a normalized inner product between the radiation patterns of the lens antenna and the first-order Gaussian beam, as seen in Equation (3.22). From the values (ζ_0,ζ_1), which are found at the maximum Gaussicity, the radius of curvature and the beam waist in the aperture plane of the antenna can be obtained. The Gaussian beam efficiency has been calculated for

the above-mentioned configuration with extension lengths varying from 1200 to 3400 μm. At the same time the radius of curvature, the beam radius and the directivity are determined. These results are shown in Table 3.5. The radius of curvature and the waist in the aperture plane are computed with Equations (3.24) and (3.25).

***Table 3.5** : Gaussian beam efficiencies and directivities for an extended hemispherical silicon lens antenna, illuminated by a double-slot feed at a frequency of 246 GHz.*

L_{ex} (μm)	Directivity (dBi)	η_{gaus} (%)	ζ_0 (rad)	ζ_1 (rad)	$\Re_{aper}$ (mm)	w_{aper} (mm)
1200	12.9	96.19	0.4186	0.4290	+6.49	1.00
1400	14.5	95.50	0.4099	0.3853	-8.18	1.00
1600	14.9	95.63	0.3854	0.3466	-5.23	1.44
1800	16.9	94.83	0.3338	0.3097	-7.54	2.09
2000	17.5	93.89	0.2638	0.2661	-12.92	2.96
2200	19.6	93.54	0.2070	0.2293	-20.92	3.75
2400	25.6	92.59	0.1434	0.1897	-39.89	4.65
2600	28.1	90.20	0.0970	0.1914	-91.97	4.72
2800	28.6	87.90	0.0683	0.8446	+1201.6	5.70
3000	28.1	85.98	0.0713	0.2510	+243.96	5.77
3200	26.9	84.81	0.0908	0.1886	+94.84	5.72
3400	25.5	86.56	0.1100	0.1719	+69.87	6.42

The Gaussian beam efficiency is very high for small extension lengths and decreases from 96.2% at 1200 μm to 84.8% at 3200 μm. This decrease in Gaussicity at the larger extension lengths can be interpreted as the result of the formation of out-of-phase sidelobes, whose level progressively increases as the extension length is increased. Around the synthesized elliptical position (2855 μm) the Gaussian beam efficiency is nearly the same as for the elliptical lens (87.8%). An optimum for the forward directivity can be found between 2600 and 3000 μm.

In Table 3.5 one can see that the radius of curvature in the aperture plane first has a positive value, meaning that the minimum waist plane is located on the left side of the aperture, and then changes sign. The radius of curvature approaches infinite around 2800 μm, which is very near the synthesized elliptical position. In the aperture plane of the extended hemispherical silicon lens, the waist increases up to an extension length of 3000 μm, when the double-slot feed is moved in axial direction away from the tip of the lens.

It is very interesting to compare the radiation patterns of the elliptical lens and the synthesized elliptical lens. Therefore, the radiation patterns in the H-plane are computed for a silicon dielectric at a frequency of 246 GHz and these are shown in Figure 3.30. The comparison does not only include the patterns, but also the beam efficiency, Gaussicity and beamwidth will be considered.

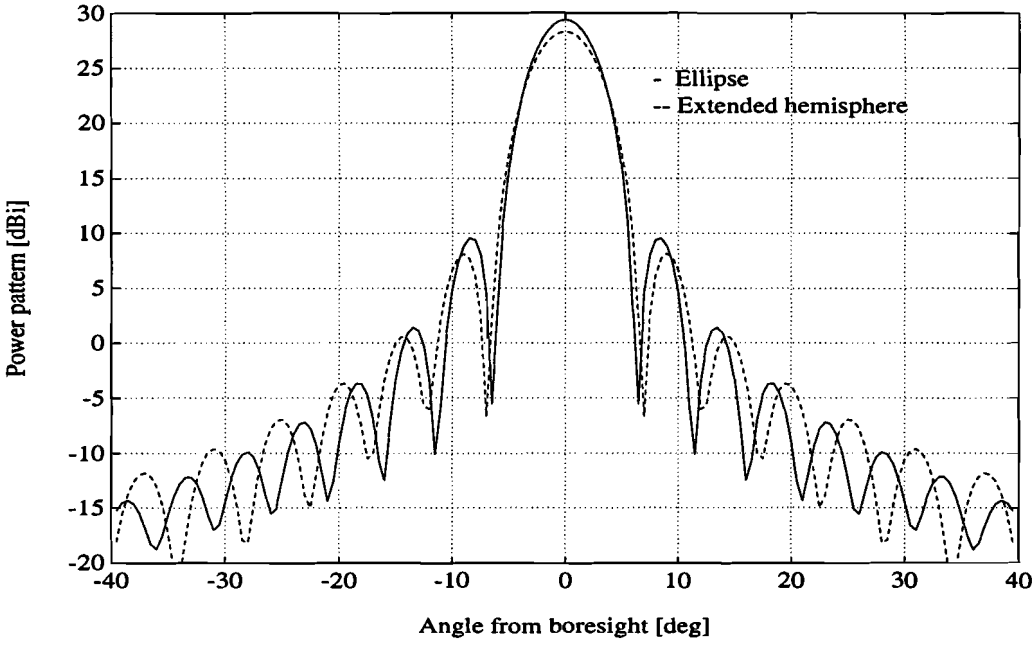

***Figure 3.30** : Power patterns of an elliptical and an extended (L_{ex} = 2855 μm) hemispherical silicon lens in the H-plane at a frequency of 246 GHz.*

At first glance, the result of the comparison seems rather good, though it can be seen that there are some differences between the two. The degradation in directivity is 1.1 dB when the extended hemisphere is used instead of the ellipse. For the 10-dB beamwidths values of 8.8 and 9.6° are found in case of the elliptical and the extended hemispherical lens, respectively. The latter however, has a better relative first sidelobe level (-20.2 dB) compared to -19.7 dB for the ellipse, but for the other sidelobes it is the other way around. These sidelobe levels

are computed in the H-plane and not in the E-plane. Further, the true elliptical lens has a better beam efficiency than the extended hemispherical lens and this beam efficiency is 88.4% for the extended hemisphere, which is 2.3% worse than for the elliptical lens.

The coupling to the fundamental Gaussian beam is better for the ellipse. A Gaussian beam efficiency of 87.8% is calculated for the ellipse and 87.6% for the extended hemisphere, but of course this is not a very hugh difference. The corresponding radius of curvature is approximately 730 mm for the hemisphere, which is very close to the value of infinite for the ellipse speaking in terms of the radius of the lens. It is found that the beam radius in the aperture plane is 6.00 mm for the elliptical and 5.68 mm for the synthesized elliptical silicon lens. Finally, it can be concluded that the real elliptical lens in general has better antenna properties than the synthesized one, but the latter may be applied as a good alternative solution.

3.3.3 Calculated antenna efficiencies

In contradiction to the elliptical lens, it is not possible to compute the directivity with the use of the antenna efficiencies in case of the extended hemispherical lens. When this type of lens is used, only the spillover and the transmission efficiency are determined, because these two efficiency calculations do not require a unique planar aperture, as is the case for the aperture and polarization efficiency. The directivity is first calculated from the far-field radiation pattern and then the combined aperture efficiency is found simply by dividing this forward directivity by η_s, η_{tr} and the factor $(\pi D/\lambda_0)^2$. In this section the directivity of the extended hemispherical lens will be calculated as a function of the extension length, for a silicon dielectric. Together with this directivity, the antenna efficiencies shall be computed. Beforehand it can be predicted that the spillover efficiency will decrease when the antenna is placed further away from the center of the lens in axial direction. This is obvious, because the further the antenna is shifted from the center, the more power is radiated beside the dielectric lens. The maximum angle of a ray illuminating the lens is a decreasing function of the extension length. To demonstrate this and at the same time determine the directivity curve, a plot has been made for a silicon lens, illuminated by the same double-slot feed as in the previous section. In Figure 3.31 this plot, with the directivity, the spillover-, the combined aperture- and the transmission-efficiency curve, is shown. Also this time the double-slot is fed by a 246 GHz signal.

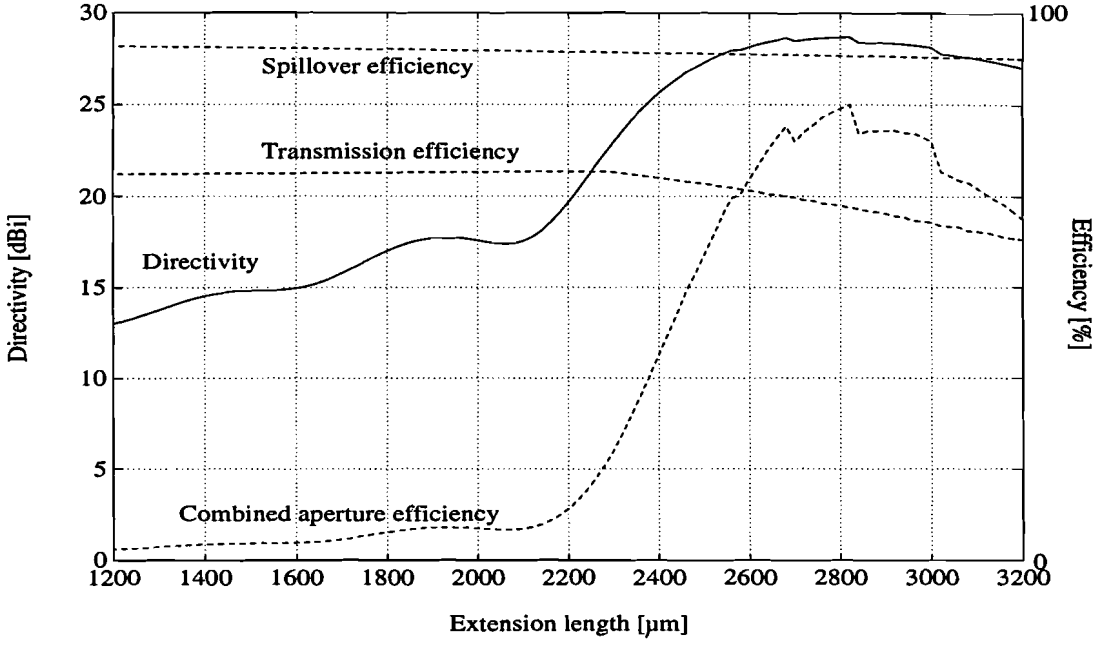

***Figure 3.31** : The directivity and the antenna efficiencies of an extended hemispherical silicon lens, illuminated by a double-slot feed at 246 GHz, as a function of the extension length.*

It is seen that the spillover losses do indeed increase as the extension length is increased. These losses are 6.1% at 1200 μm and change to 8.3% at 3200 μm, but it is a slowly varying function. The reflection losses, on the other hand, tend to decrease in the first part of the plot up to an extension length of 2200 μm, but when the extension length is further increased the transmission efficiency also gets worse and ends at 58.7% at 3200 μm. Both the spillover and the transmission efficiency do not seem to have a great influence on the directivity, because of their rather flat curves. The combined aperture efficiency however, does change significantly compared to the other two. At small extension lengths (up to 2100 μm) the combined aperture efficiency is very low (< 6%) but with a further increase it approaches the value of 84% at the maximum directivity. This maximum directivity occurs at an extension length of approximately 2820 μm, which is near the synthesized elliptical position (2855 μm). It is clear that the directivity curve has almost the same shape as the curve of the combined aperture efficiency, with their maxima at the same extension length. At 2820 μm the maximum directivity is 28.7 dBi, which is still 0.7 dB lower than the directivity of the true elliptical silicon lens at 246 GHz.

4. Comparison between theory and measurements

A true elliptical HDP lens, illuminated by a double-dipole feed with a backing reflector, is used by Skalare [8] during his measurements at frequencies from 7 to 14 GHz. The double-dipole feed was designed for an operating frequency of 10 GHz and had a length of $0.5\lambda_d$ and a spacing of $0.4\lambda_d$ between the dipole elements. The backing reflector is put a quarter wavelength behind the feed. For the diameter of the elliptical lens he chose a value of 11.0 cm. The dipole elements together with the IF and DC bias line where put on a thin Kapton film, which was placed between the HDP lens and the quarter wavelength slab with the backing reflector. In Figure 4.1 the Kapton film with the dipole elements is shown.

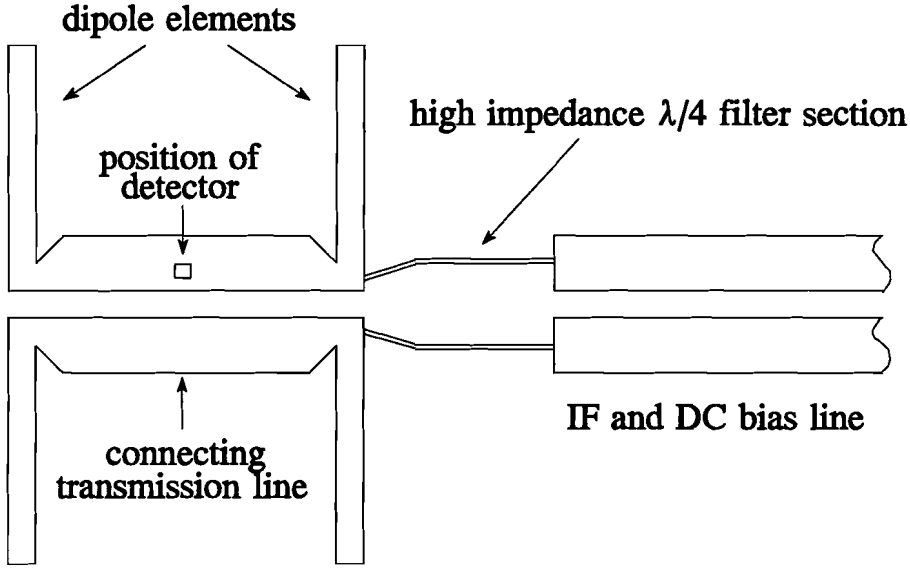

Figure 4.1 : Double-dipole antenna structure on a Kapton film.

In Ref. [8] Skalare presented measurements of the co- and cross-polarized patterns in the E-, D- and H-plane at eight different frequencies. The measured co- and cross-polarized patterns are defined according to the third definition of Ludwig [18].

For the co- and cross-polarized unit vectors the following defining equations can be written:

$$\hat{e}_{co} = \cos\delta\hat{e}_{\zeta} - \sin\delta\hat{e}_{\delta} \tag{4.1}$$

$$\hat{e}_{cr} = \sin\delta\hat{e}_{\zeta} + \cos\delta\hat{e}_{\delta} \tag{4.2}$$

Next the co-polarized patterns are compared for all three planes. Two frequencies, 9 and 11 GHz, are chosen as an example and the other six (7,8,10,12,13 and 14 GHz) can be found in Appendix C of this report. The co-polarized patterns are shown in Figures 4.2 to 4.7, where the solid line represents the measured data from Skalare and the dashed line is the pattern computed at the EUT. It appeared that the maxima in the patterns of Skalare were not always found in the boresight direction, and therefore some of these patterns are shifted to compensate for this measurement inaccuracy.

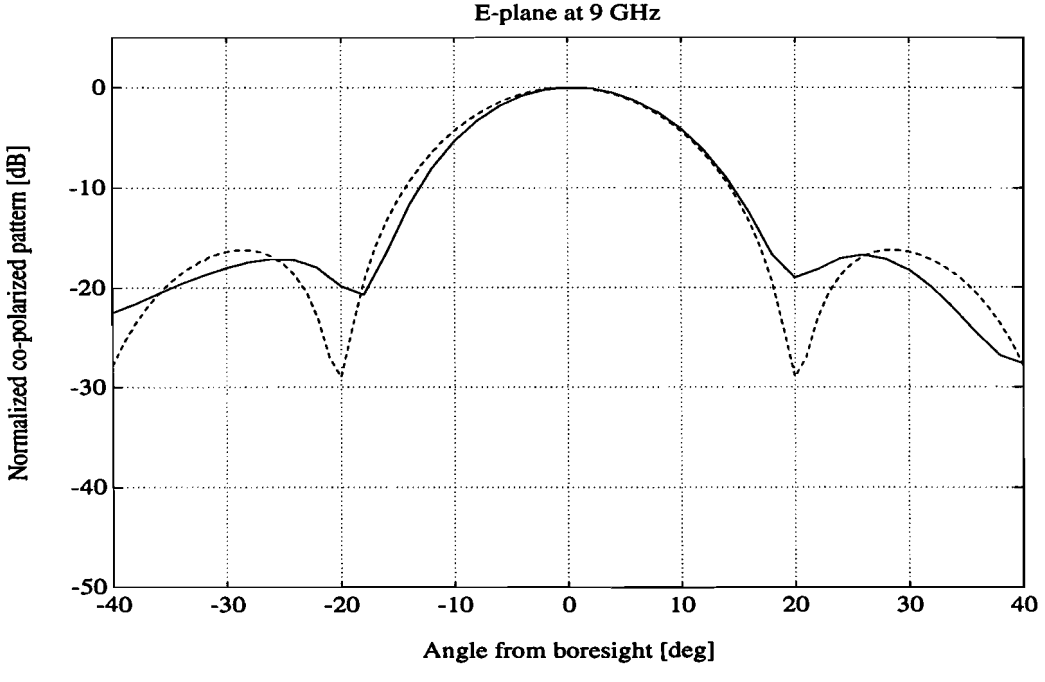

Figure 4.2 : Normalized co-polarized patterns of a double-dipole with a backing reflector on an elliptical HDP lens (solid line: Skalare, and dashed line: EUT).

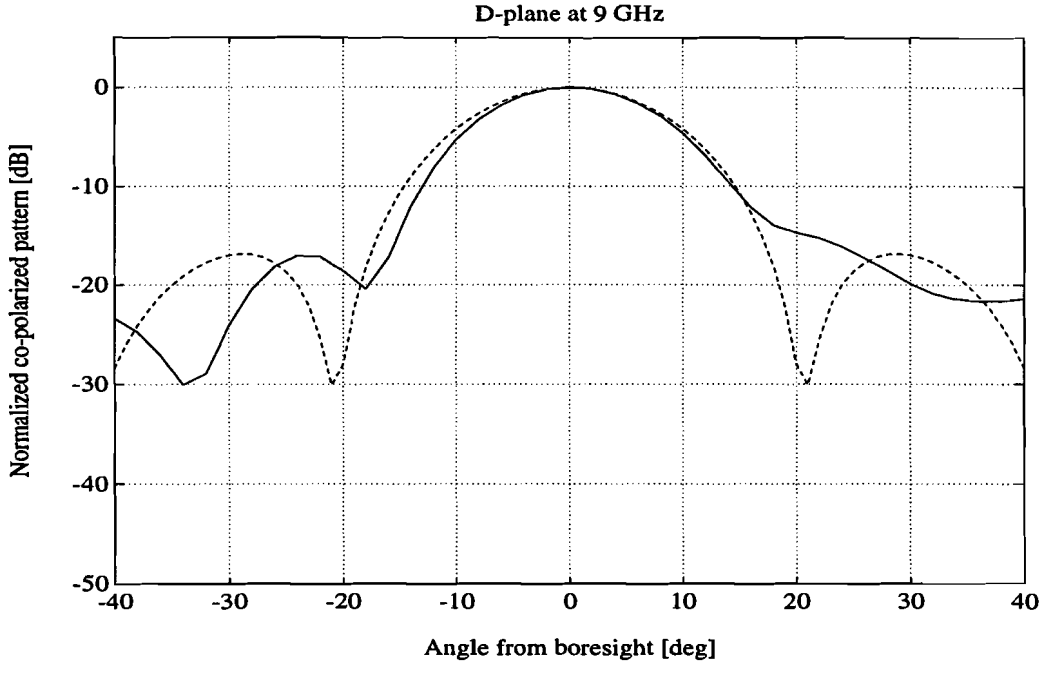

***Figure 4.3** : Normalized co-polarized patterns of a double-dipole with a backing reflector on an elliptical HDP lens (solid line: Skalare, and dashed line: EUT).*

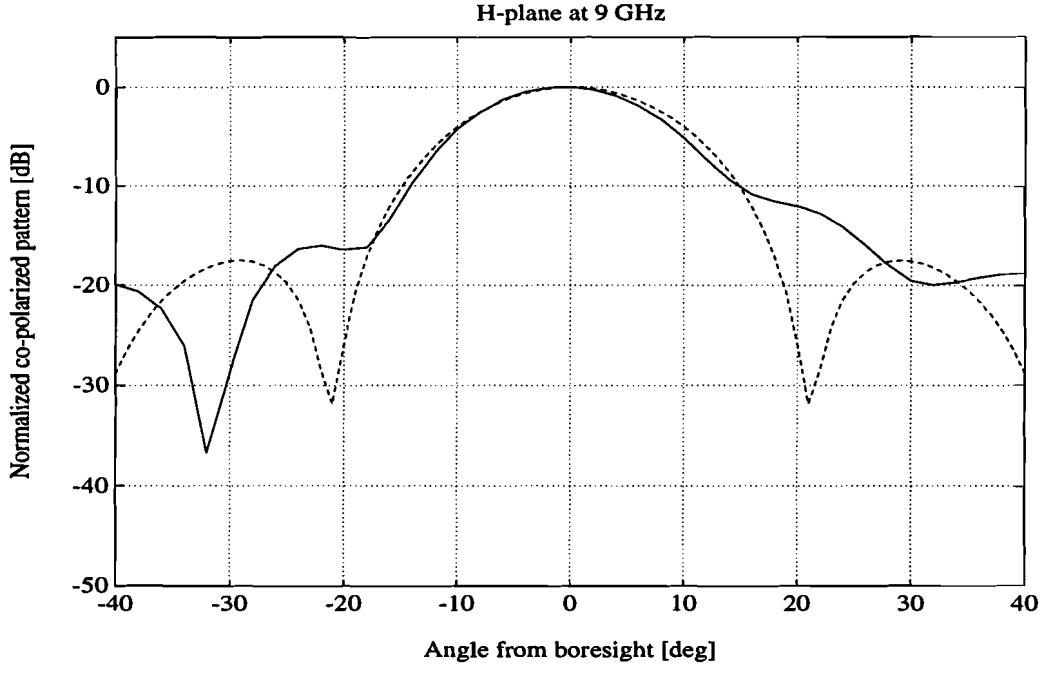

***Figure 4.4** : Normalized co-polarized patterns of a double-dipole with a backing reflector on an elliptical HDP lens (solid line: Skalare, and dashed line: EUT).*

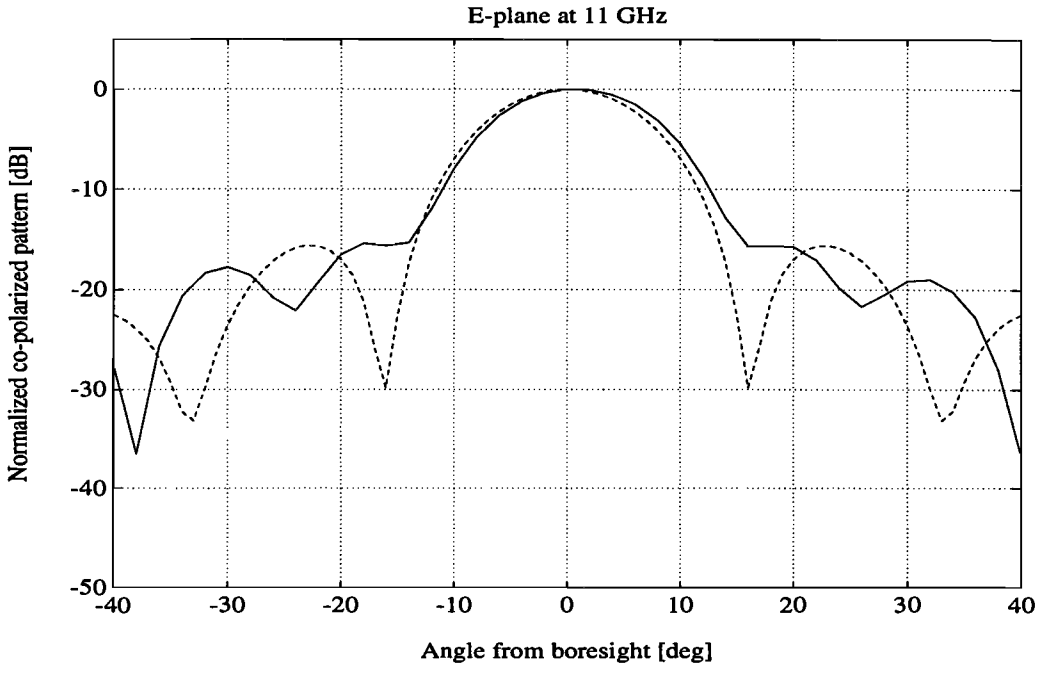

Figure 4.5 : Normalized co-polarized patterns of a double-dipole with a backing reflector on an elliptical HDP lens (solid line: Skalare, and dashed line: EUT).

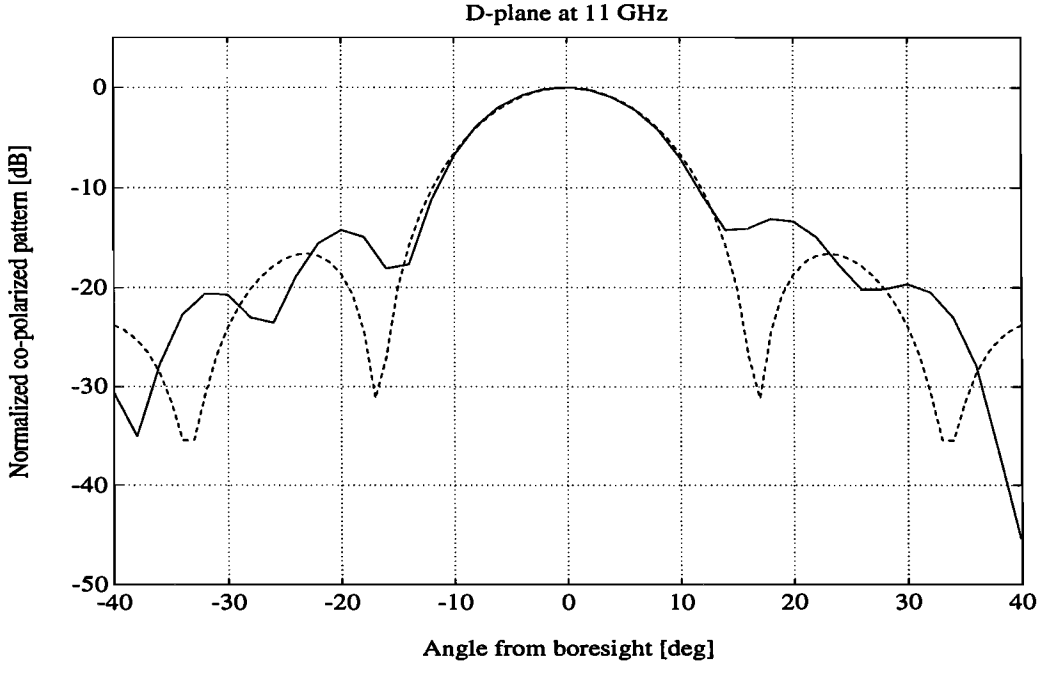

Figure 4.6 : Normalized co-polarized patterns of a double-dipole with a backing reflector on an elliptical HDP lens (solid line: Skalare, and dashed line: EUT).

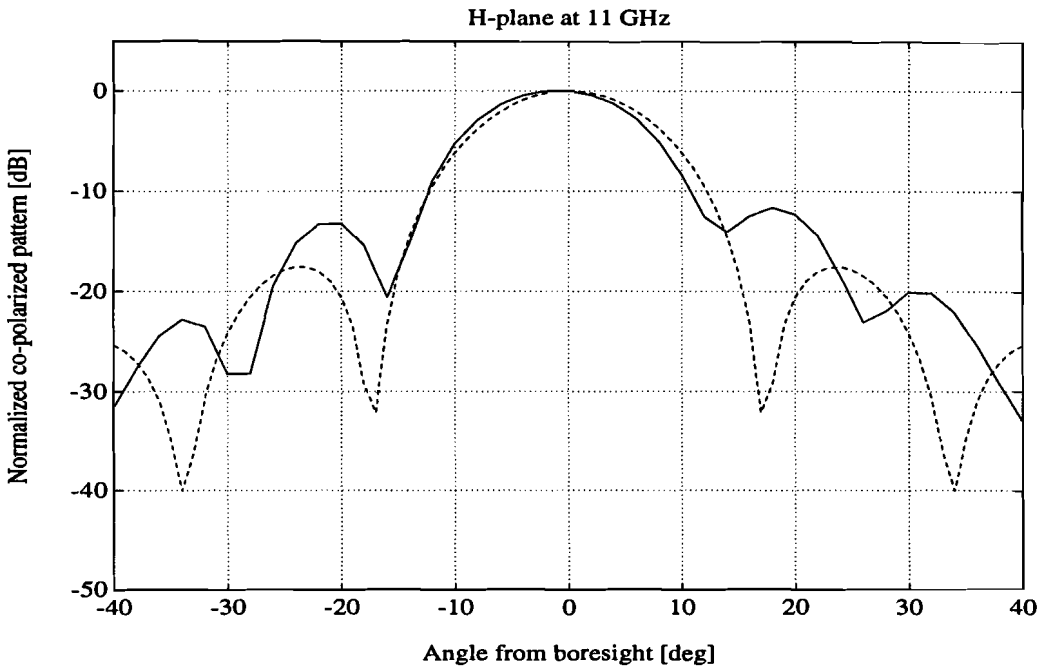

***Figure 4.7** : Normalized co-polarized patterns of a double-dipole with a backing reflector on an elliptical HDP lens (solid line: Skalare, and dashed line: EUT).*

Figures 4.2 to 4.7 show that the agreement between our model and the measured data is only valid for the main lobe down to a level of approximately -10 dB. For levels even lower than -10 dB the two do not agree well. An explanation for the discrepancies is that the model presented in this report does not take into account the lens reflected rays, which will interfere with the direct rays after a second reflection at the backing reflector. Of course these reflected rays are usually not as strong as the direct rays, especially for small angles from boresight, and therefore they will only influence the radiation pattern for angles outside the main lobe. The sidelobes will definitely be changed, if these reflected rays are considered.

Another observation that can be made is that the measured patterns are not symmetrical around 0°. The reason for this asymmetry is probably found in Figure 4.1, where one can see that the feed antenna is symmetric but the location of the IF and DC bias line at one side of the feed antenna makes the design asymmetric. It is very well possible that the IF and DC bias line will affect the radiation pattern especially in the H-plane. The E-plane radiation pattern on the other hand will not be affected that much by this bias line, because the bias line is perpendicular to this plane. Indeed, it appears that the H- and D-plane are less symmetric than the E-plane for both 9.0 and 11.0 GHz.

Due to the differences between the computed and the measured co-polarized patterns and the fact that the cross-polarized components are much smaller, it is not considered to be very useful to compare the cross-polarized patterns because of the more important role that the lens reflected rays will play.

5. Conclusions and Recommendations

5.1 Conclusions

In this report the performance of integrated lens antennas, with an elliptical or an extended hemispherical lens, is determined. The feed antenna, a double-slot or a double-dipole antenna with a backing reflector, is etched on the dielectric and illuminates the surface of the lens. By applying Geometrical Optics from the feed to the lens cap and an electric- and magnetic-field integration over the lens surface, the radiation patterns and some important efficiencies are computed. The directivity of the silicon elliptical lens antenna, with a diameter of 15.0 mm and a double-slot feed, appears to be 29.4 dBi at a frequency of 246 GHz. This is 0.8 and 2.6 dB more than the directivity of a quartz and a HDP dielectric, respectively. Of course the comparison is made, based on equally sized apertures as the silicon lens antenna. For the double-dipole feed with a backing reflector the directivity is usually somewhat higher. The beamwidths for the three dielectric materials (silicon, quartz and HDP) are around 8° at 246 GHz for both above-mentioned feeds. Increasing the frequency from 246 to 500 GHz results in a beamwidth of around 4°.

When the sidelobe envelopes and especially the relative first sidelobe levels are considered, it is found that the silicon dielectric lens design has the best performance. This design achieves a relative first sidelobe level of nearly -18 dB for the double-slot as well as for the double-dipole feed with backing reflector. For the other two dielectric materials the relative first sidelobe levels are approximately 2.5 dB worse. It is important to note that all these levels are calculated in the E-plane, because in this plane the worst levels are found. In most applications, the integrated lens antennas will be used as a feed for a parabolic reflector and therefore it is of great importance to know the part of the total radiated power that is captured within the main beam. In other words, the beam efficiency is another very interesting parameter. The beam efficiency computations show different results, ranging from 70 to 90%. Again silicon results in the best solution concerning the beam efficiency, which is normalized to the power radiated through the lens cap and not to the total radiated power.

In quasi-optical antenna systems the Gaussian beam efficiency plays a major role, because a perfect Gaussian beam results in the smallest possible optics. For the Gaussian beam efficiency of the elliptical lens antennas values from 70 to 90% are found, depending on which dielectric and which feed antenna is used. The best results are achieved (90.2%) using a silicon lens illuminated by a double-dipole feed with a backing reflector. The Gaussian beam efficiency can be increased to about 97%, if the elliptical lens is replaced by an extended hemispherical lens with a small extension length (1000-1200 μm). However, the directivity will decrease rapidly when the extension length is made smaller. At 1200 μm the directivity is less than 13 dBi for a lens with a 15.0 mm diameter. A comparison between the elliptical and the synthesized elliptical lens shows that the radiation patterns are quite similar within the main beam and that the elliptical lens has a slightly better directivity. Also the beamwidth is smaller for the true ellipse, 8.8 against 9.6°, but concerning the relative first sidelobe levels the synthesized elliptical lens appears to be the best solution.

Finally, our co-polarized radiation patterns are compared with the co-polarized radiation patterns obtained from measurements. This comparison, with a double-dipole illuminating a HDP elliptical lens at different frequencies, showed that only for the main beam a good agreement could be found. For angles outside the main beam, our model predicted sidelobes at other angles in the radiation patterns than the measurements did.

5.2 Recommendations

In the introduction of this report many different integrated antenna types are mentioned that could be used for the millimeter-wave and submillimeter-wave region. It is therefore recommended to analyze also these integrated antennas and compare them with the integrated lens antennas discussed in this report. Especially, the beam efficiency, the Gaussian beam efficiency and the rotation symmetry should be investigated, because of their great importance in most millimeter-wave and submillimeter-wave system applications, such as radiometry (limb sounding), radar, plasma diagnostics and radio astronomy. Another recommendation is to analyze other planar feed antennas than the ones used in this report, i.e. double-slot and double-dipole antenna with a backing reflector. For example the double-dipole antenna without a backing reflector, the spiral antenna or the log-periodic antenna could be considered. Then it is also interesting to find the optimal length and spacing of a double-slot or double-dipole feed for the best achievable rotation symmetry or Gaussian beam efficiency.

The comparison between the model presented in this report and the results obtained by measurements shows that our model is not complete yet. The discrepancies can probably be explained by the multiple reflected rays, which are not yet included in our model. It is expected that these contributions are the main reason for the observed differences at larger angles from boresight, because the amplitudes of the reflected rays are much smaller than the amplitudes of the direct rays and therefore they will only have an influence on the radiation pattern outside the main beam. Another option is to reduce the multiple reflection contributions by application of a matching layer between the surface of the lens and the air. This second option is more strongly recommended but askes for an analysis of the bandwidth of such a layer. In this report, the input impedance of the planar antennas on a dielectric substrate are not calculated. Nevertheless, the importance of this antenna property becomes clear when the antenna and the active circuit are combined on the same dielectric substrate and therefore have to be matched.

Acknowledgements

The author of this graduation report likes to thank everyone from the XE-division at ESA/ESTEC for the nice time spent and their constructive discussions. Especially dr. N.E. Jensen and dr. A. Roederer are acknowledged for the opportunity they gave me to do my graduation work at ESA/ESTEC in the XEA-section. Further, I would like to thank all the people from the Telecommunications division (EC) for the memorable talks we had during the coffee breaks. This report could not have been completed without the help of dr. D. Filipovic and dr. A. Skalare, because they gave me the results of their calculations and measurements and for that they are acknowledged. Finally, I am very grateful to prof.dr. G. Rebeiz for the nice discussion we had.

References

[1] D.F. Filipovic, S.S. Gearhart and G.M. Rebeiz
Double-slot antennas on extended hemispherical and elliptical silicon dielectric lenses,
IEEE Trans. on Microwave Theory Tech., vol. 41, pp. 1738-1749, 1993.

[2] S.S. Gearhart et al.
A wide-band 760-GHz planar integrated Schottky receiver,
IEEE Microwave and Guided Wave Letters, vol. 3, pp. 205-207, 1993.

[3] P.H. Sigel and R.J. Dengler
The dielectric-filled parabola: a new millimeter/submillimeter wavelength receiver/transmitter front end,
IEEE Trans. Antennas Propagat., vol. 39, pp. 40-47, 1991.

[4] G.V. Eleftheriades et al.
Millimeter-wave integrated-horn antennas, Part I: Theory,
IEEE Trans. Antennas Propagat., vol. 39, pp. 1575-1581, 1991.

[5] B. Carli, H. Fisher and J. Pyle
Limb Sounding Techniques for Environmental Monitoring in the Nineties,
Noordwijk: ESA ESTEC, 1992.

[6] D.B. Rutledge, D.P. Neikirk and D.P. Kasilingam
Integrated circuit antennas,
Infrared and Millimeter-waves, vol. 10, K.J. Button, Ed.,
New York: Academic Press, pp. 1-90, 1983.

[7] W. van Etten and J. van der Plaats
Fundamentals of Optical Fiber Communications,
Prentice Hall International (UK), 1991.

[8] A. Skalare
A dipole antenna feed for a dielectric lens surface,
SRON Final Report on Antenna Development, Jan. 1990.

[9] J.D. Kraus
Antennas,
McGraw-Hill, 1950.

[10] M. Kominami, D.M. Pozar and D.H. Schaubert
Dipole and slot elements and arrays on semi-infinite substrates,
IEEE Trans. Antennas Propagat., vol. 33, pp. 600-607, 1985.

[11] R.S. Elliott
Antenna Theory and Design,
New Jersey: Prentice-Hall, ch. 4, 1981.

[12] G.M. Rebeiz
Millimeter-wave and Terahertz integrated circuit antennas,
Proc. IEEE, vol. 80, pp. 1748-1770, 1992.

[13] R.E. Collin
Antennas and Radiowave Propagation,
New York: McGraw-Hill, ch. 4, 1985.

[14] C.A. Balanis
Antenna Theory: Analysis and Design,
New York: Wiley, ch. 11, 1982.

[15] S.E. Schwarz
Efficiency of quasi-optical couplers,
Int. J. Infrared Millimeter Waves, vol. 5, pp. 1517-1525, 1984.

[16] E. Hecht
Optics,
MA: Addison-Wesley, 2nd Edition, pp. 129-131, 1987.

[17] T.H. Buttgenbach
An improved solution for integrated array optics in quasi-optical mm and submm receivers: the hybrid antenna,
IEEE Trans. on Microwave Theory Tech., vol. 41, pp. 1750-1760, 1993.

[18] A.C. Ludwig
The definition of cross polarization,
IEEE Trans. Antennas Propagat., vol. 21, pp. 116-119, 1973.

[19] P.F. Goldsmith
Quasi-optical techniques at millimeter and submillimeter wavelengths,
Infrared and Millimeter-waves, vol. 6, K.J. Button, Ed.,
New York: Academic Press, 1982.

Appendix A: Derivation of the Fresnel reflection and transmission coefficients:

* Perpendicular polarization:

The configuration of the problem is shown in Figure A.1.

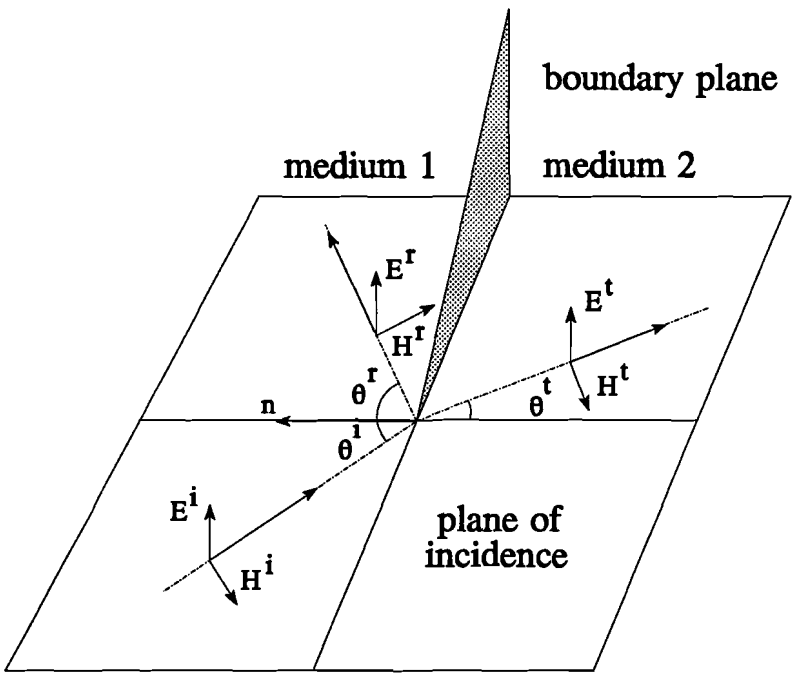

***Figure A.1** : Perpendicular polarization.*

The E-vector is perpendicular to the plane of incidence. The boundary conditions are:

$$E^i + E^r = E^t \tag{A.1}$$

$$H^i\cos\theta^i - H^r\cos\theta^r = H^t\cos\theta^t \tag{A.2}$$

For the magnetic field strengths it is possible to write:

$$H^i = \frac{E^i}{Z_1}\ ,\ H^r = \frac{E^r}{Z_1}\ ,\ H^t = \frac{E^t}{Z_2} \tag{A.3}$$

Substitution of Equation (A.3) into (A.2) gives:

$$E^i\cos\theta^i - E^r\cos\theta^r = \frac{Z_1}{Z_2}E^t\cos\theta^t \tag{A.4}$$

Elimination of E^t or E^r from Equations (A.1) and (A.4) leads to the following reflection and transmission coefficients:

$$\rho_\perp \triangleq \frac{E^r}{E^i} = \frac{Z_2\cos\theta^i - Z_1\cos\theta^t}{Z_2\cos\theta^r + Z_1\cos\theta^t} \tag{A.5}$$

$$\tau_\perp \triangleq \frac{E^t}{E^i} = \frac{Z_2\cos\theta^i + Z_2\cos\theta^r}{Z_2\cos\theta^r + Z_1\cos\theta^t} \tag{A.6}$$

* Parallel polarization:

Now, the E-vector is parallel to the plane of incidence,which is shown in Figure A.2.

The boundary conditions are given by:

$$H^i + H^r = H^t \tag{A.7}$$

$$E^i\cos\theta^i - E^r\cos\theta^r = E^t\cos\theta^t \tag{A.8}$$

Substitution of Equation (A.3) into (A.7) leads to the following equation:

$$E^i + E^r = \frac{Z_1}{Z_2}E^t \tag{A.9}$$

By eliminating E^r or E^t from Equations (A.8) and (A.9) the reflection and transmission coefficients for the parallel polarization are obtained:

$$\rho_\parallel \triangleq \frac{E^r}{E^i} = \frac{Z_1\cos\theta^i - Z_2\cos\theta^t}{Z_1\cos\theta^r + Z_2\cos\theta^t} \tag{A.10}$$

$$\tau_{\perp} \triangleq \frac{E^t}{E^i} = \frac{Z_2 \cos\theta^i + Z_2 \cos\theta^r}{Z_1 \cos\theta^r + Z_2 \cos\theta^t} \tag{A.11}$$

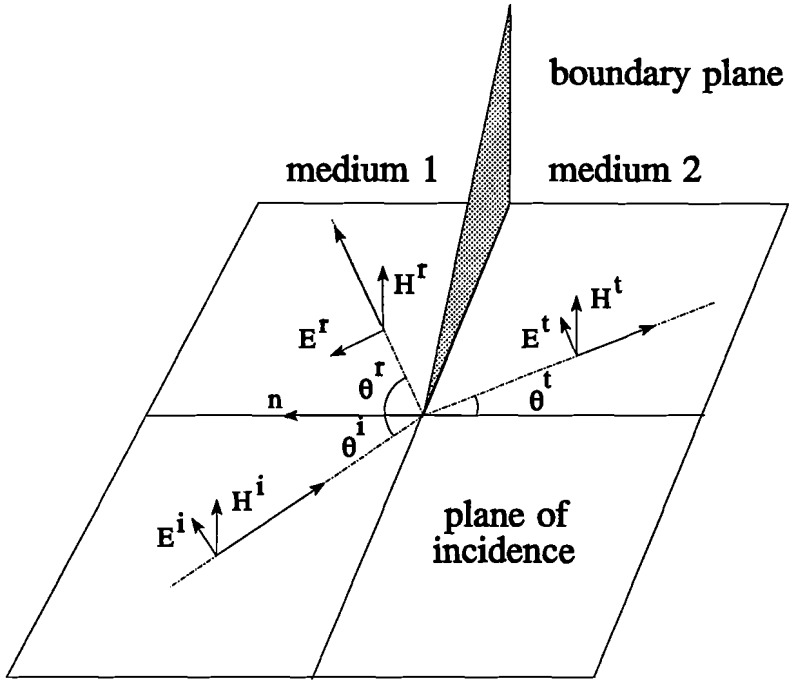

***Figure A.2** : Parallel polarization.*

Appendix B: Aperture- and far-field representation of a first-order Gaussian beam:

The first-order Gaussian beam can be seen as an approximate solution to the (scalar) Helmholtz-equation $\nabla^2 E + k^2 E = 0$. In Figure B.1 the contour of the first-order Gaussian beam is shown.

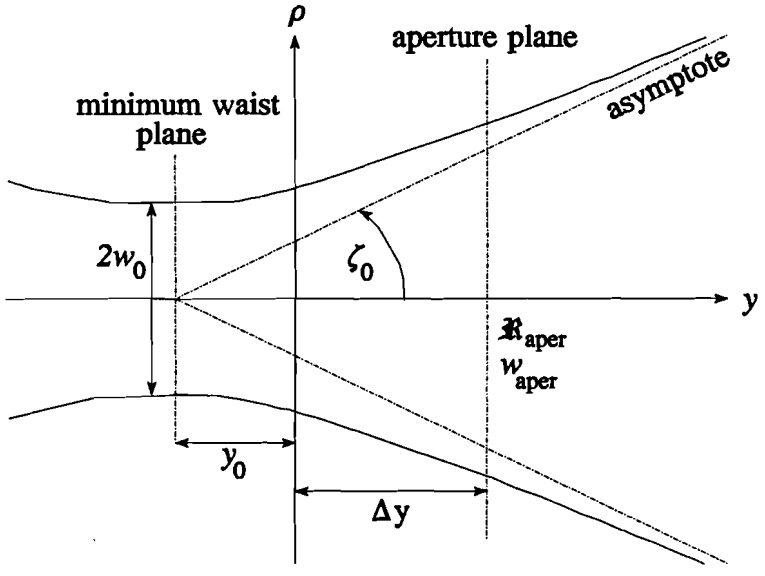

Figure B.1 : Contour of a first-order Gaussian beam.

For the lower order, or fundamental Gaussian mode, the two-dimensional rotationally symmetric field representation can be expressed as [19]:

$$\underline{E}(\rho,y) = \hat{n}_{co} A \frac{w_0}{w} \exp\left[\frac{-\rho^2}{w^2} - jk\frac{\rho^2}{2\Re} - jk(y_0+y) + j\arctan\frac{2(y+y_0)}{kw_0^2}\right] \qquad \text{(B.1)}$$

where A, w_0 are constants, and w and $\Re$ are slowly varying functions of y. From Equation (B.1) can be seen that the variation of the field amplitude transverse to the direction of

propagation has a Gaussian form with the half-width to the 1/e point being equal to w, which is called the beam radius. The variation of w as a function of y is given by:

$$w(y) = w_0 \sqrt{1 + \frac{4(y+y_0)^2}{k^2 w_0^4}} \tag{B.2}$$

Also the radius of curvature $\Re$ depends on the distance from the minimum waist plane and can be written as:

$$\Re(y) = \frac{4(y+y_0)^2 + k^2 w_0^4}{4(y+y_0)} \tag{B.3}$$

Now that the two-dimensional field of the first-order Gaussian beam is known, the next step is to find the radiation-field pattern of this fundamental Gaussian beam. In Ref. [13] is shown that the far-field pattern of any planar aperture-field distribution equals the Fourier Transform of this aperture field as being:

$$\underline{E}(r) \sim \frac{jk\cos\zeta}{2\pi r} \exp(-jkr)\, \underline{\Psi}(k\sin\zeta\cos\delta, k\sin\zeta\sin\delta) \tag{B.4}$$

with

$$\underline{\Psi}(k_x, k_z) = \int_{-\infty}^{\infty}\int_{-\infty}^{\infty} \underline{E}^a(x,z)\exp(jk_x x + jk_z z)\, dk_x dk_z \tag{B.5}$$

which is the two-dimensional Fourier Transform of the field ($\underline{E}^a$) in the plane $y=0$. The calculation of the Fourier Transform of the fundamental Gaussian beam can be simplified, because it has a rotationally symmetric field distribution. With $k_x = k\sin\zeta\cos\delta$ and $k_z = k\sin\zeta\sin\delta$ and the introduction of cylindrical coordinates (ρ, ϕ') in the plane $y=0$, the Fourier Transform of a rotationally symmetric field reduces to:

$$\underline{\Psi}(\zeta) = 2\pi \int_0^{\infty} \underline{E}^a(\rho) J_0(k\rho\sin\zeta)\, \rho\, d\rho \tag{B.6}$$

If the field distribution of the first-order Gaussian beam, from Equation (B.1), is substituted in Equation (B.6) the following integral is obtained:

$$\underline{\Psi}(\zeta) = 2\pi \hat{n}_{co} \int_0^{\infty} A \frac{w}{w_0} \exp\left(\frac{-\rho^2}{w^2} - jk\frac{\rho^2}{2\Re} + j\xi\right) J_0(k\rho\sin\zeta)\, \rho\, d\rho \tag{B.7}$$

with ξ being a constant and the values of w and $\Re$ are the values at $y=0$. This integral can be evaluated with the help of the next standard integral:

$$\int_0^\infty \exp(-a^2t^2)J_0(bt)tdt = \frac{1}{2a^2}\exp(\frac{-b^2}{4a^2}) \qquad Re(a^2)>0 \tag{B.8}$$

and reduces to:

$$\underline{\Psi}(\zeta) = C\exp\left[\frac{\Re k^2w^2(2kw^2j-4\Re)\sin^2\zeta}{16\Re^2+4k^2w^4}\right] \tag{B.9}$$

In Equation (B.9) C is a complex constant. As said before, the Gaussian beam is a paraxial approximation, which implies that this approximation is only valid for small angles from boresight. Therefore, it is allowed to replace $\sin\zeta$ by ζ and $\cos\zeta$ by one. This finally results in the far-field representation of the first-order Gaussian beam as being:

$$\underline{E}(r) \sim \frac{jkC}{2\pi r}\exp(-jkr)\exp\left[\frac{\Re k^2w^2(2kw^2j-4\Re)\zeta^2}{16\Re^2+4k^2w^4}\right] \tag{B.10}$$

Comparing this expression with the far-field representation of the first-order Gaussian beam, used in the Gaussian beam efficiency calculations, which is:

$$D\exp(-\frac{\zeta^2}{\zeta_0^2})\exp(\pm j\pi\frac{\zeta^2}{\zeta_1^2}) \tag{B.11}$$

leads to the following two equations for ζ_0 and ζ_1:

$$\zeta_0^2 = \frac{16\Re^2+4k^2w^4}{4\Re^2k^2w^2} \tag{B.12}$$

$$\zeta_1^2 = \pm\pi\frac{16\Re^2+4k^2w^4}{2\Re k^3w^4} \tag{B.13}$$

Rewriting these equations for $\Re$ and w results in:

$$\Re = \frac{2\zeta_1^4 + 2\pi^2\zeta_0^4}{\pm k\pi\zeta_0^4\zeta_1^2} \tag{B.14}$$

and

$$w = \frac{2}{k\zeta_0\zeta_1^2}\sqrt{\zeta_1^4 + \pi^2\zeta_0^4} \tag{B.15}$$

It is good to note here that these values for $\Re$ and w are values with y being equal to zero. The next step is to find expressions for the radius of curvature and the beam radius in the aperture plane $y=\Delta y$. This is started by rewriting Equations (B.2) and (B.3) for w_0 and y_0. For these variables the next expressions hold:

$$w_0 = \frac{2w\Re}{\sqrt{4\Re^2 + k^2w^4}} \tag{B.16}$$

and

$$y_0 = \frac{\Re k^2 w^4}{4\Re^2 + k^2 w^4} \tag{B.17}$$

By substituting Equations (B.14) and (B.15) in Equations (B.16) and (B.17) it is easy to derive the following two equations:

$$w_0 = \frac{2}{k\zeta_0} \tag{B.18}$$

and

$$y_0 = \pm\frac{2\pi}{k\zeta_1^2} \tag{B.19}$$

The value of y_0 is positive if the minimum waist plane is located on the left side of the plane $y=0$. With the knowledge that both the distance from the minimum waist plane to the ρ-axis and the value of the minimum waist are known, it is not difficult to determine the radius of curvature and the waist radius in the aperture plane of the antenna.

Therefore, Equations (B.2) and (B.3) are applied together with Equations (B.18) and (B.19), yielding the values for $\Re_{aper}$ and w_{aper}:

$$w_{aper} = \frac{1}{k\zeta_0}\sqrt{4 + k^2\zeta_0^4\left[\Delta y + \frac{2\pi}{k\zeta_1^2}\right]^2} \tag{B.20}$$

and

$$\Re_{aper} = \frac{\left[\Delta y + \frac{2\pi}{k\zeta_1^2}\right]^2 + \frac{4}{k^2\zeta_0^4}}{\left[\Delta y + \frac{2\pi}{k\zeta_1^2}\right]} \tag{B.21}$$

Appendix C: Measured and calculated co-polarized patterns of a double-dipole fed lens antenna:

This appendix contains the co-polarized patterns of a double-dipole feed antenna with a backing reflector, which illuminates a HDP elliptical lens. The co-polarized patterns are measured and calculated at 7,8,10,12,13 and 14 GHz in the E-, D- and H-plane. The diameter of the lens was 11.0 cm. The double-dipole feed consisted of two half-wave dipoles with a spacing of $0.4\lambda_d$ and between the feed antenna and the backing reflector a quarter wavelength of HDP dielectric material was put. For the double-dipole feed an operating frequency of 10 GHz was chosen.

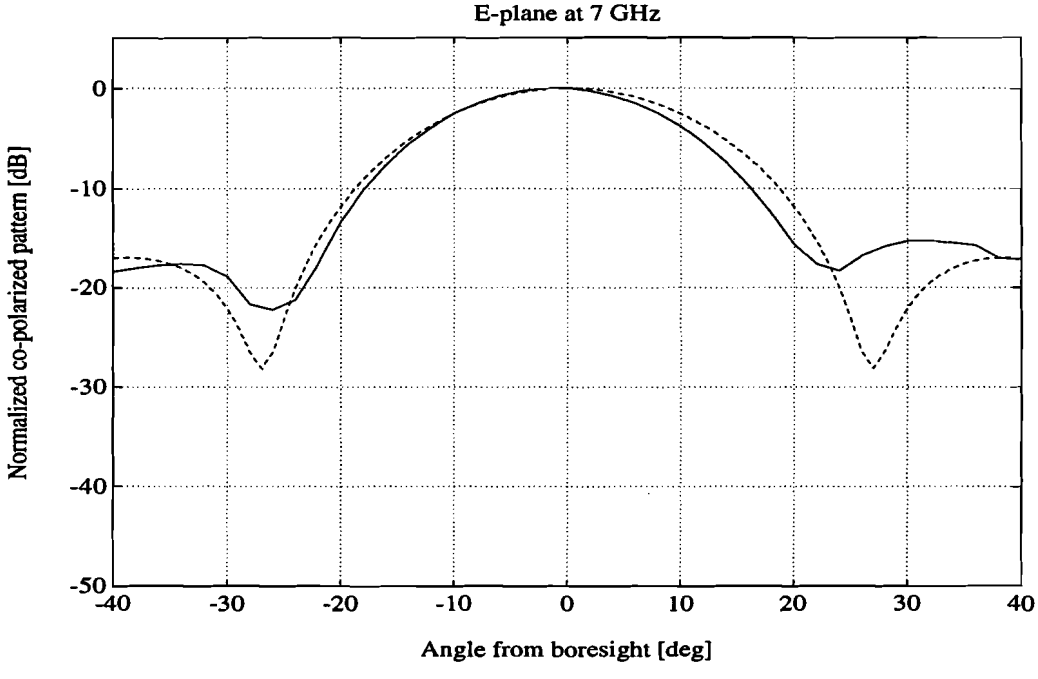

***Figure C.1** : Normalized co-polarized patterns of a double-dipole with a backing reflector on an elliptical HDP lens (solid line: Skalare, and dashed line: EUT).*

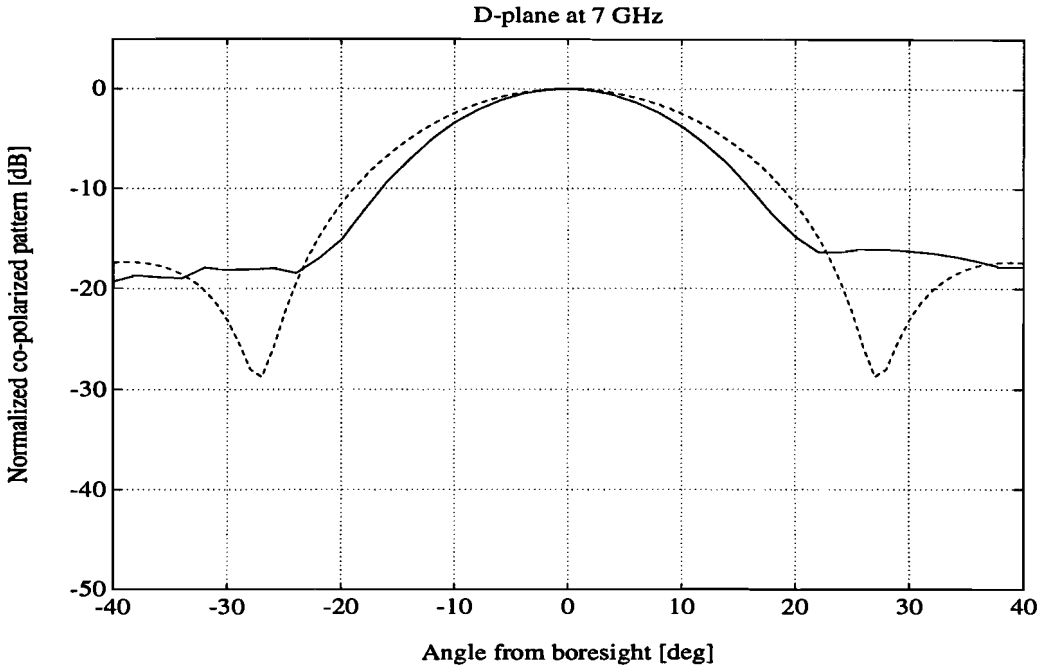

Figure C.2 : Normalized co-polarized patterns of a double-dipole with a backing reflector on an elliptical HDP lens (solid line: Skalare, and dashed line: EUT).

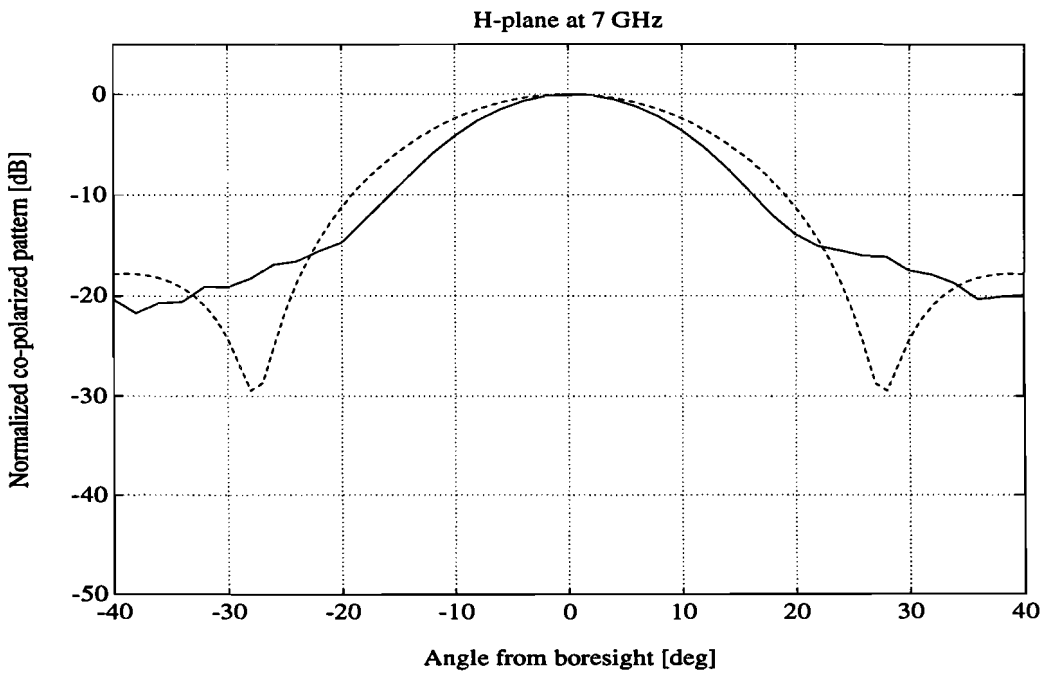

Figure C.3 : Normalized co-polarized patterns of a double-dipole with a backing reflector on an elliptical HDP lens (solid line: Skalare, and dashed line: EUT).

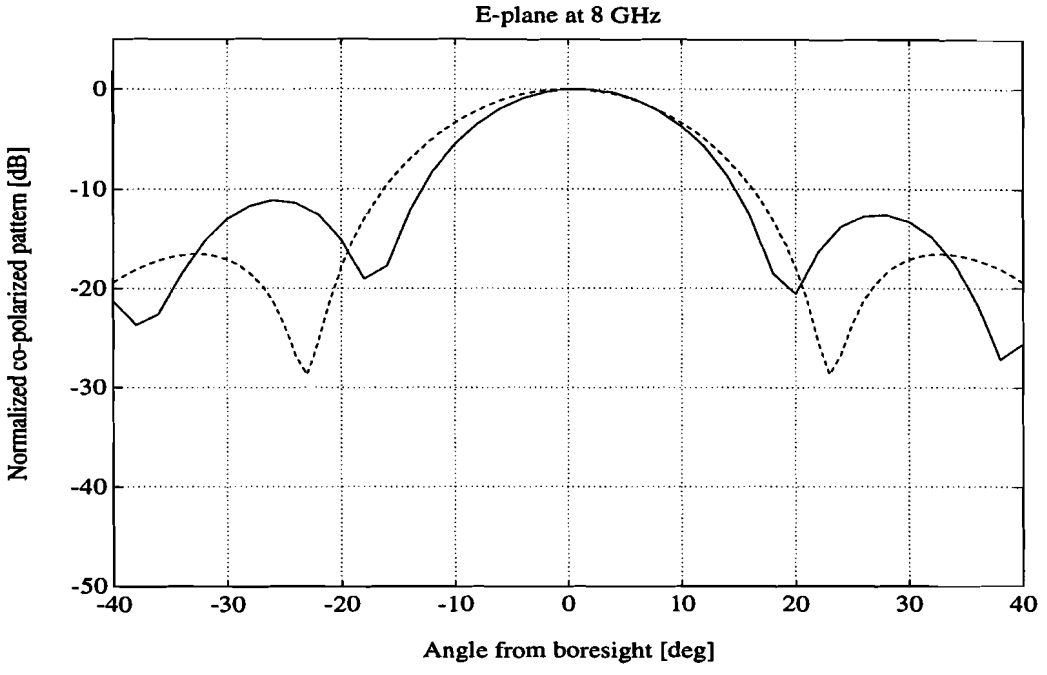

***Figure C.4** : Normalized co-polarized patterns of a double-dipole with a backing reflector on an elliptical HDP lens (solid line: Skalare, and dashed line: EUT).*

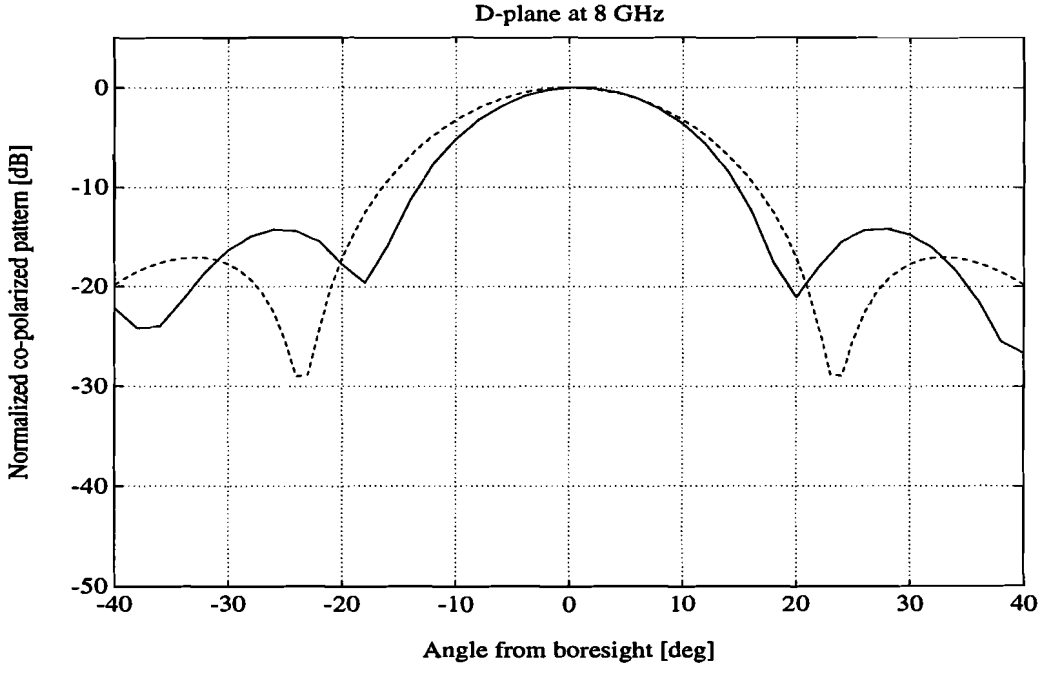

***Figure C.5** : Normalized co-polarized patterns of a double-dipole with a backing reflector on an elliptical HDP lens (solid line: Skalare, and dashed line: EUT).*

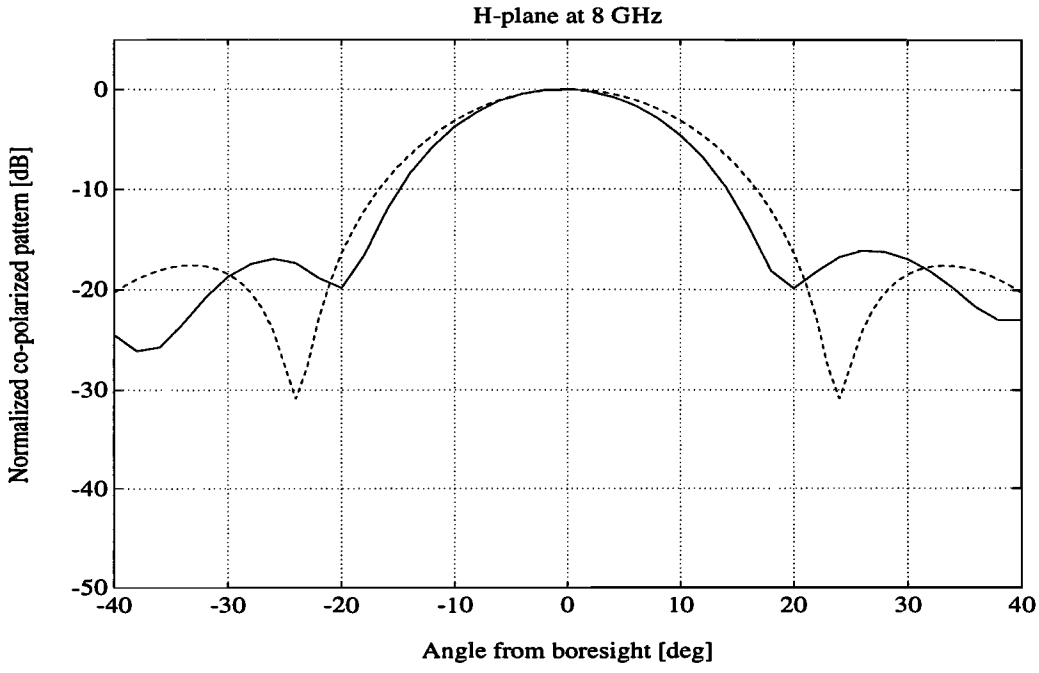

***Figure C.6** : Normalized co-polarized patterns of a double-dipole with a backing reflector on an elliptical HDP lens (solid line: Skalare, and dashed line: EUT).*

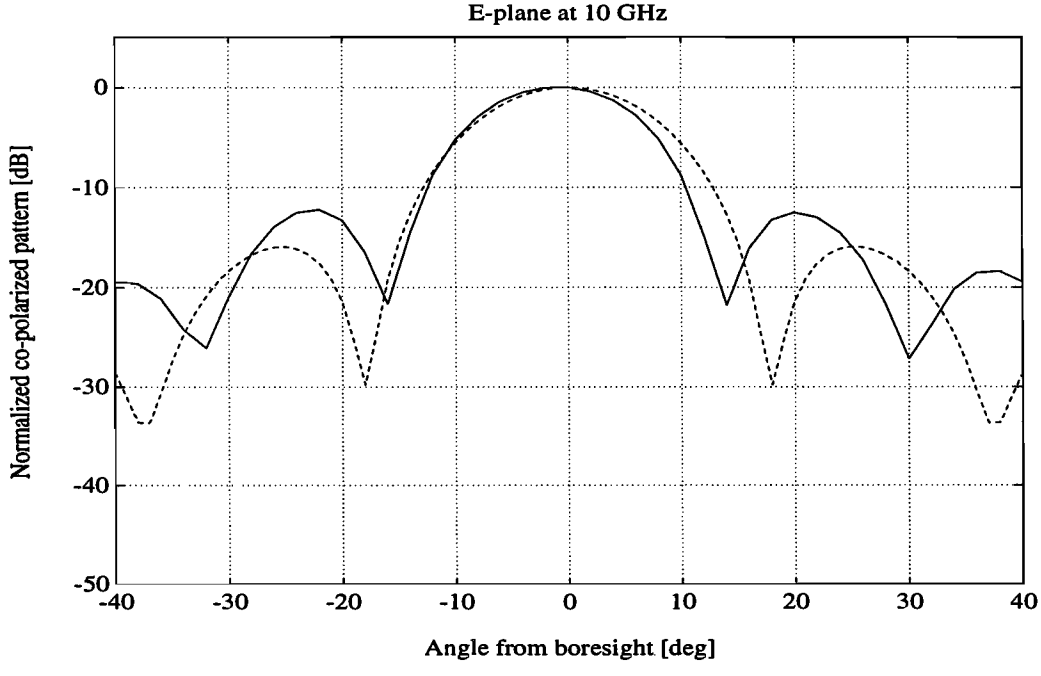

***Figure C.7** : Normalized co-polarized patterns of a double-dipole with a backing reflector on an elliptical HDP lens (solid line: Skalare, and dashed line: EUT).*

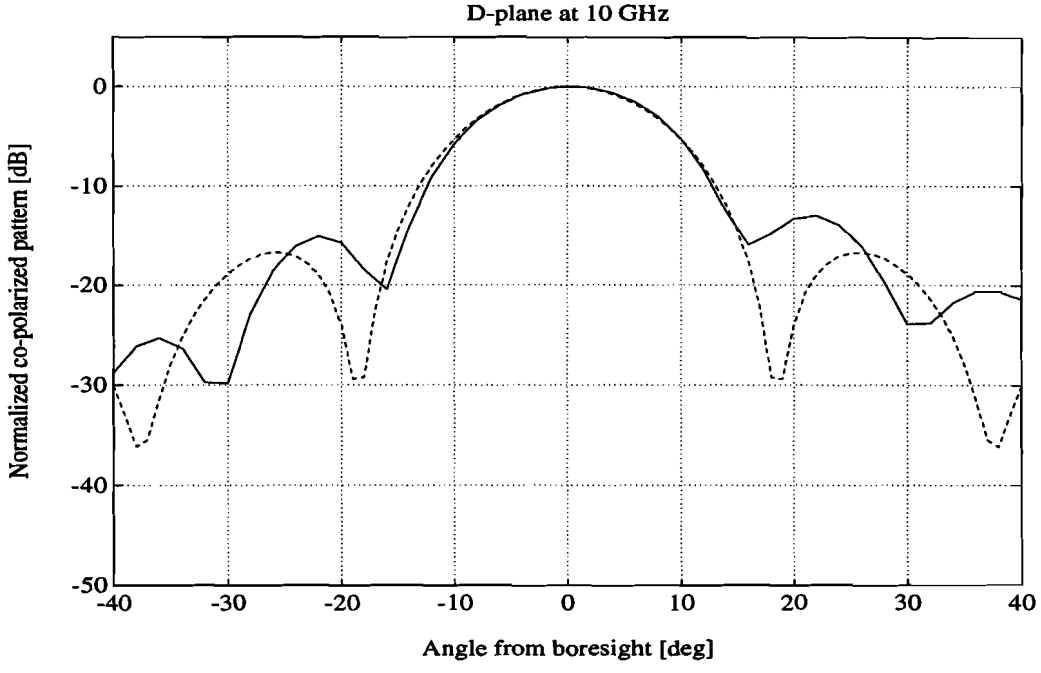

***Figure C.8** : Normalized co-polarized patterns of a double-dipole with a backing reflector on an elliptical HDP lens (solid line: Skalare, and dashed line: EUT).*

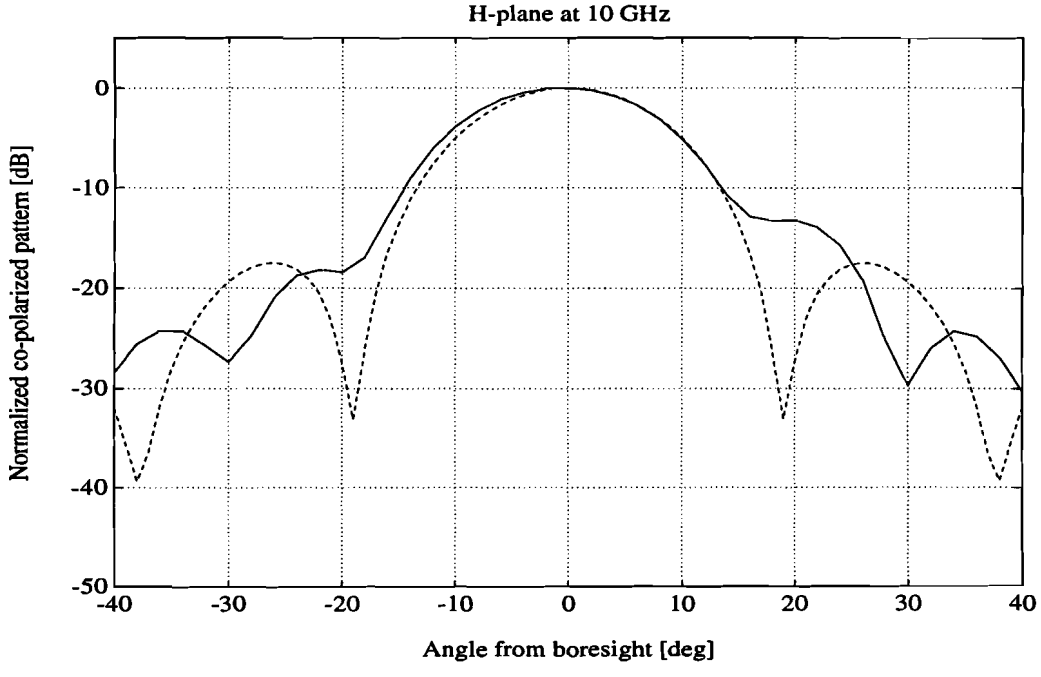

***Figure C.9** : Normalized co-polarized patterns of a double-dipole with a backing reflector on an elliptical HDP lens (solid line: Skalare, and dashed line: EUT).*

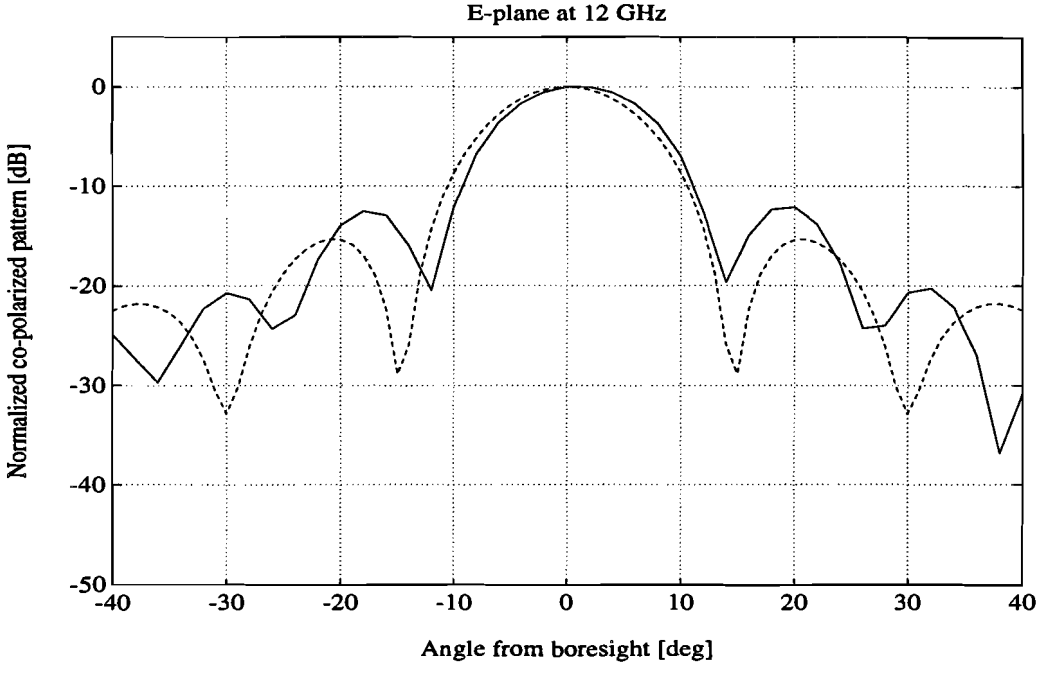

Figure C.10 : Normalized co-polarized patterns of a double-dipole with a backing reflector on an elliptical HDP lens (solid line: Skalare, and dashed line: EUT).

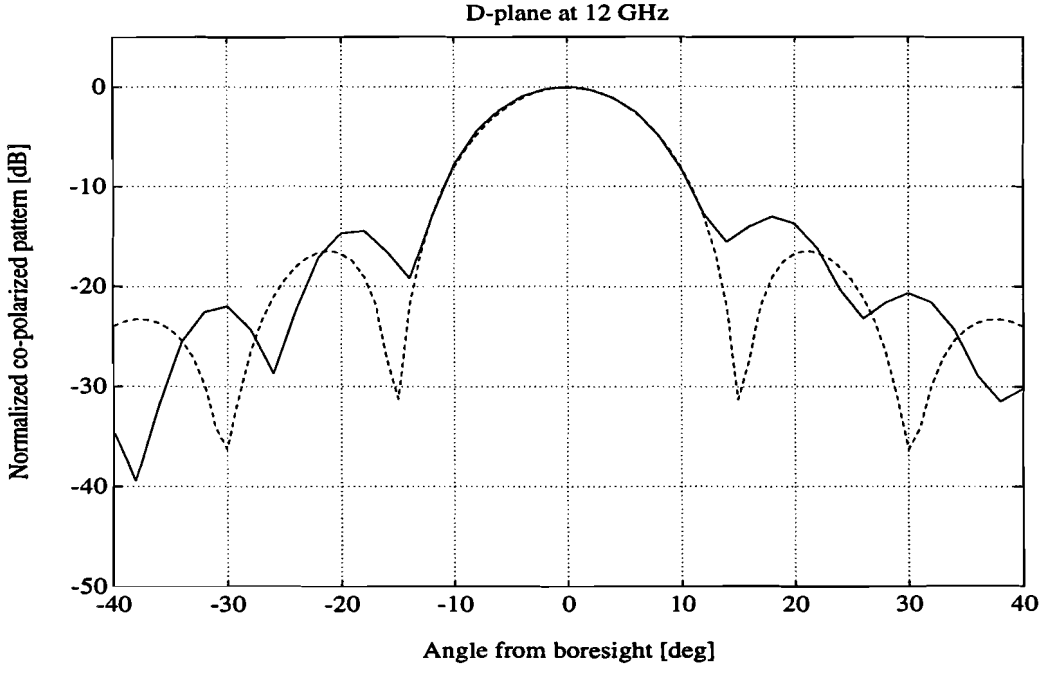

Figure C.11 : Normalized co-polarized patterns of a double-dipole with a backing reflector on an elliptical HDP lens (solid line: Skalare, and dashed line: EUT).

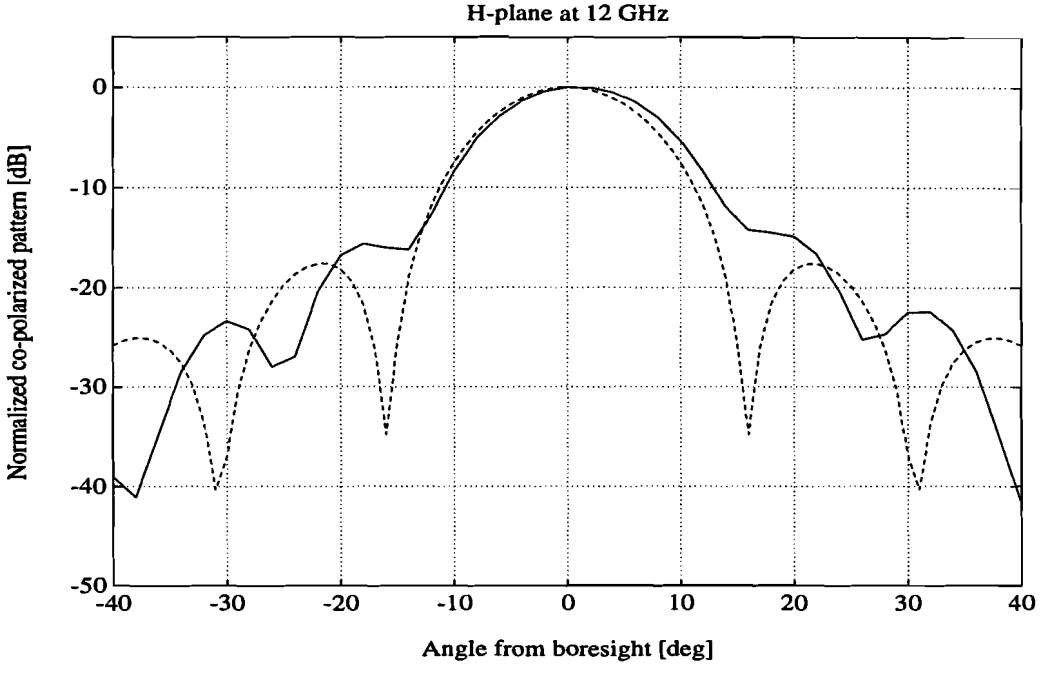

***Figure C.12** : Normalized co-polarized patterns of a double-dipole with a backing reflector on an elliptical HDP lens (solid line: Skalare, and dashed line: EUT).*

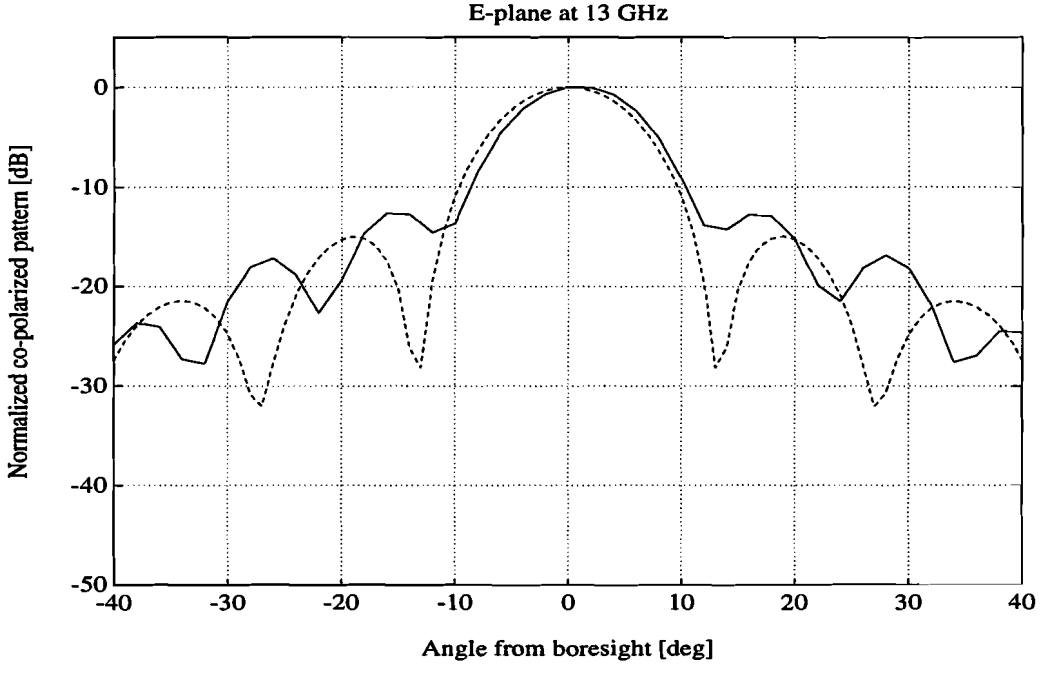

***Figure C.13** : Normalized co-polarized patterns of a double-dipole with a backing reflector on an elliptical HDP lens (solid line: Skalare, and dashed line: EUT).*

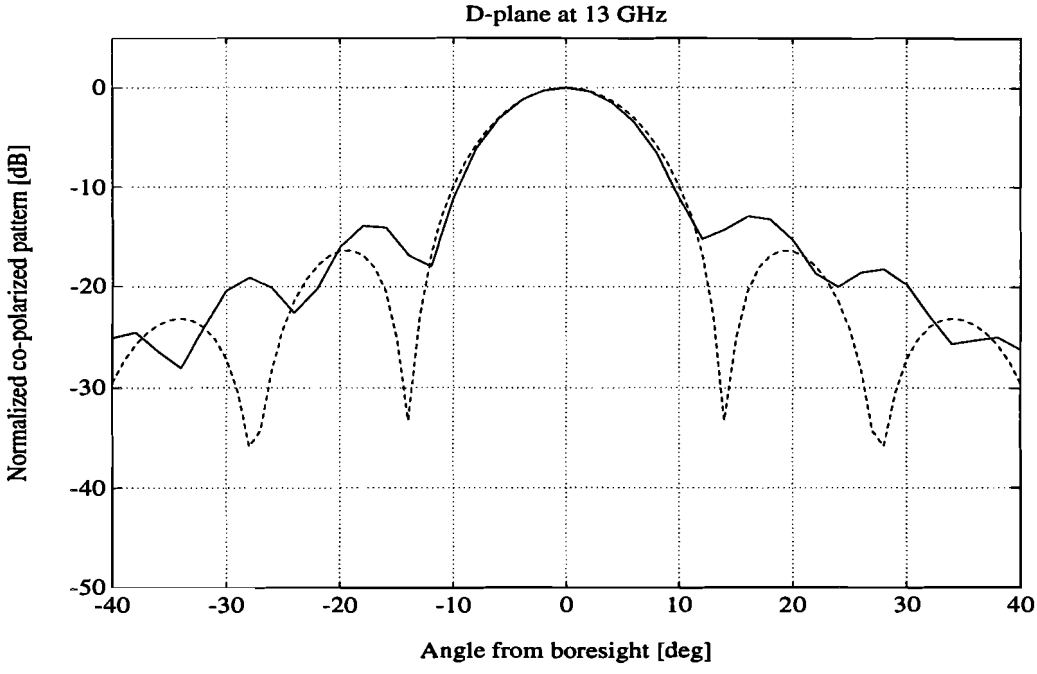

Figure C.14 *: Normalized co-polarized patterns of a double-dipole with a backing reflector on an elliptical HDP lens (solid line: Skalare, and dashed line: EUT).*

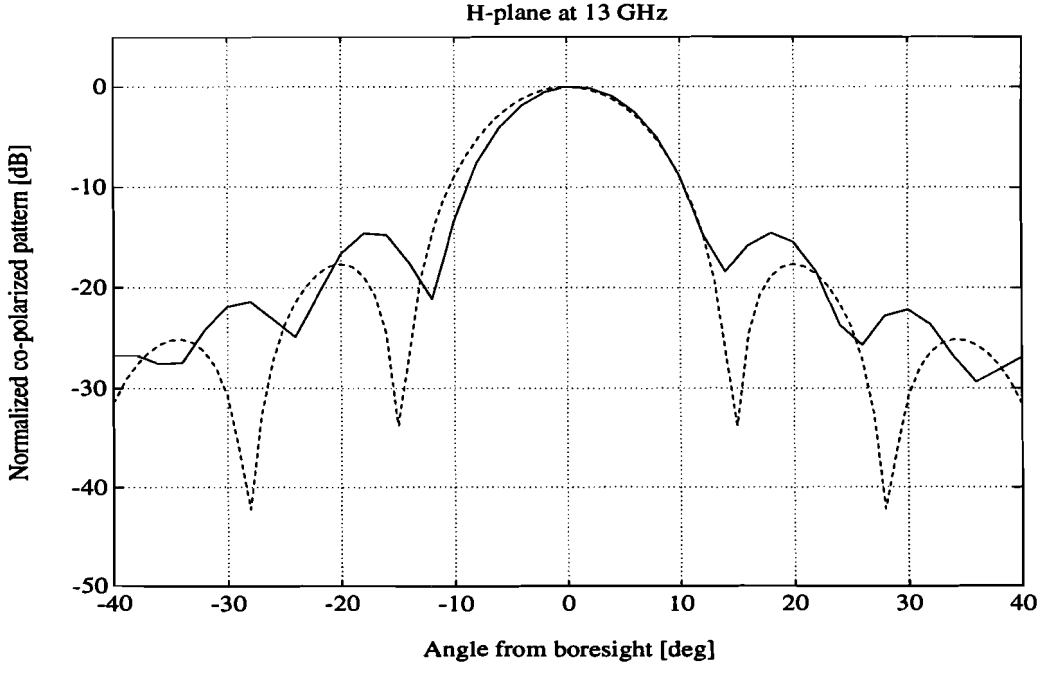

Figure C.15 *: Normalized co-polarized patterns of a double-dipole with a backing reflector on an elliptical HDP lens (solid line: Skalare, and dashed line: EUT).*

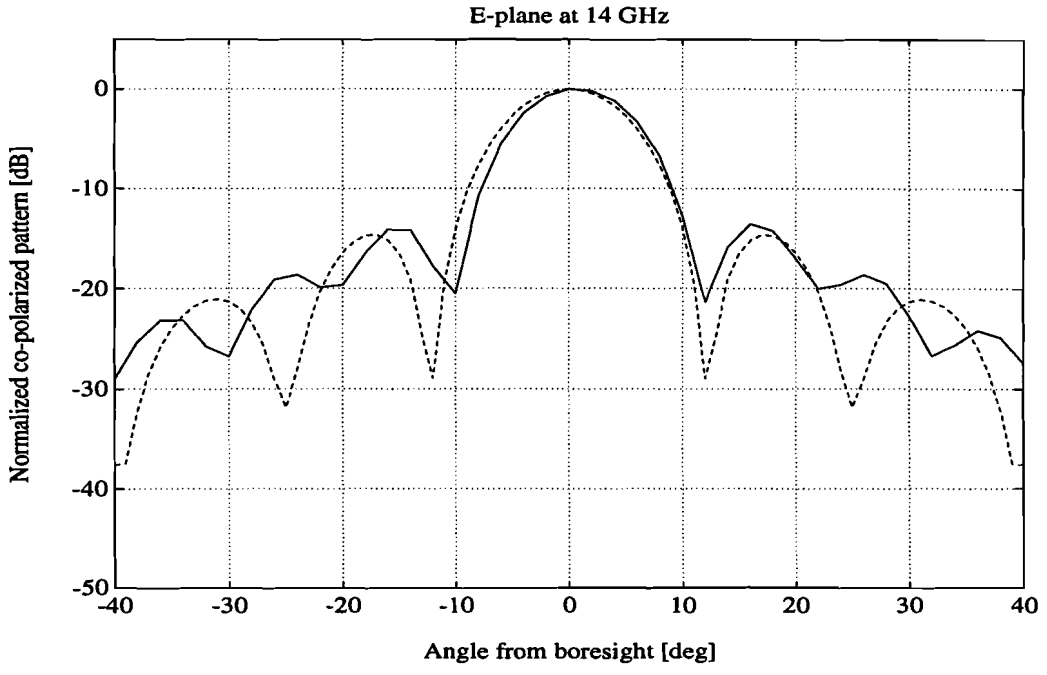

***Figure C.16** : Normalized co-polarized patterns of a double-dipole with a backing reflector on an elliptical HDP lens (solid line: Skalare, and dashed line: EUT).*

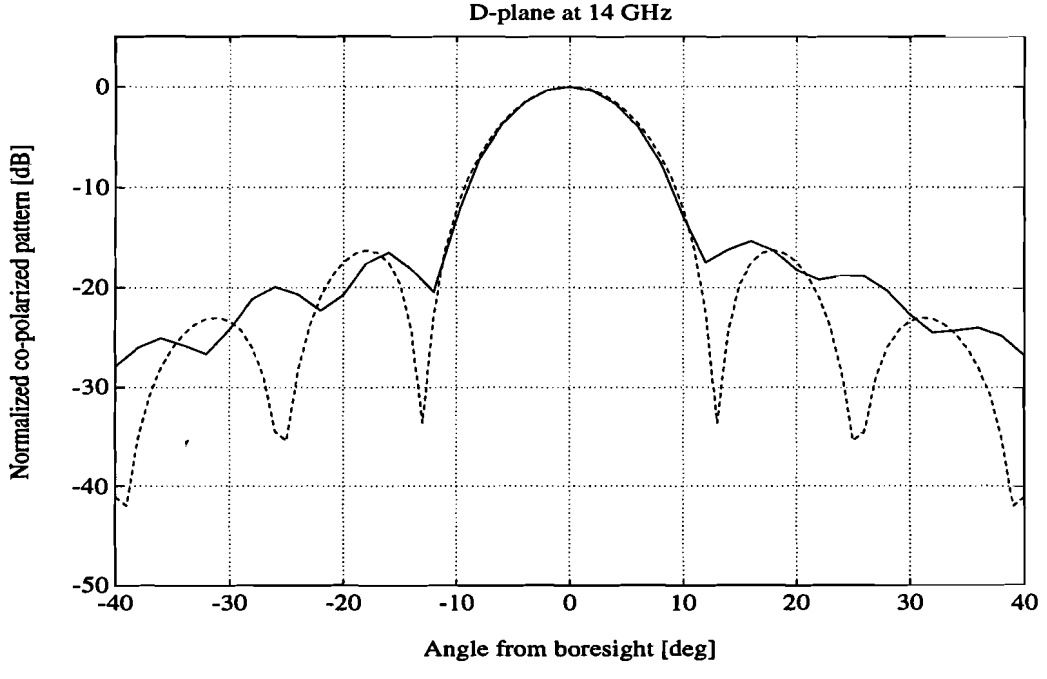

***Figure C.17** : Normalized co-polarized patterns of a double-dipole with a backing reflector on an elliptical HDP lens (solid line: Skalare, and dashed line: EUT).*

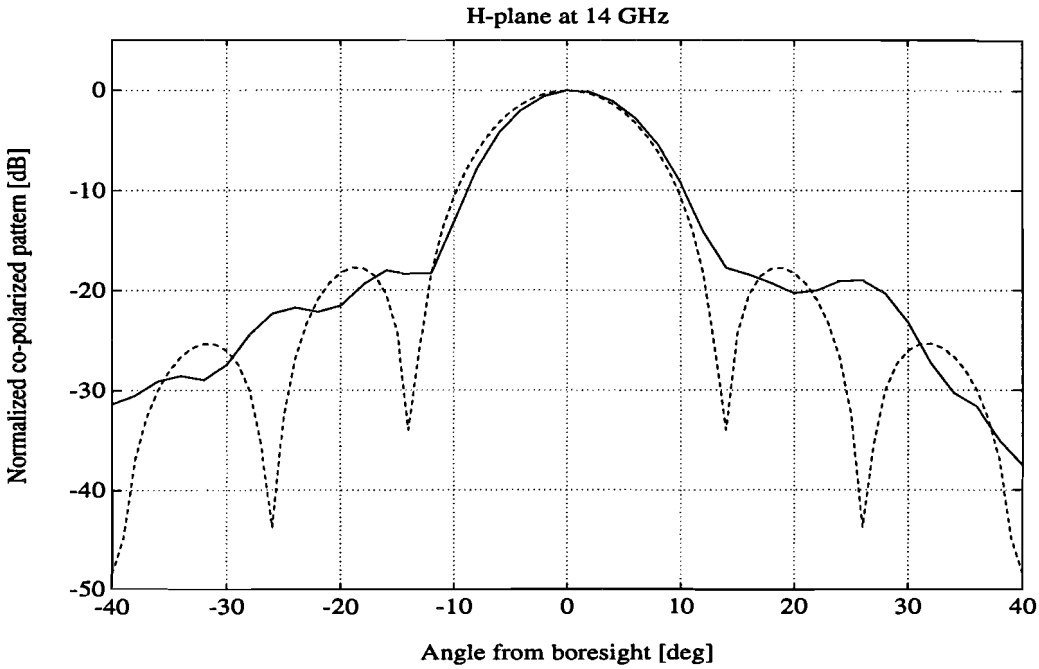

***Figure C.18** : Normalized co-polarized patterns of a double-dipole with a backing reflector on an elliptical HDP lens (solid line: Skalare, and dashed line: EUT).*

It appears that also for the frequencies used in this appendix there only exist a good agreement for the main beam. The discrepancies for larger angles from boresight again cannot be neglected and in Chapter four it is explained why these differences between theory and measurements can exist. In Chapter four it is also seen that the co-polarized patterns are not symmetrical around 0°, especially in the H-plane. From Figures C.1 to C.18 the same conclusion can be drawn.